ABSTRACT

Title of Dissertation: IMPROVING THE ESTIMATION OF LEAF AREA INDEX FROM MULTISPECTRAL REMOTELY SENSED DATA

Hongliang Fang, Doctor of Philosophy, 2003

Dissertation directed by: Dr. Shunlin Liang, Associate Professor
Department of Geography
University of Maryland

Leaf Area Index (LAI) is an important structural property of surface vegetation. Many algorithms use LAI in regional and global biogeochemical, ecological, and meteorological applications. This dissertation reports several new, improved methods to estimate LAI from remotely sensed data.

To improve LAI estimation, a new atmospheric correction algorithm was developed for the Enhanced Thematic Mapper Plus (ETM+) imagery. It can effectively estimate the spatial distribution of atmospheric aerosols and retrieve surface reflectance under general atmospheric and surface conditions. This method was validated using ground measurements at Beltsville, Maryland. Several examples are given to correct AVIRIS

(Airborne Visible/Infrared Imaging Spectrometer), MODIS (Moderate Resolution Imaging Spectroradiometer) and SeaWiFS (Sea-viewing Wide Field-of-view Sensor) data using the new algorithm.

Next, a genetic algorithm (GA) was incorporated into the optimization process of radiative transfer (RT) model inversion for LAI retrieval. Different ETM+ band combinations and the number of "genes" employed in the GA were examined to evaluate their effectiveness. The LAI estimates from ETM+ using this method were reasonably accurate when compared with field measured LAI.

A new hybrid method, which integrates both the RT model simulation and the non-parametric statistical methods, was developed to estimate LAI. Two non-parametric methods were applied, the neural network ((NN) algorithms and the projection pursuit regression (PPR) algorithms. A soil reflectance index (*SRI*) was proposed to account for variable soil background reflectances. Both atmospherically corrected surface reflectances and raw top-of-atmosphere (TOA) radiances from ETM+ were tested. It was found that the best way to estimate LAI was to use the red and near infrared band combination of surface reflectance. In an application of this hybrid method to MODIS, the PPR and NN methods were compared. MODIS LAI standard products (MOD15) were found to have larger values than my results in the study area.

IMPROVING THE ESTIMATION OF LEAF AREA INDEX FROM MULTISPECTRAL REMOTELY SENSED DATA

By

Hongliang Fang

Dissertation submitted to the Faculty of the Graduate School of the
University of Maryland, College Park in partial fulfillment
of the requirements for the degree of
Doctor of Philosophy
2003

Advisory Committee:

Dr. Shunlin Liang, Chairman
Dr. Jeffrey T. Morisette
Dr.: Stephen D. Prince
Dr. John R. G. Townshend
Dr. Richard Weismiller

DEDICATION

To people whose love and support made me feel that I was never alone.

ACKNOWLEDGEMENTS

I could never have achieved this goal without the support of many persons.

I wish to thank my advisor, Dr. Shunlin Liang, for his continued encouragement of my research, and for giving me a level of independence which was both very trying and exhilarating. I am very grateful for his scholarly guidance and strong support throughout the entire period of this research. The implementation of this study was made possible through grants from NASA of which Dr. Liang is the primary investigator.

I am grateful for the support and guidance provided by other members of my dissertation committee, including Drs. Jeffrey Morisette, Stephen Prince, John Townshend, and Richard Weismiller. I particularly would like to thank Dr. Townshend for his advice and valuable suggestions during my study in the Department of Geography, University of Maryland.

I wish to thank Dr. Charles Walthall, Dr. Craig Daughtry, Dr. Jay Radhakrishnan, Wayne Dulaney, Andy Russ, and Monisha Kaul, from Beltsville Agricultural Research Center (BARC), USDA. I enjoyed collaborating with you and thank you for your help during my research. My conversation with Dr. Walthall bolstered my confidence in pursuing a personal goal.

I wish to thank other members of this group, Dr. Mingzhen Chen, now at the University of Toronto, Chad Shuey and Lynn Thorp, for their support and help during my study. Thank you very much, I enjoyed working with you.

I would like to thank Dr. Crystal B. Schaaf, and Dr. Feng Gao, Boston University, who provided much needed support during my research. Special thanks are extended to Dr. Andres Kuusk, Tartu Observatory, Estonia, for his scholarly support and kindly providing his latest model codes.

I would especially like to thank Drs. David Jupp, Tim McVicar and Tom G. Van Niel, CSIRO, Australia, who provided data and valuable suggestions for my research through these years. I am looking forward to meeting Tim and Tom one day.

In 2002, I received an assistantship from the Joint Global Change Research Institute (JGCRI) of the Pacific Northwest National Laboratory (DOE) and the University of Maryland. Drs. Roberto Cesar Izaurralde, Norman J. Rosenberg, and Steve Fetter of JGCRI provided valuable guidance and support during my research at JGCRI. There are numerous people who provided valuable assistance during my field work in Tucson, Arizona in September 2002. I would like to thank Drs. Stuart E. Marsh, Sam Drake, Wim van Leeuwen, from the University of Arizona, who provided field assistance, logistical support and accommodation during the field campaign. Thanks must be extended to Ms. Allison M. Thomson from the Pacific Northwest National Laboratory of the Department of Energy. She helped greatly during the field study.

I wish to thank members of the Geography Department at the University of Maryland, College Park, who provided me with an intellectual home over the past years. Thanks must go particularly to Dr. Michael Kearney for his helpful advice in my geographical study.

TABLE OF CONTENTS

List of Tables ix

List of Figures x

Chapter 1 Introduction 1

1.1 Importance of leaf area index (LAI) 1
1.2 Current optical remote sensing methods for LAI estimation 4
1.2.1 Empirical relationships based on vegetation indices 6
1.2.2 Canopy reflectance model inversion 9
1.2.3 Nonparametric methods 15
1.3 Objectives of this study 16
1.3.1 Development of new atmospheric correction algorithm 17
1.3.2 Development of new LAI inversion methods 18
1.3.3 Validation of LAI products 20
1.4 Structure of the dissertation 22

Chapter 2 Development of New Atmospheric Correction Algorithm 23

2.1 Introduction 23
2.2 Existing atmospheric correction algorithms 24
2.2.1 Ground-based methods 24
2.2.2 Image-based methods 25
2.2.3 Atmospheric model-based methods 26
2.3 New methodology 28
2.3.1 Processing heterogeneous haze 28
2.3.2 Correcting surface adjacency effects 32
2.4 Results and validation 36
2.4.1 ETM+ results 36
2.4.2 Validation 38
2.5 Extensions to other areas and sensors 44
2.5.1 AVIRIS 46
2.5.2 MODIS 46
2.5.3 SeaWiFS 49
2.6 Summary 51

Chapter 3 LAI Retrieval Using a Genetic Algorithm 52

3.1 Introduction 52
3.2 The genetic algorithm and the radiative transfer model 54

3.3 Experimental study 58
3.3.1 Surface reflectance and LAI measurements 58
3.3.2 Experiments with different reflectance data sets 64
3.3.3 Strategies to fix free parameters and select ETM+ bands 66
3.4 Results and analysis 69
3.4.1 Using the retrieved ETM+ reflectance 69
3.4.2 Using field measured reflectance data 78
3.4.3 Comparison with other methods 81
3.5 Summary 86

Chapter 4 LAI Retrieval from ETM+ with a Hybrid Approach 88

4.1 Introduction 88
4.2 Background 90
4.2.1 Creating the LUT with a RT model 90
4.2.2 Neural network method 93
4.3 Methodology 94
4.3.1 The soil reflectance index (SRI) 95
4.3.2 Companion methods to calculate soil reflectance 99
4.3.3 Creating the databases 102
4.3.4 Estimating LAI with the NN method 104
4.4 Results and analysis 105
4.4.1 LAI retrieval from ETM+ surface reflectance 105
4.4.2 LAI retrieval from ETM+ raw radiance 106
4.4.3 Validation 110
4.4.4 Comparison with the genetic algorithm results 113
4.4.5 LAI mapping 115
4.5 Summary 116

Chapter 5 Mapping LAI from MODIS Using a Hybrid Inversion Method 120

5.1 Introduction 120
5.1.1 The MODIS LAI algorithm 121
5.2 Methodology 124
5.2.1 Data preparation 124
5.2.2 Atmospheric correction, aggregation and registration of ETM+ imagery 125
5.2.3 Determining the soil reflectance index 126
5.2.4 Creating the database with the radiative transfer model 131
5.2.5 Nonparametric training and prediction 131
5.3 Results 133
5.3.1 LAI maps from MODAGG 138

5.3.2 LAI maps from aggregated ETM+ 138
5.3.3 Comparison of LAI distributions 140
5.4 Discussion and summary 142

Chapter 6 Conclusion 146

6.1 A new atmospheric correction algorithm for ETM+ 146
6.2 Application of genetic algorithm in the optimization of RT model inversion 147
6.3 LAI retrieval with a hybrid method from ETM+ 149
6.4 LAI retrieval from MODIS data with a hybrid approach 150
6.5 Algorithm comparison 152
6.6 Issues for further research 153

REFERENCES 155

List of Tables

Table 1.1 Observational requirements for leaf area index. 3

Table 1.2 Some representative instruments/teams that are using remote sensing to estimate LAI.* 5

Table 3.1 Input parameters to the canopy radiative transfer model, MCRM. 57

Table 3.2 Field LAI measurements at BARC. (a) shows the mean, standard deviation (std) and coefficient of variation (CV), number of points, and cover type[a] of each plot. (b) shows the mean CV and the total number of plots (in brackets) of each cover type for the four dates. 62

Table 3.3 An example of a genetic algorithm output (six genes). 75

Table 3.4 The mean standard deviation of the LAI-GA and field LAI for different number of genes (6, 5, 4 and 3) and band combinations. 76

Table 4.1 Parameter values used to establish the canopy reflectance database. 91

Table 4.2 Soil line parameters extracted from various dates. L_1 and L_2 are the lower and upper percentiles of the reflectance of pixels in band 3 to calculate the minimum and maximum soil reflectances used for SRI. 98

Table 4.3 Comparison of R^2 and RMSE for different neural network scenarios and the application of the soil reflectance index (SRI). Band combinations use surface reflectances simulated from MCRM. 107

Table 4.4 Same to Table 4.3 , but using TOA radiance in band combinations. 108

Table 4.5 Relative R^2 and the RMSE differences for different bias levels. Band (3,4) is used for surface reflectance and (4, NDVI) for TOA radiance. 114

Table 4.6 Statistics of the LAI-NN estimated from the four ETM+ reflectances. 119

Table 5.1 Statistics of the MODIS LAI products, LAI estimated from the aggregated ETM+ data and from the MODAGG data. The minimum (Min), mean and maximum (Max) values of the neural network (NN) and the projection pursuit regression (PPR) methods are shown for the two dates. The two mean values correspond to pixels with the main RT method and backup method, respectively. 135

Table 6.1 Comparison of the GA optimization methods, the hybrid approach the MODIS LAI algorithm. 152

List of Figures

Figure 1-1 Flowchart of the LAI estimation processes. 19

Figure 2-1 Flowchart of the new atmospheric correction algorithm. VIS: visible bands; AOT: aerosol optical thickness. 29

Figure 2-2 Relative contribution of the neighboring pixels from equation (2.7). The aerosol optical depth (τ) is from May 11, 2000. The six lines are for band one to six downward. 35

Figure 2-3 False color composite (RGB432) and difference images of Landsat ETM+ reflectances at the BARC study area (July 29, 1999). White/blue polygons in (a) are hazy/shadow regions, respectively. Lines AA' and BB' are used in Figure 2-4. 37

Figure 2-4 False color composite of ETM+ (RGB432) before (a) and after (b) atmospheric correction The image was acquired on May 11, 2000 and has a size of 512×512. (c) the NIR reflectance profiles of line AA'. (d) the blue band reflectance profiles of line BB'. 39

Figure 2-5 Comparison of retrieved surface reflectance from ETM+ (crosses) and measured (lines) reflectance at different sites on May 11, 2000. The solid line is the mean ASD reflectance and the dotted line is ± one standard deviation away from the mean. 40

Figure 2-6 Comparison of the retrieved ETM+ reflectance and the aggregated ASD measured reflectance acquired on four dates: May 11, 2000 (□), Oct 2, 2000 (○), Apr 28, 2001 (◇) and Aug 2, 2001(△). 42

Figure 2-7 Comparison of the surface reflectance of 'invariant' objects from three ETM+ bands of May 11, 2000 and July 28, 1999. 43

Figure 2-8 Examples of three ETM+ scenes (Nov 17, 1999) before (left column) and after (right column) atmospheric correction. The images are of true color composites (RGB321). 45

Figure 2-9 AVIRIS images (May 11, 2000) of the BARC study area. (a) and (b) are band 14 (500nm) before and after atmospheric correction using the cluster match method respectively. (c) and (d) are band 26 (618 nm) before and after processing. The image is 512 (lines) × 614 (columns). 47

Figure 2-10 MODIS band 3 (blue) before (a) and after (b) atmospheric correction, and false color composite image (RGB214) before (c) and after (d) correction. The image size is 400×400. 48

Figure 2-11 SeaWiFS band 2 (blue) before (a) and after (b) atmospheric correction, and false color composite image (RGB753) before (c) and after (d) correction. The image size is 512×512. 50

Figure 3-1 Flowchart of the approach to estimate LAI with a genetic algorithm optimization method. 59

Figure 3-2 Two examples of simultaneous ASD-measured surface spectral reflectances (lines) and the atmospherically corrected reflectances from ETM+ (crosses). Vertical line segments denote the standard deviation of the ETM+ reflectances. Dashed lines are one standard deviation away from the mean reflectances (solid line). 63

Figure 3-3 The distribution of S_z, C_{ab}, N and ε^2(E^2) (rows) as derived with the GA optimization method. The four columns are using: all six ETM+ bands, RED+NIR, NIR only, and red only, respectively. 68

Figure 3-4 Comparison of LAI-GA with field LAI. LAI-GA is estimated from Landsat ETM+ images using: a) all six bands; b) red and near infrared band only; c) NIR band only; and d) red band only. Symbols for a)~d): May 11 (□) and Oct 2 (○) 2000 and Apr 28 (◇) and Aug 2 (△) 2001. The one standard deviation of field LAI and LAI-GA are shown with line segments. R^2: R square. 6 genes (LAI, S_z, C_{ab}, N, r_{s1} and r_{s2}) were used. (e)~h) compare LAI of different cover types, alfalfa (▽), barley, hairy vetch and orchard grass (×), corn (□), deciduous forest (○), grass (◇), soybean (+), and wheat (△). 71

Figure 3-5 Comparison of field LAI with LAI-GA derived from Landsat ETM+ with five genes (LAI, C_{ab}, N, r_{s1} and r_{s2}) fixing S_z=0.8. (a)~(d) compare LAI of different dates. One standard deviation of LAI-GA is shown. (e)~(h) compare LAI of different cover types. Symbols: refer to Figure 3-4. 72

Figure 3-6 Comparison of field LAI with LAI-GA derived from Landsat ETM+ with four genes (LAI, N, r_{s1} and r_{s2}) fixing S_z=0.8 and C_{ab}=50. (a)~(d) compare LAI of different dates. One standard deviation of LAI-GA is shown. (e)~(h) compare LAI of different cover types. Refer to Figure 3-4 for symbols. 73

Figure 3-7 Comparison of field LAI with LAI-GA derived from Landsat ETM+ with three genes (LAI, r_{s1} and r_{s2}) fixing S_z =0.8, C_{ab} =50 and N=1.8. (a)~(d) compare LAI of different dates. One standard deviation of LAI-GA is shown. (e)~(h) compare LAI of different cover types. Refer to Figure 3-4 for symbols. 74

Figure 3-8 Retrieved LAI-GA values for different ground types (A: alfalfa; B: barley; C: corn; F: deciduous forest; G: grass; H: hairy vetch; O: orchard

grass; S: soybean; W: wheat). The numbers above the bars are one standard deviation. 79

Figure 3-9 Comparison of LAI-GA (solid points) with field measured LAI. LAI-GA was derived from field ASD-measured reflectance data collected at BARC, USDA. The LAI derived from ETM+ 6 bands (hollow points) are also shown. (a)~(d) compare LAI of different dates. (e)~(h) compare LAI of different cover types. Refer to Figure 3-4 for symbols. 80

Figure 3-10 Comparison of LAI maps generated for (a) Apr 28 and (b) Aug 2, 2001 using GA method; (c) Apr 28 and (d) Aug 2, 2001 using the Powell inversion algorithm. 83

Figure 3-11 Comparison of LAI retrieved with GA optimization method (LAI-GA) and with the Powell inversion algorithm (LAI-Powell) for (a) Apr 28 and (b) Aug 2, 2001. 84

Figure 3-12 LAI-NDVI relationships. Polynomial and power functions are used to correlate NDVI and LAI. 85

Figure 4-1 Reflectance of soil pixels in red and NIR bands. S_1 (or S_2) are a set of pixels within radius L_1 (or L_2) from the two dark points which are global minimum (ρ_{Gmin}) and maximum (ρ_{Gmax}) reflectance, respectively. 97

Figure 4-2 Spectral reflectance of Codorus soil at a range of relative water contents (RWC) from oven dry (RWC = 0.0) to water saturated (RWC = 1.0). *RI* (reflectance index) represents the magnitude between the minimum and maximum reflectances. 101

Figure 4-3 Comparison of LAI-NN with field LAI. LAI-NN is estimated from Landsat ETM+ images with the neural network methods for four different soil reflectance options: a) SN1; b) SN2; c) SN3; and d) SRI. Symbols: May 11 (□) and Oct 2 (○) 2000 and Apr 28 (◇) and Aug 2 (△) 2001. (e)~h) compare LAI of different cover types, alfalfa (▽), barley, hairy vetch and orchard grass (×), corn (□), deciduous forest (○), grass (◇), soybean (+), and wheat (△). R^2: R square. The solid line is the 1:1 line, and the dashed one the regression line. 111

Figure 4-4 Comparison of retrieved forest LAI-NN values retrieved with SN1 (□), SN2 (◇), SN3 (Δ) and the SRI (•), respectively, with measure LAI. The intercepts of the dashed lines are ±1. 112

Figure 4-5 Comparison of LAI derived from the neural network method (LAI-NNT) and the genetic algorithm (LAI-GA) of two 30×30 pixels regions in Figure 3-10. (a) Apr 28, 2001; (b) Aug 2, 2001. 114

Figure 4-6 LAI maps generated with the neural network method from ETM+ reflectances. (a) May 11, 2000; (b) Oct 2, 2000; (c) Apr 28, 2001; (d) Aug 2, 2001. Band (3, 4) and SRI are used in the NN training. 117

Figure 4-7 LAI distribution estimated using the proposed hybrid approach with ETM+ for Apr 28, 2001 over the Washington, DC area. White box shows the Figure 4-6c area. Size: 1500 by 1500 pixels. 118

Figure 5-1 Work flow of the hybrid approach to estimating leaf area index with remote sensing imagery. 122

Figure 5-2 The scatterplot of the red (x) and near-infrared (y) reflectances for ETM+ and MODAGG imageries. The ETM+ scatterplots are of different resolutions (240m, 510m, 750m and 990m). The strip within the dashed lines shows the soil pixels. 128

Figure 5-3 Presentation of the registration of the MODIS LAI product (red), the aggregated ETM+ LAI (green) and the MODAGG LAI (blue) of the study area. The ETM+ (the smaller lozenge region) and MODAGG data are of Aug 28, 2001. The MODIS LAI product is of May 1, 2001. 136

Figure 5-4 MODIS biome types for LAI products. Color numbers: 0, Water or unclassified; 1, Grasses/Cereal crops; 2, Shrubs; 3, Broadleaf crops; 4, Savannah; 5, Broadleaf forest; 6, Needleleaf forest. 136

Figure 5-5 MODIS LAI products for (a) May 1, 2001 and (c) Aug 5, 2001. (b) and (d) depict the MODIS LAI algorithms for the two dates. Red (yellow) color represents that the main radiative transfer method (the empirical backup method) is used. 137

Figure 5-6 LAI estimated from MODAGG data (1 km). The top two are for Apr 28, 2001 and the bottom two Aug 2, 2001. (a) and (c) are from the neural network algorithm; (b) and (d) are with the projection pursuit regression method. LAI legend same as Figure 5-5. 139

Figure 5-7 LAI estimated from aggregated ETM+ reflectance (510 m). The top two are for Aug 28, 2001 and the bottom two Aug 2, 2001. (a) and (c) are from the neural network algorithm; (b) and (d) are with the projection pursuit regression method. LAI legend same as Figure 5-5. 141

Figure 5-8 Histogram comparison of the MODIS LAI products and LAI derived from MODAGG and aggregated ETM+ data. The two columns represent the results of two dates (Apr 28 and Aug 2, 2001 respectively). (A-B) MODIS LAI products; (C-D) From ETM+ with NN method; (E-F) From ETM+ with PPR method; (G-H) From MODAGG with NN method; and (I-J) from MODAGG with PPR method. 143

Chapter 1 Introduction

Leaf area index (LAI), defined as the total one-sided green leaf area per unit ground surface area, describes an important structural characteristic of vegetation. Remote sensing provides a very effective means of rapidly-obtaining LAI over a large area. Currently, LAI is estimated from remotely sensed data through its statistical relationship with spectral vegetation indices, by physical model inversion and other methods. With the availability of some new sensors, it is necessary to test existing methods and find out if the development of new methods is needed. Although some remote sensing teams are providing LAI products, LAI accuracy is still unclear as large-scale validation work has not been done. Some primary validation results have shown the accuracy of existing LAI products cannot meet the requirements of various applications. For example, the current LAI products need improvement in terrestrial carbon cycle modeling (Cihlar et al., 2000). My primary objective was to develop new algorithms to improve the estimation of LAI from remotely sensed data. The results obtained with these algorithms were validated with ground measurements.

1.1 Importance of leaf area index (LAI)

The plant canopy acts as a critical interface between the atmosphere and terrestrial biosphere. Considering the abundance of global vegetation, there is an enormous variety of canopy shapes, sizes, and attributes. Characterization of vegetation in terms of LAI, rather than species composition, is a critical simplification of different terrestrial

ecosystems worldwide (King, 1999). Because these leaf surfaces are the primary sites of energy and mass exchange, important processes—such as canopy interception, evapotranspiration, and gross photosynthesis—are directly proportional to LAI (Chen, 1996a).

McNaughton and Jarvis (1983) demonstrated that LAI is important in determining canopy-scale estimates of evapotranspiration. Gholz (1982) and Grier and Running (1977) related LAI to the site water balance of mature coniferous forest communities in western Oregon. Functional relationships exist between LAI and net primary production (Gholz, 1982) and stemwood production (Schroeder et al., 1982) of temperate coniferous forests. McLeod and Running (1988) correlated LAI to volume growth of ponderosa pine (*Pinus ponderosa*) stands in western Montana. In perennial biomes such as forests, LAI reflects climatic optima; warm, wet climates produce forests of high LAI, while colder, drier climates produce lower LAI (McLeod and Running, 1988), so it could be used to measure the magnitude of the biogeochemical cycling of a vegetation type. LAI changes seasonally in crops and annual vegetation types, and the seasonal increase in LAI provides a good crop development monitor. Several reports (Botkin, 1986; Wittwer, 1983) identify LAI as the single most important variable for characterizing vegetation energy and mass exchange for global-scale research.

LAI is a required input to many models that quantify terrestrial photosynthesis (Running and Coughlan, 1988), hydrological balance (Bonan, 1993), global carbon cycle (Prince and Goward, 1995), and circulation processes (Sellers et al., 1986). Table 1.1 show

several regional and global programs which require LAI for agricultural, hydrological or climatic research. In this table, horizontal resolution (Hor Res), observing cycle (Obs Cycle), accuracy and delay of availability are all expressed as optimum/threshold values.

FPAR (fraction of absorbed photosynthetically active radiation) is another important biophysical variable. FPAR is frequently used to translate satellite data such as

Table 1.1 Observational requirements for leaf area index.

Requirement	Hor Res (km)	Obs Cycle (day)	Accuracy (%)	Delay (day)	Confidence	Applications
WMO	0.01-10	5-7	5-10	1-5	Reasonable	Agricultural Meteorology
WMO	10-50	7-30	5-20	1-7	Tentative	Regional NWP
WMO	0.01-10	7-24	5-20	1-5	Reasonable	Hydrology
WMO	50-100	7-30	5-20	1-7	Tentative	Global NWP
GCOS	0.1-1	10-30	20-100	10-30	Tentative	Terrestrial Climate
GTOS	0.1-1	10-30	20-100	10-30	Tentative	Terrestrial Climate

GCOS: Global Climate Observing System
GTOS: Global Terrestrial Observing System
NWP: Numerical Weather Prediction
WMO: World Meteorological Organization
(*http://alto-stratus.wmo.ch/sat/stations/_asp_htx_idc/Requirementsearch.asp*)

NDVI (Normalized Difference Vegetation Index) into estimates of primary production. Asrar et al. (1992) found that FPAR is curvilinearly related to LAI, approaching the asymptote at an LAI of 6. LAI and FPAR are two basic quantities used in regional climate simulations. This dissertation focuses on LAI and its estimation from remotely sensed data.

In the laboratory, LAI is often calculated from the measured specific leaf area (SLA) (Gower et al., 1992). In the field, LAI could be obtained directly or indirectly: Direct methods measure LAI through litterfall or destructive sampling; indirect methods estimate LAI via measurements of canopy transmittance. Using the Beer-Lambert Law, which assumes that leaf inclination angles are spherically and randomly distributed and that the foliage is distributed randomly in space (Jarvis and Leverenz, 1983), canopy transmittance can be converted to LAI. The LAI-2000 is an instrument commonly used to indirectly estimate LAI (Deblonde et al., 1994; Lang, 1987). Hemispherical photographs and TRAC (Tracing Radiation and Architecture of Canopies) are two other methods that are often used, especially for forest canopies (Chen and Balck, 1991; Chen and Cihlar, 1995). Direct measurements are more accurate at a point scale and are often used in LAI validation. However, they are very labor-intensive and thus impractical for large regions. Indirect measurements of LAI, useful for quantifying small patches of vegetated areas (Kucharik et al., 1998), are subject to substantial errors due to their influence by shoot structures, dead branches and stems. For example, the LAI-2000 could overestimate green LAI of canopies that contain numerous dead branches. In general, all laboratory and field LAI estimations are limited for global research needs and are primarily used for calibrating and validating other methods.

1.2 Current optical remote sensing methods for LAI estimation

Satellite remote sensing provides a unique way to obtain LAI over large areas (Prince, 1999). Various data from new satellites that are or are going to be available will bring a

new era of LAI mapping (Table 1.2). There is a wealth of research into methods for the estimation of LAI using different optical remote sensing instruments. Algorithms for retrieving LAI from Landsat Multispelctral Scanner (MSS) (Yin and Williams, 1997), NOAA Advanced Very High Resolution Radiometers (AVHRR) (Privette et al., 1996), and Landsat TM (Fassnacht et al., 1997; Kuusk, 1998) have been developed. MODIS and MISR (Multiangle Imaging SpectroRadiometer) science teams also provide LAI products based on their methods (Diner et al., 1999; Knyazikhin et al., 1999). LAI data can also be obtained from ADEOS-POLDER and SPOT 4-VEGETATION.

Table 1.2 Some representative instruments/teams that are using remote sensing to estimate LAI.*

Instruments	**Res. (km)**	**ObsCy.**	**Agency**	**HTTPs**
MODIS	1	8d	NASA	*modis.gsfc.nasa.gov*
MISR	1.1	2d	NASA	*www-misr.jpl.nasa.gov*
MERIS	0.3	3d	ESA	*Envisat.esa.int/instruments/meris*
GLI	1	16d	Japan	*sharaku.eorc.nasda.go.jp/ADEOS2/index.html*
POLDER	6	41d	CNES	
VEGETATION	1	1d	Multi-country	*www.spot-vegetation.com*
Panchromatic imager camera (PIC)	0.01	7d	NEMO, US Navy	*www.tec.army.mil/tio/nemo.htm*
Imaging spectrometer	0.03	7d	CSIRO, Australia	*www.atnf.csiro.au/pasa/15_2/ryder/paper/*

* *http://alto-stratus.wmo.ch/sat/stations/satsystem.html*

However, LAI accuracy from sensors in Table 1.2 still cannot meet the requirements in Table 1.1. Even for MODIS, MISR and POLDER, the accuracies of the LAI products have not been well documented. For example, the current MODIS LAI product could

vary as much as ±25% from field-measurements*. My studies (introduced later in this dissertation) have found even greater errors. Investigations are also needed to address issues such as improving the LAI estimation accuracy at high LAI values for better understanding of the terrestrial carbon cycle (Cihlar et al., 2000). The following sections discuss general methods estimating LAI from remotely sensed data.

1.2.1 Empirical relationships based on vegetation indices

Early leaf reflectance measurements of visible and infrared energy identified a strong correlation between a red and near-infrared transmittance ratio and measured LAI (Jordan, 1969). Recognition that reflectance measurements offer the opportunity to "scale up" from the plot level to larger areas has sustained interest over the last three decades in developing empirical algorithms relating LAI to surface reflectance and to spectral vegetation indices (VI) derived from reflectance (Turner et al., 1999). Reflectances in red and near-infrared wavebands have been used to formulate various vegetation indices as indicators of the conditions of vegetated surfaces (Asrar et al., 1984; Jordan, 1969; Kaufman and Tanré, 1992; Liu and Huete, 1995; Roujean and Bréon, 1995). Vegetation indices were designed to maximize sensitivity to the vegetation's characteristics while minimizing confounding factors such as soil background reflectance, directional, and atmospheric effects.

The most commonly used vegetation indices utilize the information contained in red and near-infrared (NIR) canopy reflectances or radiances. They are combined in the form of

* *http://alto-stratus.wmo.ch/sat/stations/_asp_htx_idc/ParamInst.asp*

ratios: ratio vegetation index (RVI) (Pearson and Miller, 1972) or normalized difference vegetation index (NDVI) (Rouse et al., 1974).

$$RVI=RED/NIR \tag{1.1}$$

$$NDVI = (NIR-RED)/(NIR+RED), \tag{1.2}$$

where RED and NIR represent spectral reflectances in the red and near-infrared regions. Although these indices enhance the contrast between soil and vegetation and minimize the effects of illumination conditions, they are sensitive to optical properties of soil background. For a given amount of vegetation, darker soil substrates result in higher vegetation index values (Elvidge and Lyon, 1985; Huete et al., 1985).

The perpendicular vegetation index (PVI) refers to the perpendicular distance from a point corresponding to canopy reflectance in red-NIR space and the line joining points for soil reflectance (Richardson and Wiegand, 1977). Experimental and theoretical investigations show that PVI is also affected by optical properties of soil background; brighter soils result in higher index values for a given quantity of incomplete vegetation cover (Huete, 1988 ; Huete et al., 1985). For this reason some new indices, which are less influenced by soil brightness, have been proposed, for example, the weighted difference vegetation index (WDVI) (Clevers, 1989), soil adjusted vegetation index (SAVI) (Huete, 1988), and the transformed soil adjusted vegetation index (TSAVI) (Baret et al., 1989) .

A common procedure to estimate LAI is to establish an empirical relationship between VI and LAI by statistically fitting observed LAI values to the corresponding VI. Among proposed LAI-VI relations are the following forms (Asrar et al., 1985a; Asrar et al., 1985b; Baret, 1995; Best and Harlan, 1985; Curran, 1983; Peterson et al., 1987; Price and Bausch, 1995):

$$\mathrm{LAI}=Ax^3+Bx^2+Cx+D \tag{1.3}$$

$$\mathrm{LAI}=A+Bx^C \tag{1.4}$$

$$\mathrm{LAI}=-1/2A\ln(1-x) \tag{1.5}$$

$$\mathrm{LAI}=f(x), \tag{1.6}$$

where x is either a vegetation index or the reflectances derived from remotely sensed data. Coefficients A, B, C, and D are empirical parameters and vary with vegetation types. The last equation is a generic function of any form. Given a set of coefficients, the equations can be applied to remotely sensed images to map the spatial LAI distributions. These relationships were confirmed using reflectance model simulation (Sellers, 1985). Chen (1996a) showed that the RVI is the best for estimating LAI in boreal forests. White (1997) showed that the NDVI provided the best estimate of LAI in his study site (conifer forests).

The advantage of the VI approach is its simplicity and ease of computation. However, the VI approach only uses very limited amounts of spectral information, generally red and infrared bands, though there is rich spectral information provided by current remote

sensing instruments. The proposed LAI-VI equations have diversified forms. These equations vary not only in mathematical form (linear, power, exponential, etc.), but also in their empirical coefficients, depending primarily on vegetation types. To use this VI approach operationally, an LAI-VI equation must be established for each vegetation type, which requires substantial LAI ground measurements and corresponding remote sensing data. Because there is no universal LAI-VI equation applicable to diverse vegetation types, it is difficult to use this approach for large-scale remote sensing images. Moreover, the vegetation indices approach a saturation level asymptotically for LAI ranging from 2 to 6, depending on conditions (Ahlrichs and Bauer, 1983; Best and Harlan, 1985; Chance, 1981; Daughtry et al., 1980).

Another limitation of this approach is the sensitivity of VI to non-vegetation related factors such as soil background properties (Huete, 1989), atmospheric conditions (Kaufman, 1989; Vermote et al., 1990), topography (Holben and Justice, 1980; Justice et al., 1981), and bi-directional surfaces (Burgess and Pairman, 1997; Deering, 1989; Roujean et al., 1992). The effects from soil background variations and atmospheric conditions may be decreased to some extent by developing improved vegetation indices (Clevers, 1989; Huete, 1988; Kaufman and Tanré, 1992; Qi et al., 1994).

1.2.2 Canopy reflectance model inversion

Canopy reflectance models relate fundamental surface parameters (e.g., LAI, leaf optical properties) to scene reflectance for a given sun-surface-sensor geometry. During the last

three decades, roughly, a large of number of surface bidirectional reflectance distribution function (BRDF) models have been developed (Goel and Thompson, 2000; Myneni et al., 1989). Some models (sometimes called parametric models) are based on simple mathematical functions of reflectance distribution (Rahman et al., 1993; Roujean et al., 1992; Walthall et al., 1985). Others are physical radiative transfer models and have been used to estimate plant morphological and optical properties (Goel, 1988; Qin and Liang, 2000).

1.2.2.1 Canopy radiative transfer models

Canopy radiative transfer models may be grouped into four model classes: geometric, turbid medium, hybrid, and computer simulation.

Geometric models simulate heterogeneous scenes with geometric objects (e.g., cones, spheroids, ellipsoids, cubes) protruding from a surface (e.g. Jasinski, 1990; Li and Strahler, 1985; Otterman, 1984). Optical behavior of the objects is constant or simplified. Reflectance anisotropy is determined primarily by the fractions and spatial orientation of shaded and sunlit surfaces (both canopy and ground) for a particular sun-target-sensor geometry. Representative geometric models are used by Li et al. (1996; 1986) and by Jupp et al. (1986), who use a spheroid-on-a-stick shape. Geometric models have been inverted to retrieve canopy structural (Li and Strahler, 1985; Woodcock et al., 1997) and optical information (Chen et al., 2000; Otterman et al., 1987).

Turbid-medium models simulate a canopy with a cloud of infinitesimal platelets having the optical properties of plant organs (most commonly leaves). The models generally include single and multiple scattering; the former is determined quasi-analytically, while the latter must be approximated. The canopy architecture is described at the leaf level through LAI and LAD (leaf angle distribution). A widely used model in this category is the SAIL model (Verhoef, 1984) which was later modified to include hotspots and specular reflection (Goel and Kuusk, 1992). These models, best suited for dense canopies with small vegetation elements, have successfully simulated RT in mature agricultural crops. Drawbacks of the turbid-medium approach include the absence of scattering behavior caused by the finite size of actual scattering elements, which cause phenomena such as shading and the non-random orientation of scattering elements, (e.g., leaf clumping) which cannot be simulated by a uniform, turbid medium and thus makes them inappropriate for many canopies. Recent advances (Kuusk, 1994; Myneni and Ganapol, 1991; Ross and Marshak, 1989; Verstaete et al., 1990) have compensated for these shortcomings. Many turbid-medium models have been inverted to estimate LAI and other parameters (Goel, 1988; Kuusk, 1991; Kuusk, 1994; Liang and Strahler, 1994a; Liang and Strahler, 1994b; Nilson and Kuusk, 1989; Privette et al., 1994; Verstaete et al., 1990).

Hybrid models combine the spatial heterogeneity of geometric models and the realistic radiative transport treatment of turbid-medium models. This permits the simulation of gap probabilities and path-length distributions, along with single and multiple scattering (Li et al., 1995; Norman and Welles, 1983). However, multiple scattering is not

rigorously treated by these models (Goel and Thompson, 2000). In addition, the model complexity may result in a relatively high computational time. Thus, little operational application of these models has been reported in the literature.

Computer simulation models use the positions and orientations of various vegetation elements to describe the canopy. One model type uses Monte Carlo methods which rigorously trace photo interactions with an arrangement of discrete scatterers within the canopy (Govaerts and Verstraete, 1998; Ross and Marshak, 1988). Although computationally expensive, these models accurately simulate within-canopy spatial heterogeneity (e.g., organ size distribution, leaf clumping, gaps) and scene-scale heterogeneity (e.g., topography) that other models must either neglect or approximate with quasi-empirical formulations. While several models have been developed (Boreal et al., 1991; Goel et al., 1991; Ross and Marshak, 1988), their computational expense reduces the likelihood that they will be adopted for inversion applications (Antyufeev and Marshak, 1990).

1.2.2.2 Model inversion

To calculate canopy biophysical parameters, the canopy RT model has to be solved. Model inversion has been mainly applied over the directional distribution of reflectance (Pinty et al., 1990). The general reflectance model inversion problem may be stated as follows: given a set of empirical reflectance measurements, determine the set of canopy biophysical variables such that the computed reflectances best fit the empirical

reflectances (Myneni et al., 1995). The fit of the empirical data is determined by a merit function, ε^2, defined as

$$\varepsilon^2 = \sum_{i=1}^{n} \sum_{j=1}^{B} W_i (r_{ij} - \hat{r}_{ij})^2 \tag{1.7}$$

where r_{ij} is the observed directional reflectance for a given viewing and solar angle geometry, $\hat{r}_{ij}$ the simulation model estimate, n the number of reflectance samples, B the number of spectral bands, and W_i represents the weight. A penalty function may be used to limit the independent parameter space to physically possible values. The ability to correctly determine target parameter space through model inversion, therefore, depends on the dataset $\hat{r}_{ij}$, the model's likeness to physical reality and the chosen-optimization algorithm's ability to minimize ε^2 over the parameter space.

There are several methods for minimizing the merit function and the choice of a particular method depends on the mathematical properties of the function to be minimized. Some of these methods have been used for retrieving LAI, for example, the downhill simplex method used by Privette (1994), the conjugate direction set method used by Kuusk (1991), and Pinty's (1990) quasi-Newton method. These methods do not require evaluation of function derivatives for minimization. They are particularly appealing for complex, nonlinear formulations, as in canopy reflectance modeling.

The look-up table (LUT) method provides a simple solution to the traditional inversion problem. It makes use of the precomputed model reflectances from a large range of input parameters (Kimes et al., 2000) and thus can speed up the inversion process significantly. The LUT method is used by the MODIS science team to estimate LAI from a three-dimensional radiative transfer model (Knyazikhin et al., 1998a). This method is easy to use since most of the complications lie in generating the database. The accuracy of the LUT method is dependent upon the accuracy of biophysically-based RT models.

Canopy reflectance models have been applied to both spectral and directional dimensions (Bicheron and Leroy, 1999; Goel, 1988; Kuusk, 1995a; Privette et al., 1994; Roujean et al., 1997; Walthall, 1997). Model inversion has been mainly applied to the estimation of directional distribution of reflectance. For example, Liang and Strahler (1993b) presented a parametric model based on a rigorous canopy radiative transfer equation which is realistically sensitive to angular variation in sky radiance. Inversion of this model retrieved LAI very well (absolute difference<0.2 m^2/m^2).

There are some major limitations in operational use of a canopy modeling approach. The main deficiencies of most radiative transfer models are their complexity and difficulty in parameter inversion, which is a major barrier when using large satellite images. This is the reason why only simple radiative transfer models such as turbid-medium or geometric optics have been used (Weiss and Baret, 1999). Some models may have multiple solutions, given a set of remote-sensing measurements, and the inversion may

not always converge (Jacquemoud, 1993). Some of these models are suitable for crops and grass land (Gao and Lesht, 1997; Kuusk, 1995a), while some are more applicable for forest because they take into account the canopy's geometric structure (Li and Strahler, 1992; Rosema et al., 1992).

1.2.3 Nonparametric methods

Neural network algorithms are commonly used, nonparametric methods in remote sensing parameter retrieval. They provide a very efficient tool to establish the relationship between the simulated reflectance field and the corresponding biophysical variables of interest (Baret et al., 1995; Baret and Fourty, 1997; Jin and Liu, 1997; Smith, 1993). Smith first trained a back-propagation neural network to invert a simple multiple scattering model to estimate leaf area index from reflectance at three wavelengths and then subsequently applied the trained network to satellite observations. He reported error estimates under 30% and indicated that the method appeared to be much less sensitive to initial guesses for the parameters than other inversion techniques. Gong et al. (1999) employed an error back-propagation feed-forward neural network program to invert LAI and LAD from a canopy reflectance model (Liang and Strahler, 1993a). The test results showed that a relative error between 1% and 5% or better was achievable for retrieving one parameter at a time or two parameters simultaneously.

Projection pursuit regression (Friedman and Stuetzle, 1981) is a new method for nonparametric multiple regression. The procedure models the regression surface as a

sum of general smooth functions of linear combinations of the predictor variables in an iterative manner. It can be simply described (Friedman and Stuetzle, 1981) as:

$$Y = a + \sum_{j=1}^{M} W_j \alpha^T X \tag{1.8}$$

where X, Y are the explanatory and predicted vectors, respectively, for vectors α, and a dimension M chosen by the user. It uses an additive model on predictor variables formed by projecting X in M carefully chosen directions. The projection pursuit regression is more general than standard stepwise and stagewise regression procedures, because it does not require the definition of a metric in the predictor space. Compared with the previously described LAI-VI equations (see 1.2.1), the projection-pursuit regression method makes a transform of VI first and then conducts the regression analysis. This method has not yet been used to estimate biophysical parameters from remotely sensed data. Therefore, it is very attractive to explore this method in the estimation of LAI.

1.3 Objectives of this study

This thesis seeks to develop new and improved methods for the estimation of LAI from remotely sensed data. Several topics will be addressed. First, raw satellite observation data were transformed into surface reflectance with a new atmospheric correction method. Second, the surface reflectance was used to derive surface LAI using a genetic algorithm optimization algorithm. Third, a hybrid RT inversion method was developed

and applied to Landsat ETM+ and Terra MODIS to retrieve LAI. The general outline is shown in Figure 1-1.

1.3.1 Development of new atmospheric correction algorithm

Atmospheric correction has been shown to significantly improve the accuracy of image classification and surface parameter estimation (Liang, 2003b). It is indispensable when one estimates surface parameters from satellite data which represent the combined radiance from surface and atmosphere. To derive surface biophysical properties from satellite measurements, the signals produced by the ground must be uncoupled from those by the atmosphere. Without such corrections, only correlative models can be developed to derive biophysical properties, unless one assumes that atmospheric effects are insignificant (Ouaidrari and Vermote, 1999).

Analytical decoupling of the atmosphere and the surface effects on reflectance is a challenging problem. Vegetation indices such as the NDVI (Tucker, 1979) significantly reduce the atmospheric effect because of its normalization effect (Kaufman and Tanré, 1992). Further reductions of atmospheric effects, including cloud effects, can be achieved by temporal compositing techniques in which several consecutive images are examined, and the value corresponding to the maximum vegetation index for each pixel is chosen (Holben, 1986; Kaufman, 1987; Kaufman and Tanré, 1992; Tanré et al., 1992).

One of the most popular methods is the 'dark-object' algorithm, which has been used for correcting surface radiance data from several satellites (Chavez, 1988). However, this method usually fails if there are no dense vegetation canopies or other dark objects in the imagery. To overcome this limitation, a new algorithm was developed for general atmospheric and surface conditions.

1.3.2 Development of new LAI inversion methods

Following the atmospheric correction, improved LAI estimation algorithms were developed. The first step was to find an algorithm which avoids the initial guess in the optimization and can find optimal results. Secondly, the advantages of both the physical RT inversion method and the non-parametric retrieval method were combined by developing a hybrid method.

An evolutionary algorithm was explored instead of the current optimization methods. The evolutionary algorithm makes use of the concept of natural selection among variants formed by genetic mutation and recombination (Goldberg, 1989). Genetic algorithms (GA) have been applied to a variety of remote sensing optimization problems in recent years (Jin and Wang, 2001; Zhuang and Xu, 2000). A linking interface was created in order to incorporate GA into the RT model inversion process. The GA-based inversion method was compared with current optimization algorithms, which will be explored later.

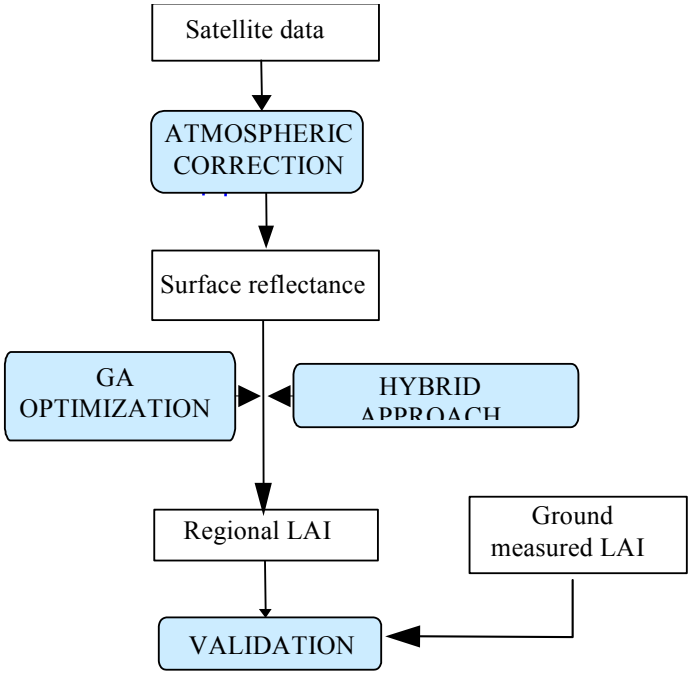

Figure 1-1 Flowchart of the LAI estimation processes.

Non-parametric methods showed very good relationships between surface reflectance and LAI. Neural network methods are more often used than projection pursuit regression (Friedman and Stuetzle, 1981). To take advantage of both RT inversion methods and non-parametric methods, a hybrid inversion method was developed. A large amount of field data was obtained for the non-parametric training. In addition, there is also a large amount of satellite data in the study area. The hybrid method was tested first with the 30 meters resolution Landsat ETM+ data. Subsequently, the method was extended to estimate LAI from Terra MODIS data.

1.3.3 Validation of LAI products

The algorithms were tested with different methods. The purposes of this validation were to: 1) Test the ability of satellite data to estimate LAI at different spatial scales; 2) Investigate the uncertainties and suitability of applying algorithms developed at point scale to local and regional scales; and 3) Compare the LAI values derived from remotely sensed data that have different spatial and spectral resolutions.

The NASA Earth Observation System (EOS) science teams have special validation programs (e.g. MODIS land team, MODLAND) for their products. In the MODLAND validation, general approaches involve either airborne or higher resolution satellite data, or both, coupled with ground-based measurements. Intensive study sites form a major component of the MODLAND validation plan, and they have evolved into the EOS

Land Validation Core Sites (Cohen and Justice, 1999; Justice et al., 1998a; Morisette et al., 2002). NASA's Airborne Science Program provides airborne platforms to carry NASA sensors such as the AVIRIS (Airborne Visible/Infrared Imaging Spectrometer), and EOS sensor simulators.

The LAI estimation algorithm was developed from point-scale RT simulation and was applied to pixel-based remote sensing data. It should be noted that differences exist between the parameters obtained at points (high-resolution) and averages for areas (low-resolution). Numerical experiments have shown that the retrieved LAI values from the satellite imagery could be quite different from the true LAI values if the surface is highly heterogeneous (Liang, 2000). Therefore, it is critical to examine whether the retrieved LAI values from low-resolution satellite data are equivalent to that upscaled from high-resolution ones.

The experimental site was the USDA Beltsville Agricultural Research Center (BARC) located in Beltsville, Maryland. This site, listed as one of the initial 24 NASA EOS land validation core sites (Morisette et al., 2002), is adjacent to the NASA Goddard Space Flight Center (GSFC) (39.03°N, 76.85°W). Detailed ground records include vegetation structural and optical characteristics and crop management information. Remotely sensed data in the study area include Landsat 7 ETM+, Terra MODIS, and SeaWiFS, etc. The GSFC operates a sunphotometer which provides the solar and atmospheric data.

Intensive validation work was carried out using the data collected in this study area. LAI estimated with these methods was compared with more conventional methods such as the LAI-VI relationships and some RT inversion methods.

1.4 Structure of the dissertation

The central objective of this research was to improve the estimation of LAI from remotely sensed data. After reviewing existing methods, the directions for this dissertation were pointed out in this chapter. A new atmospheric correction algorithm is introduced in Chapter 2. In Chapter 3, a new optimization method is explored by integrating RT models and genetic algorithms. A novel hybrid LAI estimation method is put forward in Chapter 4. This hybrid method is applied to estimate LAI from MODIS data in Chapter 5. Validation of LAI was not designed as a separate chapter, but was embedded in each relevant chapter. The final chapter summarizes the dissertation.

Chapter 2 Development of New Atmospheric Correction Algorithm

2.1 Introduction

As discussed in Chapter 1, satellite remote sensing plays a crucial role in the estimation of LAI at various spatial and temporal resolutions. However, use of remote sensing data to derive vegetation information is always hindered by the inherent non-vegetation information, such as atmosphere, which is also in the signal. Atmospheric correction becomes, therefore, indispensable and significantly improves the accuracy of surface parameter (e.g. LAI) estimation (Liang et al., 2001).

Conventional atmospheric correction algorithms always include some major assumptions which limit their general application. For example, histogram matching methods assume that the surface reflectance histograms in both clear and hazy regions are identical and thus perform poorly if the spatial distribution of aerosols varies dramatically (Richter, 1996a; Richter, 1996b). The commonly used dark-object methods need to detect pixels with very low reflectance (such as densely vegetated surfaces or water) and are, therefore, inappropriate in winter or non-vegetated regions (Kaufman and Sendra, 1988; Popp, 1995). The main objective of this chapter is to develop a new atmospheric correction technique that can handle general atmospheric and surface conditions.

This chapter begins with a general review of atmospheric correction methods in section 2.2, and then discusses the new methodology in section 2.3. The new method is applied to different remote sensing images such as ETM+, AVIRIS, MODIS and SeaWiFS. Field-measured data are used to validate the algorithm.

2.2 Existing atmospheric correction algorithms

All methods reported in the literature are roughly classified into the following groups: ground-based, image-based and atmospheric model-based methods. There is no distinct boundary among them. In fact, they are often used in an integrated fashion.

2.2.1 Ground-based methods

The ground-based methods rely on prior knowledge of surface reflectance for an image area. Atmospheric correction is performed by transforming image digital numbers (DN) into surface reflectance (ρ) through a linear regression:

$$\rho = b + g \times DN \tag{2.1}$$

where g and b are coefficients usually derived from sampled coherent surface reflectance and raw DN data. If surface measurements are not available, a priori reflectance values can be assigned to some ground objects (e.g. water bodies or wet soils) before using equation (2.1).

Ground-based reflectance measurements are crucial to the calibration of satellite sensors (Slater et al., 1987). The ground-based method assumes that the surface is Lambertian and the atmosphere is homogeneous. Its major limitation is that it requires simultaneous surface measurement which is often realistically impossible.

2.2.2 Image-based methods

Liang et al. (2001) have provided a review of current image-based methods. A well known one is the so-called "dark-object subtraction (DOS)" method. Dark-object subtraction techniques require a histogram examination of each band to determine the "take-off point"—the point separating shadowed and illuminated pixels (Chavez, 1988). Chavez (1988) provided an improved dark-object technique, which incorporates two factors: the wavelength dependence of atmospheric scattering and the relative radiometric sensitivities of the sensor's channels.

The main advantage of the image-based method is that it does not require in situ field measurements of surface reflectances and/or atmospheric optical depths or simulated atmospheric parameters. However, DOS algorithms require the existence of extensive dark objects such as dense vegetation, water and wet soils in the scene, and they do not work well for non-vegetated surfaces. Moreover, the DOS technique is not acceptable for many applications, especially those dealing with medium to bright reflectance values (Myneni et al., 1995).

2.2.3 Atmospheric model-based methods

Atmospheric correction can also be made with a coupled atmosphere and surface model based on the physical principles of solar flux transfer in an atmosphere-land surface system (Fraser and Kaufman, 1985; Lee and Kaufman, 1986; Tanré et al., 1979). Model-based methods attempt to perform explicit atmospheric correction by using atmospheric radiative transfer (RT) models. Generally, two steps are involved in this kind of model. The first step converts satellite-generated digital numbers to at-satellite radiances using instrument calibration coefficients. Next, at-satellite radiance is converted to surface reflectance by correcting for atmospheric effects (Moran et al., 1992).

Simplified model-based methods rely on assumptions, rather than measurements, of atmospheric conditions, but have varying degrees of accuracy (Dozier and Frew, 1981; Otterman and Fraser, 1976; Singh, 1988). One example of this is to convert at-satellite radiance to apparent reflectances (ρ'), directly, using (Tanré et al., 1987)

$$\rho' = \pi I' / \mu_0 F \tag{2.2}$$

where I' is the radiance measured at the sensor level, F is the solar flux, and $\mu_0=\cos\theta_0$ in which θ_0 is the solar zenith angle.

ρ' differs from ρ (in 2.1) because of two main atmospheric effects: absorption by atmospheric gases (principally water vapor and ozone) in the visible and near-infrared range and scattering by aerosols and molecules. For a flat and Lambertian surface under a horizontally homogeneous atmosphere, the relationship between the apparent and surface reflectances can be expressed by

$$\rho' = \rho_a + \rho_s T(\theta_0) T(\theta_v) / (1 - \rho_s S) \tag{2.3}$$

where ρ', ρ_a, ρ_s are planetary, atmospheric, and surface spectral reflectance, respectively. $T(\theta_0)$ is the total transmittance of the atmosphere from the sun to the pixel, and $T(\theta_v)$ from pixel to the sensor. S is spherical albedo of the atmosphere.

The model-based approach is more general than empirical methods such as the dark-object subtraction technique. The main deficiencies in the radiative transfer equation are its complexity and difficulty in parameter inversion. If the codes to solve the RT equations are used in conjunction with field measurements of atmospheric optical depth, the resulting reflectances are notably accurate (Holm et al., 1989; Moran et al., 1990). However, it is rather difficult, and sometimes not possible, to provide the aerosol optical depth data to solve equation (2.3).

As I have mentioned above, these methods are not independent of each other, but are integrated in practical applications. For example, the dark-object algorithm requires some basic assumptions about ground surface reflectances (Richter, 1997). Some

enhanced “dark-object” algorithms have combined the use of radiative transfer models for removing the atmospheric effects (Chavez, 1996; Kaufman, 1989; Kaufman and Tanré, 1996). Liang et al. (1997) successfully combined the dark-object algorithm and the lookup table approach for atmospheric correction of Landsat TM imagery over land.

2.3 New methodology

A new atmospheric correction algorithm was developed to overcome the limitations of previously discussed, existing atmospheric correction methods. Remote sensing images are often contaminated by atmospheric aerosols, clouds and cloud shadows. Conventional methods are useful for processing horizontally homogeneous haze. However, for heterogeneously distributed haze, they are problematic. A cluster match method was explored to handle this problem. The general procedure is illustrated in Figure 2-1. There are two major steps in this method. The first step, estimating the spatial distribution of aerosol loading, and the second, correcting the adjacency effects, are described in two subsections.

2.3.1 Processing heterogeneous haze

It is assumed that the image is only partly affected by haze. The first step of this algorithm is to delineate the clear and hazy regions based on the visible bands. Currently, there are several convenient methods to delineate hazy regions (Cahalan et al., 2001; Richter, 1996a; Zhang et al., 2002). In my study, a cluster analysis of the visible

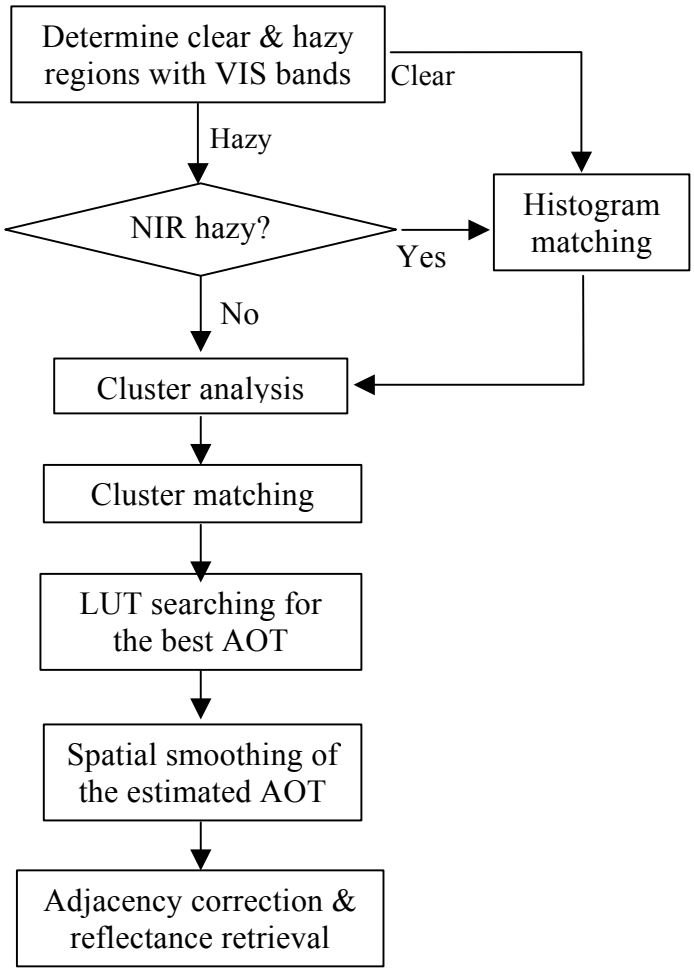

Figure 2-1 Flowchart of the new atmospheric correction algorithm. VIS: visible bands; AOT: aerosol optical thickness.

bands (band 1, 2, and 3 for ETM+) is performed. The image is classified into between ten and twenty primary clusters. These clusters are then aggregated into a few major classes (e.g. clouds, hazy areas, shadows, and clear regions), visually. A haze mask is then generated.

In equation (2.3), there are three unknowns: the atmospheric reflectance, the total transmittance and the atmospheric spherical albedo. To solve this equation, MODTRAN (Berk et al., 1999) is used to simulate the top of atmosphere (TOA) radiances for different atmospheric profiles and aerosol loadings and these are placed in a look-up table (LUT). The three unknowns are then determined for different atmospheric visibilities (Liang, 2001). My experiments show that a visibility of 50 km can well characterize the atmospheric conditions of the clear image. This visibility value works very well after retrieving and checking the initial minimum reflectances for different surfaces such as water body, dark forest, and wet soil. Thus, the aerosol optical depths are determined and the surface reflectances are retrieved for clear regions.

In some cases, near infrared bands are contaminated by haze. The algorithm starts an ancillary histogram-matching module to correct the aerosol effects in the infrared bands. The clear region determined above is used as a reference for the hazy region. Their respective reflectance histograms are assumed to be the same. The idea is to predict the reflectance of the hazy regions in visible bands by haze-free regions of the same cluster. This prediction is carried out on a cluster-by-cluster basis (hence its name: cluster matching). An unsupervised cluster analysis is conducted for the clear near infrared

bands for the whole scene. In this process, the number of clusters needs to be determined. Experiments with several cluster numbers (20, 30, 50, and 80) found no significant differences. For any given cluster, the surface reflectance in the haze region is assumed the same as that of the clear region. Therefore, the mean reflectance value of the clear region is used for the hazy region of the same cluster in the first step.

A spatial smooth operation is needed because the variations of aerosols are much smoother than the TM/ETM+ resolutions. In this study, a typical moving window of 5×5 was found to produce very good results in the spatial smoothing. The aerosol data were used to search the look-up table and interpolate the best coefficients. The surface reflectance can be finally retrieved with the aerosol map and equation (2.3).

Besides correcting aerosol scattering, attempts were made to remove the effects caused by cloud shadows. Because of the strong atmospheric scattering in the shorter wavelengths, shadows are more distinct in the near-infrared bands than the visible bands. This fact is important for the algorithm to process the shadow regions based on the same rationale used for the hazy regions. This time, the shadows are identified from unsupervised classification of the near infrared bands. The cluster analysis and cluster matching processes are performed for the visible bands. The average reflectance of the clear region is used for the shadow region of the same cluster. The look-up table constructed before is used here to derive the aerosol distribution map and estimate primary surface reflectance.

In this procedure, the surface properties of each cluster in the hazy region are assumed to be the same as the clear region. There are other ways to construct a relationship between the hazy and clear regions. The neural network (NN) method was found to be of limited use. The clear region was divided into training and test subregions. The trained NN, using data from the training subregion, shows that non-linear relationships exist between bands 4, 5, 7 and bands 1, 2, 3 ($r > 0.98$). However, there was a considerable amount of scatter in the test subregion. Different parameters of the NN were tried; they all performed poorly. Both radiance and reflectance data sets were used in the experiment and predicted the same poor results. In fact, reflectance data gave poorer results.

2.3.2 Correcting surface adjacency effects

The adjacency effect is caused by multiple reflections between the atmosphere and land surface. In high-resolution images, the pixel values over a heterogeneous landscape are affected by their neighboring pixels resulting in typically hazy images without contrast. This problem has been extensively investigated (Kaufman, 1989). Adjacency effect correction methods can be grouped into two broad categories: (1) using the atmospheric point spread function (PSF); and (2) developing empirical formulae.

The PSF describes the physical, optical and electronic properties during the remotely sensed data acquisition process. If the PSF of a scene is known, the inverse function can be used to correct the data to spatially specific surface reflectances. Different methods have been explored to calculate the atmospheric PSF, such as the Monte-Carlo

simulations (Miesch et al., 1999; Reinersman and Carder, 1995) or radiosity simulations (Borel and Gerstl, 1992). However, calculating the atmospheric PSF is computationally intensive. A deconvolution calculation is necessary to reconstruct the real image and it requires considerable computer resources. For high-resolution satellite imagery (e.g., ETM+ or SPOT), the validity of using the atmospheric PSF method is still questionable because a simple deconvolution cannot account for multiple reflections between the atmosphere and the surface.

Because of the difficulty of the PSF method, empirical methods are often used. Pinilla Ruiz (2002) approximated the PSF with linear step functions and devised a set of deconvolution filters for each image from its PSF. Some researchers simplified the process by taking into account only several neighboring pixels for calculating the effective reflectance (Singh and Cracknell, 1986). Popp (1995) calculated the contribution of the environment surrounding a pixel using

$$A_F = A_i - \sum_{n=1}^{Nn} \xi((2n+1)s)(\overline{A_n} - \overline{A_{n-1}}); \overline{A_0} := A_i \tag{2.4}$$

$$\xi(s) = 0.7\delta^R e^{-s/2H^R} + \delta(0.37e^{-s/H^A} + 0.32e^{-s/6H^A}) \tag{2.5}$$

where A_i and A_F are reflectances before and after adjacency processing for pixel i, s is the pixel size, ζ is the approximated environmental contribution, δ^R and δ^A are the optical depths of Rayleigh scattering and aerosols, H^R and H^A are the respective scaling

heights of Rayleigh scattering and aerosols, and N_n is the total number of surrounding pixels considered.

Equation (2.4) is much easier compared with conventional PSF methods and produces a reliable result (not reported here). However, its application involves significant computation, especially for the iterative transfer fraction in (2.5). In addition, the accuracy of this algorithm relies on the acquisition of ancillary data (aerosol loading, water vapor content, aerosol type, vertical profiles, etc.) and their accuracies. Those ancillary data are usually difficult to estimate without field measurements.

Based on extensive numeric simulation using a three-dimensional radiative transfer model (Liang et al., 2001), a simple convolution function $g(s)$ was developed to produce the effective reflectance

$$\rho_e = \frac{\int g(s)\rho(s)ds}{\int g(s)ds} \tag{2.6}$$

where $\rho(s)$ is the reflectance calculated without accounting for the adjacency effect and s is the distance (km) from the central pixel. The fitted empirical function is

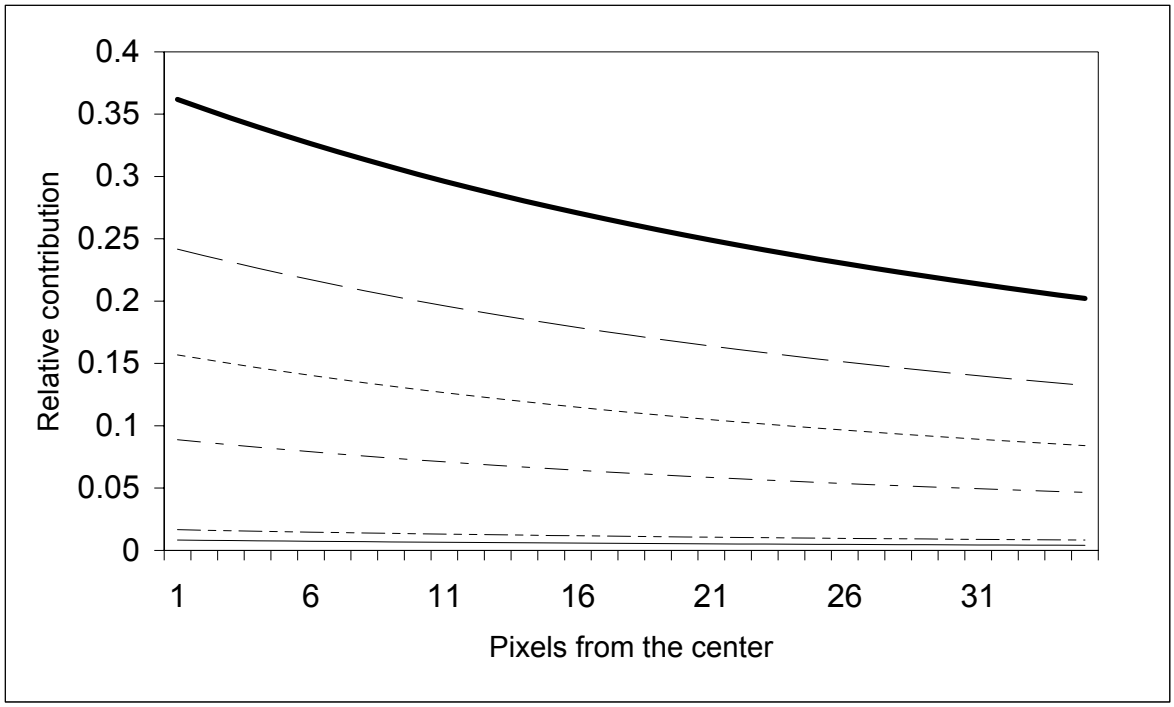

Figure 2-2 Relative contribution of the neighboring pixels from equation (2.7). The aerosol optical depth (τ) is from May 11, 2000. The six lines are for band one to six downward.

$$g(s) = f_1(\tau)\exp(-1.424s) + f_2(\tau)\exp(-12916s) \tag{2.7}$$

where τ is the aerosol optical depth, and

$$\begin{aligned} f_1(\tau) &= 0.003\tau \\ f_2(\tau) &= 0.071\tau^3 - 0.061\tau^2 - 0.439\tau + 0.996 \end{aligned} \tag{2.8}$$

One can see that equations (2.6), (2.7) and (2.8) are significantly easier to implement than (2.4) and (2.5). These equations are general and suitable for all the spectral bands.

In practice, they are very effective to process high-resolution images over a large area (Liang et al., 2001).

The first term of the right side of (2.7) represents the contribution from background pixels, and the second term represents the contribution from the central pixel and its nearest neighbors. An example of the normalized functions of (2.7) is illustrated in Figure 2-2. One can see that the adjacency effect degrades as the distances to the central pixel increase. Among the six ETM+ bands, the visible bands are more affected by the adjacency effect than the near-IR bands.

2.4 Results and validation

2.4.1 ETM+ results

The new method was used to correct ETM+ images over the study area at BARC. The surface reflectance values after atmospheric correction are represented in Figure 2-3. This image was acquired on July 28, 1999. The image size was 1500×1500 pixels. The atmospheric correction was performed by assuming a Lambertian and homogeneous surface and a standard rural atmosphere. Figure 2-3b shows the reflectance image after removing hazy and cloudy regions. Figure 2-3c is the image after removing shadows. The results demonstrate a great improvement compared with the original reflectance image (Figure 2-3a). All haze, thin clouds and shadows have been effectively removed. A difference

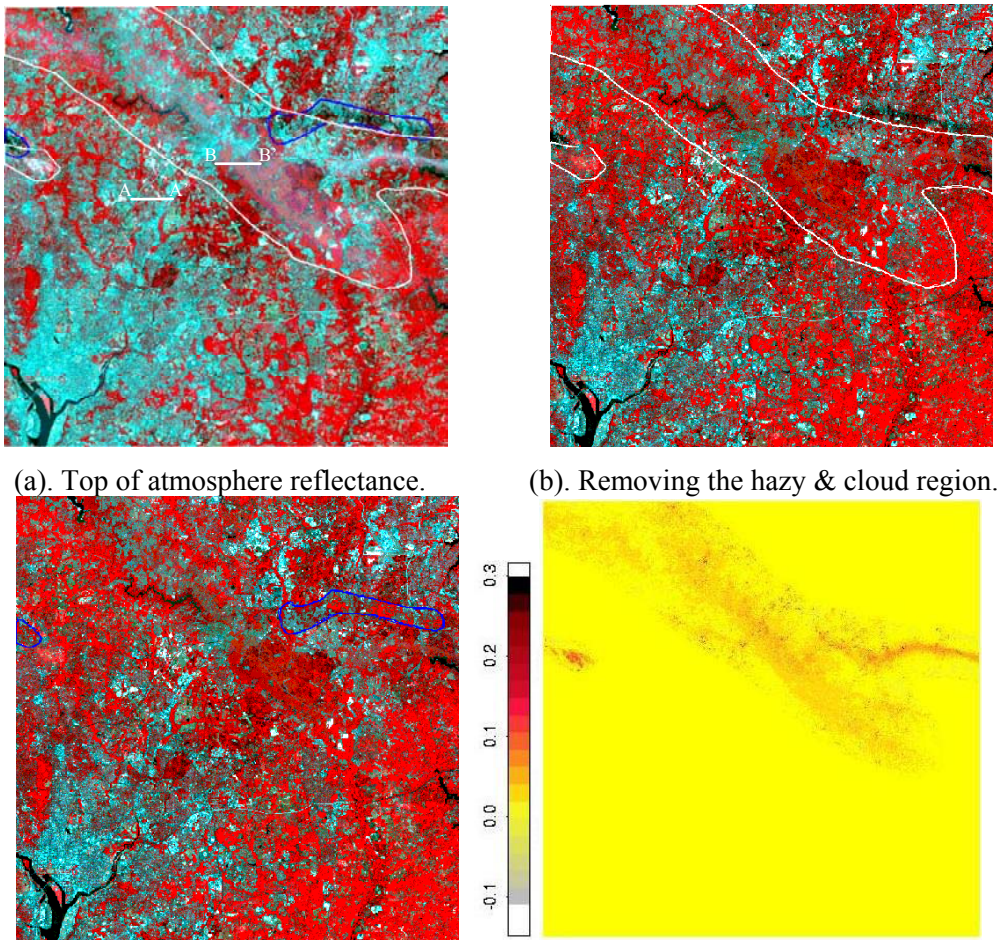

(a). Top of atmosphere reflectance.

(b). Removing the hazy & cloud region.

(c). After shadow processing.

(d). Difference image of (a)-(c), band 1

Figure 2-3 False color composite (RGB432) and difference images of Landsat ETM+ reflectances at the BARC study area (July 29, 1999). White/blue polygons in (a) are hazy/shadow regions, respectively. Lines AA' and BB' are used in Figure 2-4.

image is shown in Figure 2-3d which clearly displays the areas that are greatly improved after correction.

Figure 2-4 provides a more detailed look at the study area at BARC. The image of 512×512 size was acquired on May 11, 2000. Some large shadow patches were removed after processing. Two transects were selected to quantitatively examine the atmospheric correction effects for both 1999 and 2000. Line AA' crosses a developed area and was in a cloud shadow in 2000 (Figure 2-4a). Line BB' goes through a forest and was in a hazy region in 1999 (Figure 2-3a). Statistical comparison of the ETM+ images before and after atmospheric correction shows that in the shadow region, the reflectance increased for band 4 (NIR) after atmospheric correction (Figure 2-4c). In the haze region, surface reflectance decreased for band 1 (blue) (Figure 2-4d). Quantitative comparison of the atmospherically corrected ETM+ reflectances and field-measured reflectances will be investigated in the following subsection.

2.4.2 Validation

In the study area at BARC, large amounts of field data were collected, spanning years, to validate the atmospheric correction algorithm. After visually examining the atmospheric correction, the estimated ETM+ reflectance is compared with the field-measured reflectance for different land cover types. One example is given in Figure 2-5.
The atmospherically corrected reflectances are represented with crosses at the ETM+ central wavelength. They were obtained from the average reflectance of each plot. At

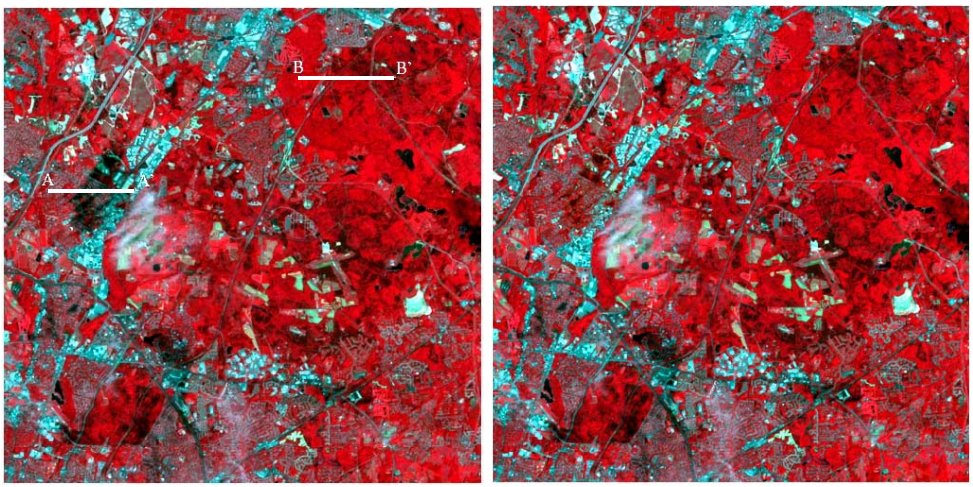

(a) (b)

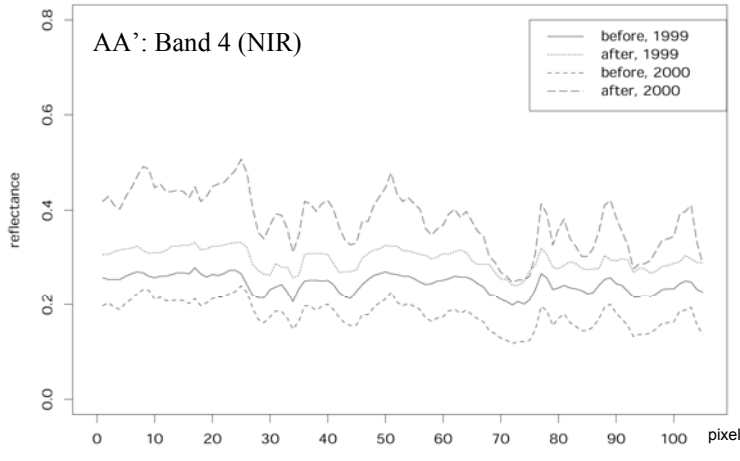

(c)

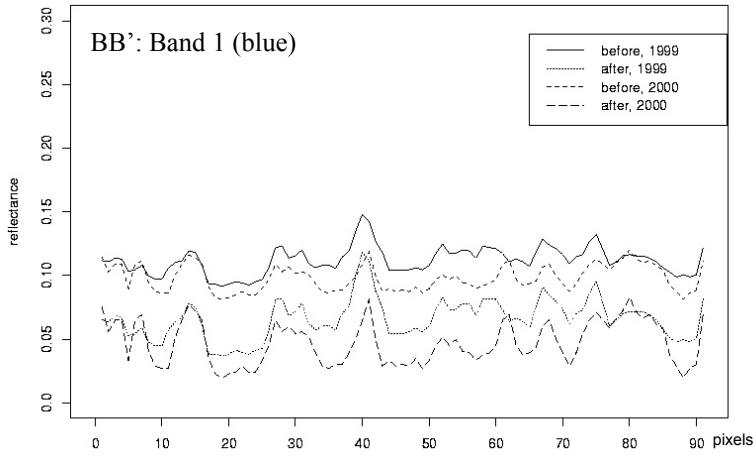

(d)

Figure 2-4 False color composite of ETM+ (RGB432) before (a) and after (b) atmospheric correction The image was acquired on May 11, 2000 and has a size of 512×512. (c) the NIR reflectance profiles of line AA'. (d) the blue band reflectance profiles of line BB'.

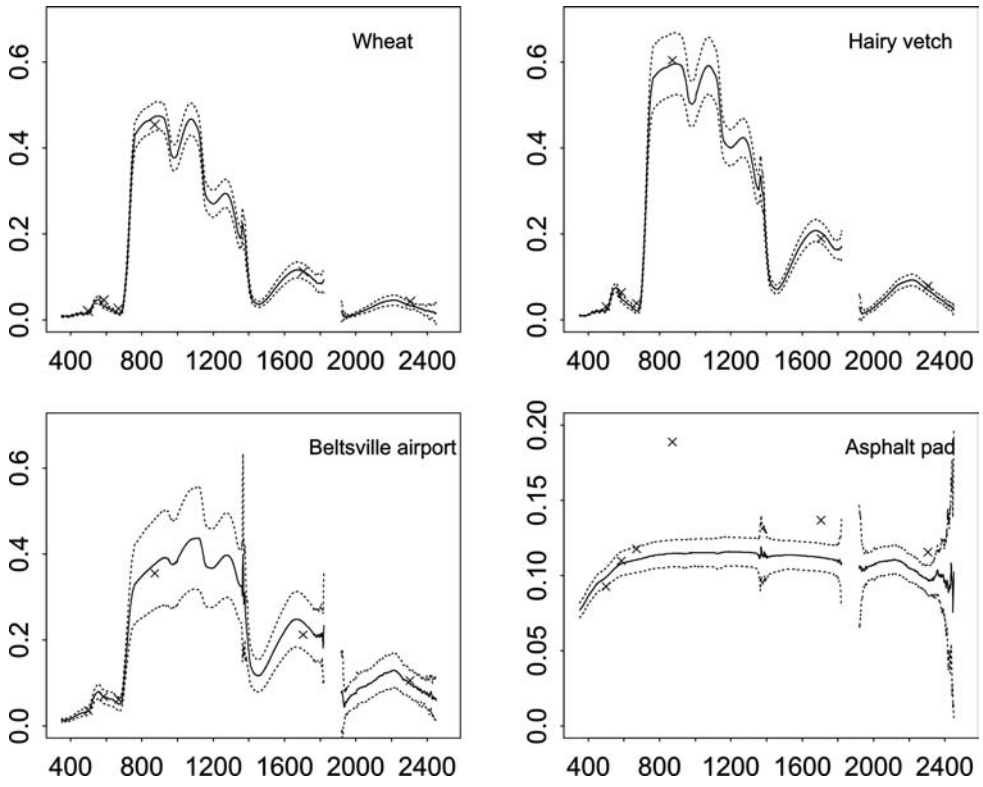

Figure 2-5 Comparison of retrieved surface reflectance from ETM+ (crosses) and measured (lines) reflectance at different sites on May 11, 2000. The solid line is the mean ASD reflectance and the dotted line is ± one standard deviation away from the mean.

these sites, the average ASD (Analytical Spectral Devices (ASD), 2000) measurements are shown with solid lines in the figure. ASD measures the reflectance over 350-2500 nm wavelengths. The solid line is the mean reflectance, and the two dashed lines represent the mean reflectance plus and minus one standard deviation. The gaps are the absorption bands where ASD sensors do not work because of high noise. In this figure, we can see that the retrieved ETM+ reflectances match well with the ASD measurements. Most ETM+ reflectances are within the one standard deviation range of the ASD measurements. The only exception is on asphalt. Because the ETM+ pixels are mixed with surrounding forests, they differ greatly from the point asphalt measurements.

Figure 2-6 compares the two sets of reflectances at ETM+ bands. The ASD measurements are integrated into the corresponding ETM+ bands using the ETM+ sensor spectral response function. Both reflectances agree quite well with each other (all R^2 are larger than 0.883). The absolute errors are not larger than 0.041 and the relative errors are less than 10%. This result is very satisfactory considering the many uncertainties (e.g., aerosol scattering model, measurement errors and surface heterogeneity) in the atmospheric correction process.

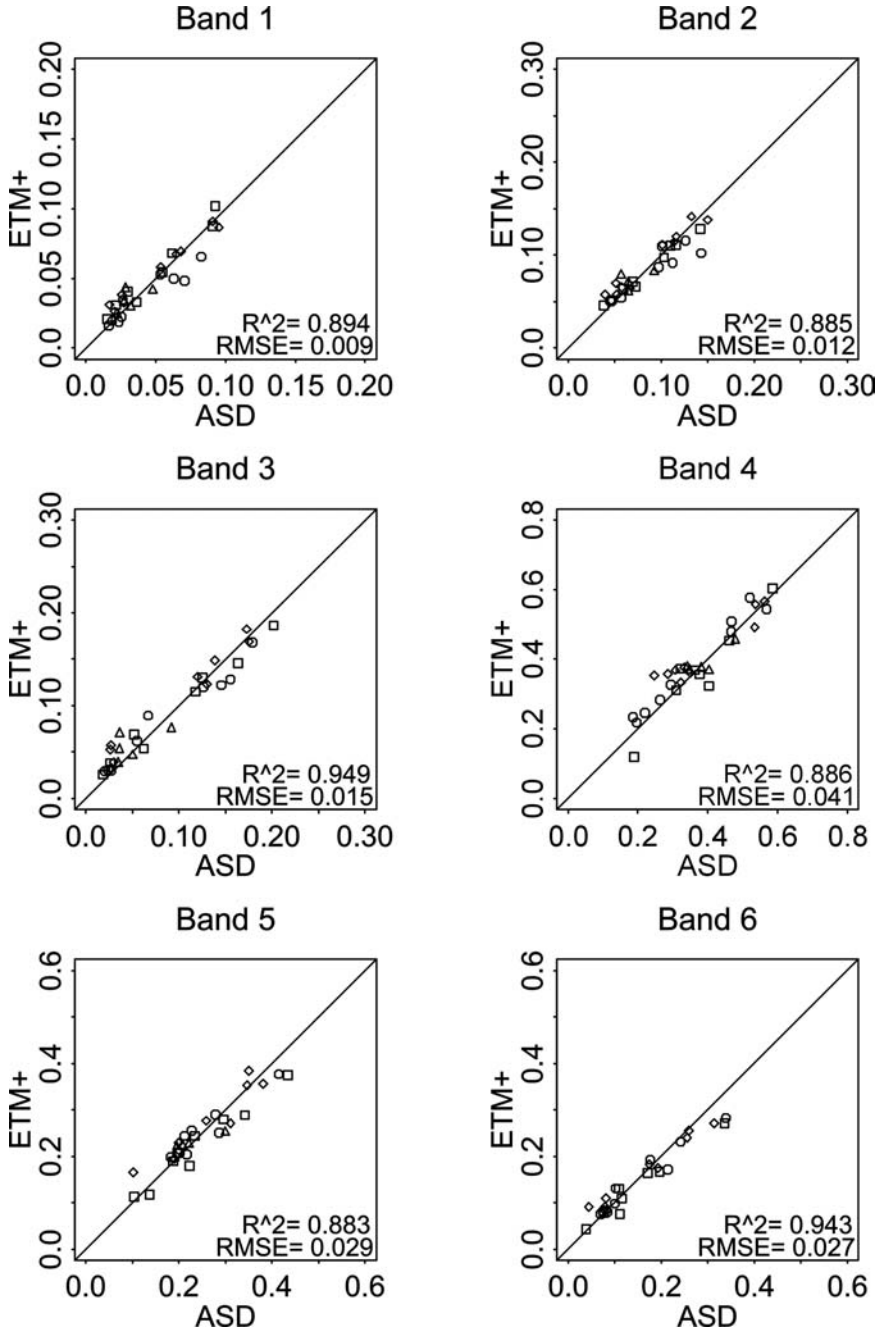

Figure 2-6 Comparison of the retrieved ETM+ reflectance and the aggregated ASD measured reflectance acquired on four dates: May 11, 2000 (□), Oct 2, 2000 (○), Apr 28, 2001 (◇) and Aug 2, 2001(△).

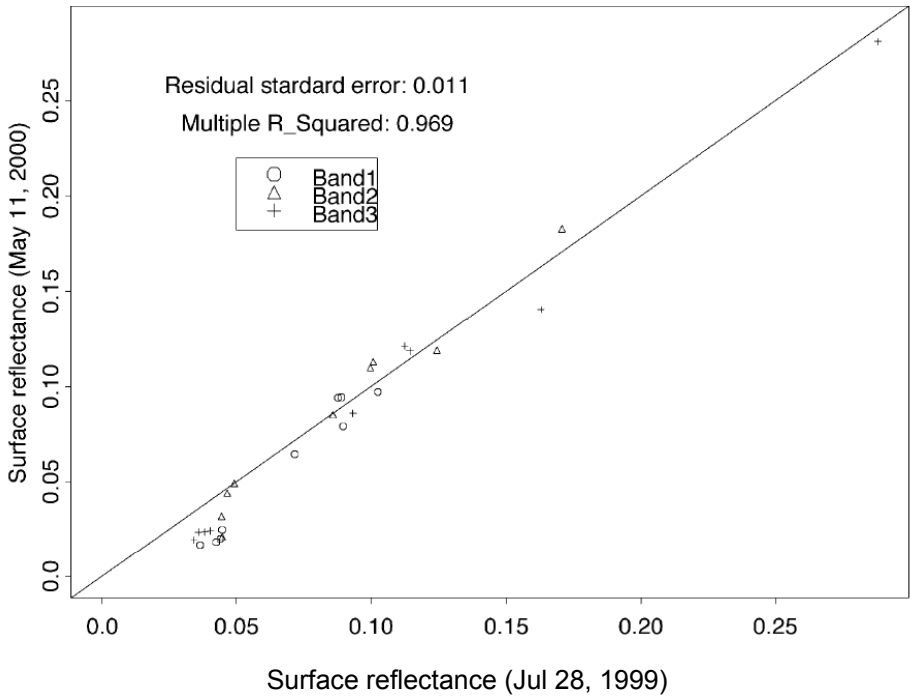

Figure 2-7 Comparison of the surface reflectance of 'invariant' objects from three ETM+ bands of May 11, 2000 and July 28, 1999.

Some ground objects have very stable spectral characteristics over time, which can be used for verifying the atmospheric correction algorithm. Figure 2-7 compares the reflectances of those invariant objects acquired at two dates (July 28, 1999 and May 11, 2000). The two reflectance images were registered together and nine plots were selected in total on each image including conifer forest plots (2), lake plots (2), highway intersection (sandy pavement) (1), Beltsville airport (concrete) (2) and asphalt plots (2). The mean reflectance of a 3×3 pixel window for each plot was calculated and compared. These invariant objects show strong agreement with each other. The maximum deviation is about 0.02. The residual standard error is 0.011, and the R^2 is 0.969.

2.5 Extensions to other areas and sensors

The above descriptions demonstrate that the new atmospheric correction algorithm worked well for ETM+. The cluster-match atmospheric correction method is especially advantageous for processing images acquired in winter when the dark-object methods fail because there is usually no dense vegetation available. Figure 2-8 shows some true color composite ETM+ imagery of agricultural fields before and after atmospheric correction. These three images are of 600×600 pixels acquired in South Dakota (row 31/ path 30) on November 17, 1999. The solar zenith angle was 63.51º and the azimuth angle was 162.83º. Correcting these images is challenging because there are no field-measured aerosol data or water vapor content in this region. Thus, a clear visibility value (50 km) was used to represent the general aerosol characteristics of the clear regions. The aerosol patterns in these images were very different. After correction, most of the hazy regions were cleaned up. The results could be validated quantitatively using ground measurements for this area.

The algorithm was extended to other sensors such as the airborne AVIRIS, spaceborne MODIS and SeaWiFS. These three sensors have very different spectral and spatial characteristics than ETM+. Since the new algorithm is particularly advantageous for processing heterogeneously distributed aerosols, three hazy images were obtained. AVIRIS and SeaWiFS produced images over the core study area, while the MODIS image came from northeast China since an ideal test image was hard to acquire for the study area.

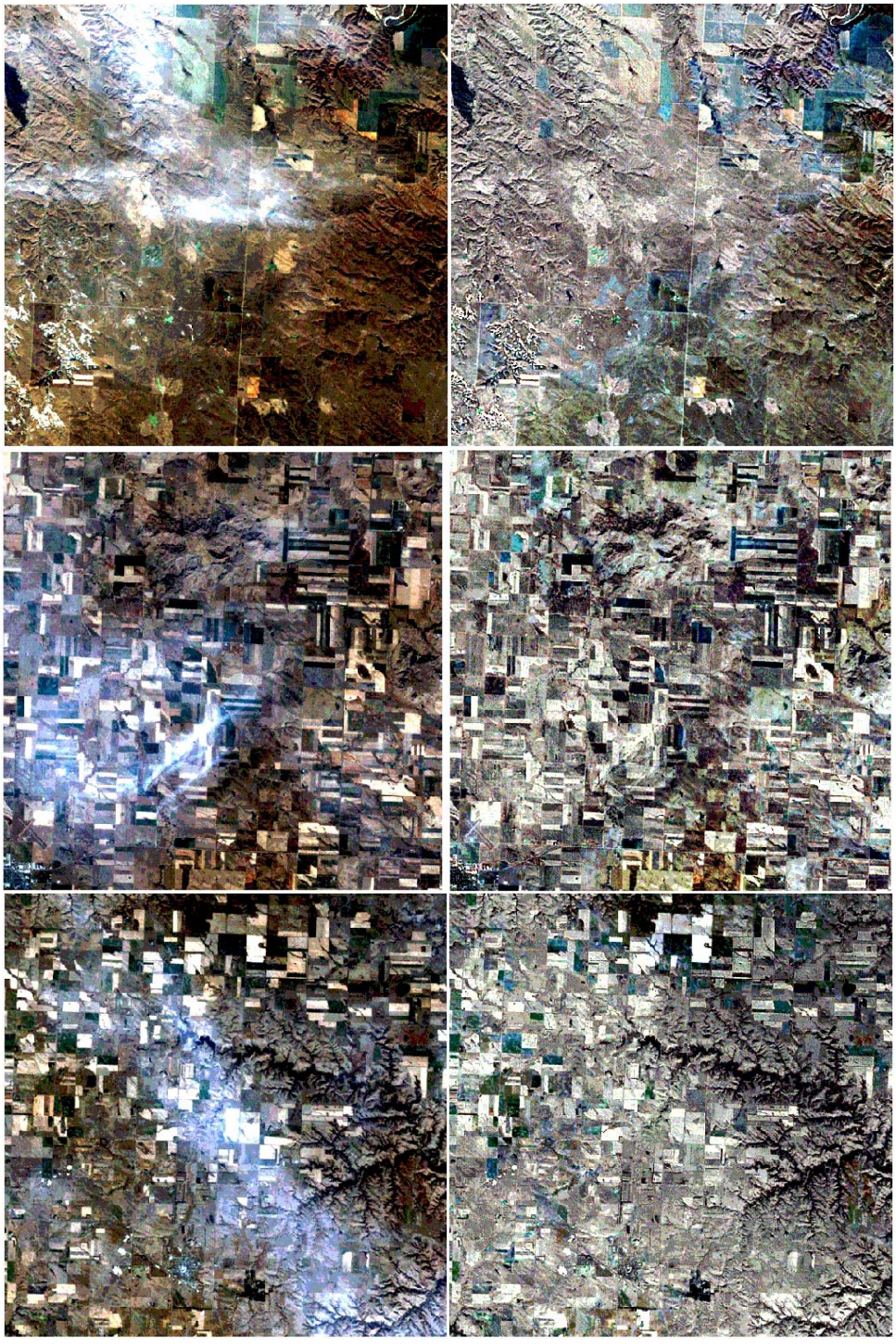

Figure 2-8 Examples of three ETM+ scenes (Nov 17, 1999) before (left column) and after (right column) atmospheric correction. The images are of true color composites (RGB321).

2.5.1 AVIRIS

AVIRIS is a hyperspectral optical sensor that delivers the calibrated images of the upwelling spectral radiance in 224 contiguous spectral bands with wavelengths from 400 to 2500 nanometers (Green et al., 1998). The AVIRIS image was acquired on May 11, 2000 over the study area. The ground resolution was 20 meters. The AVIRIS data provide abundant near-infrared and middle IR radiometric information which greatly helps atmospheric correction. It was found that this method works very well in the study area (Figure 2-9). Figure 2-9a&c are raw images contaminated by heavy haze. The haze masked residential areas, roads, parking structures and other constructed areas. After processing with the new atmospheric correction method, these ground targets cleared remarkably (Figure 2-9b&d). The corrected images are useful for hyperspectral analysis and urbanization research.

2.5.2 MODIS

MODIS has one more near-IR band (1.63-1.65 μm) than ETM+ (Justice et al., 1998b). This helps the algorithm in the cluster-analysis and cluster-match procedures by providing more consistent classification. Figure 2-10 shows an example over the northeastern coast of China, acquired on May 7, 2000. The image is of 400×400 at 1 km resolution. Figure 2-10a&b compare the blue band imagery (band 3) before and after atmospheric correction. Figure 2-10c&d compare the standard false-color composite images using band 2, 1 and 4 as red, green and blue. The differences are significant,

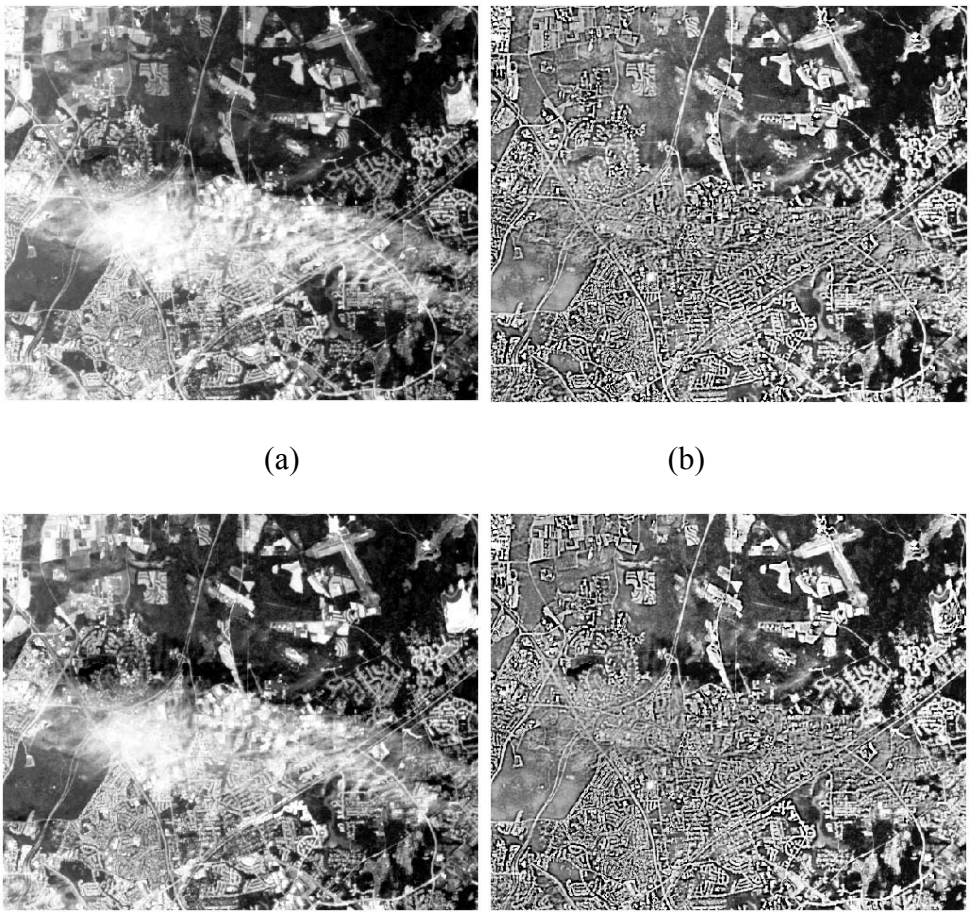

(a) (b)

(c) (d)

Figure 2-9 AVIRIS images (May 11, 2000) of the BARC study area. (a) and (b) are band 14 (500nm) before and after atmospheric correction using the cluster match method respectively. (c) and (d) are band 26 (618 nm) before and after processing. The image is 512 (lines) × 614 (columns).

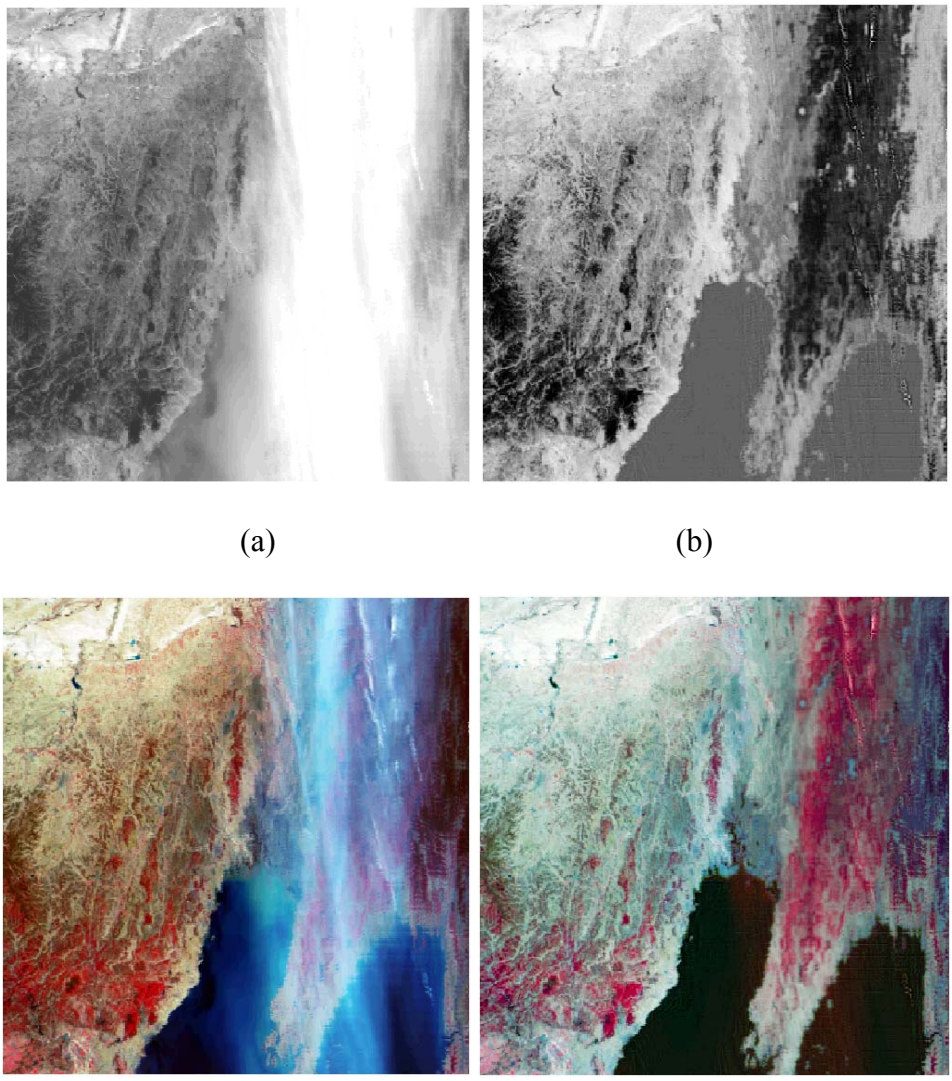

(a) (b)

(c) (d)

Figure 2-10 MODIS band 3 (blue) before (a) and after (b) atmospheric correction, and false color composite image (RGB214) before (c) and after (d) correction. The image size is 400×400.

particularly over blue band: haze and thin clouds have been effectively removed in the corrected imagery. The image color has been visually enhanced after processing. If surface reflectances were available, the correction could be evaluated quantitatively.

The MODIS standard LAI algorithms do not process cloud and haze areas such as in this example, because of the algorithm's limitations. Figure 2-10 shows that these small clouds and haze can be removed and thus these MODIS data can still be used to retrieve LAI.

2.5.3 SeaWiFS

SeaWiFS is designed for observing ocean productivity. It has eight bands total, six in the visible spectrum*. The rich visible information helps the algorithm in hazy/clear region demarcation. Unfortunately, there are only two near-IR bands. Theoretically, more near-IR bands will help identify ground cover types in the clustering analysis. Because SeaWiFS imagery has a much coarser spatial resolution, the number of clusters used in this algorithm can be smaller than for ETM+ imagery. Figure 2-11 shows an image of the Washington, DC area acquired on November 6, 2000. The black/white image is band 2 (blue), and the color imagery is composited using bands 7, 5 and 3 as red, green and blue. The hazy area in the lower part of the image has been effectively removed. Because of the lack of IR bands in the cluster analysis and fewer cluster numbers, the image reveals some patchy effects after correction. Therefore, further improvements are still needed for SeaWiFS correction.

---

* *http://seawifs.gsfc.nasa.gov/SEAWIFS.html*

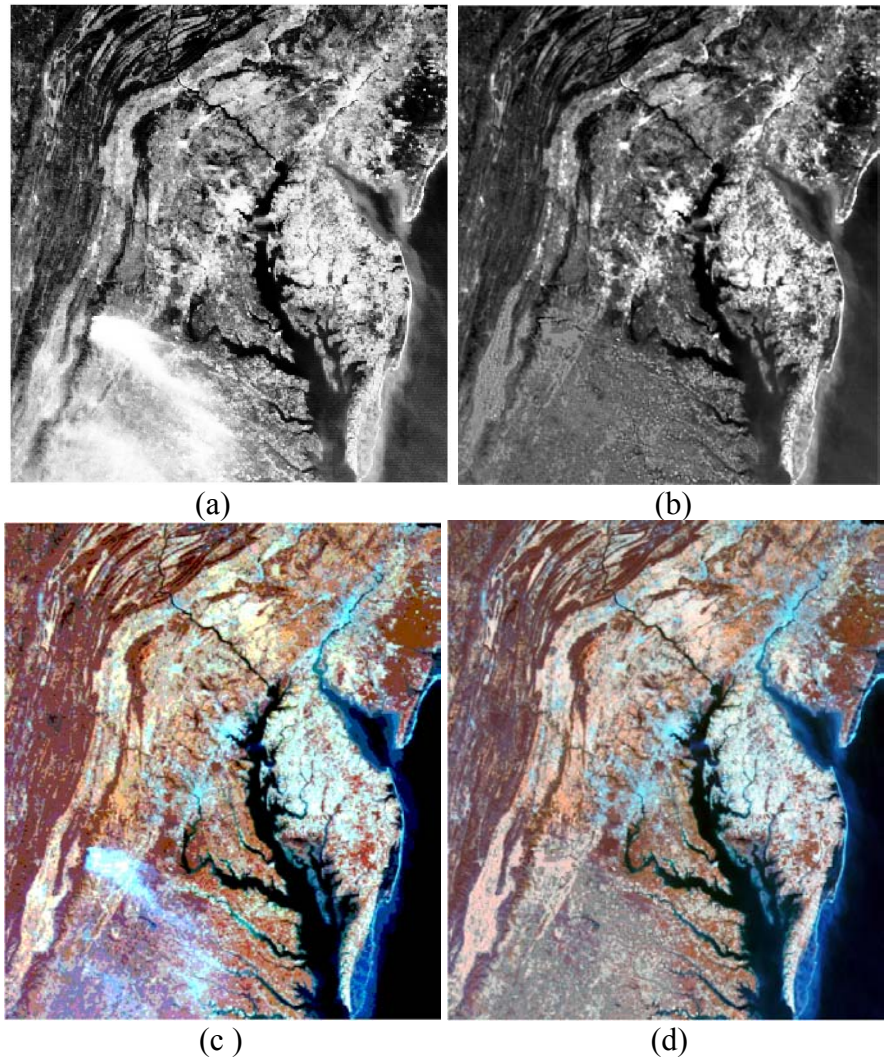

Figure 2-11 SeaWiFS band 2 (blue) before (a) and after (b) atmospheric correction, and false color composite image (RGB753) before (c) and after (d) correction. The image size is 512×512.

2.6 Summary

A new atmospheric correction algorithm has been developed and applied to correct some remotely sensed images in this study. A cluster analysis was conducted using infrared bands. The mean reflectance of the visible bands in a clear region was used to represent the reflectance of the same cluster in a hazy region. The aerosol optical thickness of the hazy region was estimated using the look-up table created with MODTRAN. The aerosol map was smoothed with an average filter. Afterwards, the surface reflectance was calculated with atmospheric radiative transfer function (2.3).

The results of the application of this method to ETM+ imagery have shown that this method works very well. All haze, thin clouds and shadows can be removed effectively after correction. Validation with surface measured reflectance proved that this new algorithm can be used to accurately retrieve surface reflectance ($R^2 \geq 0.883$).

This algorithm has been extended to correct AVIRIS, MODIS and SeaWiFS imagery. Although there are no ground data to evaluate the accuracy of the correction algorithms, visual examples in this chapter have shown that the corrected images have been greatly improved. More near-IR bands facilitate the algorithm in the cluster-analysis process.

Chapter 3 LAI Retrieval Using a Genetic Algorithm

3.1 Introduction

In the first chapter, LAI estimation methods through canopy radiative transfer (RT) model inversion were reviewed. Conventional inversion methods determine the set of canopy biophysical parameters such that the computed reflectances optimally fit the measured ones (Myneni et al., 1995). Some optimization methods were introduced in that chapter. These methods are generally available in standard software libraries (e.g. Press et al., 1992) and are commonly used for complex, nonlinear formulations, such as in canopy reflectance modeling. One of their major limitations is multiple solutions at local minima, leading to large inaccuracies in the estimation of biophysical parameters. Moreover, the inversion may not always converge (Jacquemoud, 1993). These limitations motivated me to examine new inversion methods.

Genetic algorithms (GA) have been applied to a variety of optimization problems in remote sensing. The fundamental concept of GA is based on natural selection among variants formed by genetic mutation and recombination (Goldberg, 1989). Genetic algorithms have been developed for retrieval of land surface roughness and soil moisture (Jin and Wang, 2001). Lin and Sarabandi (1999) used GA as a global search routine to characterize the input parameters (such as tree density, tree height, trunk diameter, and soil moisture) of a forest stand. The inversion was tested with measured single-polarized SAR (Synthetic Aperture Radar) data. Zhuang and Xu (2000) tried to retrieve LAI from thermal infrared multi-angle data using GA. But the resulting LAI values differed greatly

from field data (retrieved 2.9 vs. field 1.4). A genetic algorithm was applied to the numerical optimization of a crop growth model using AVHRR data (de Wit, 1999). The 'synthetic' model output was compared with the 'measured' AVHRR signal and the goodness-of-fit was used to adjust the crop model parameters to find a better set of parameters. Renders and Flasse (1996) compared the conventional optimization methods (Quasi-Newton and Simplex methods) and the GA method, and designed new hybrid methods to combine the advantages of different optimization methods. The new methods were tested with simulated data based on the model of Verstraete et al. (1990) but they were not tested and applied in any practical remote sensing scenario.

For a conventional optimization inversion algorithm, the final solution is often affected by the initial values. Therefore, "the solution obtained through an iterative process is reliable only if the space of initial conditions is sufficiently scanned" (Bicheron and Leroy, 1999). The most significant advantages of the GA are that it avoids the initial guess selection problem and provides a systematic scanning of the whole population and several acceptable local solutions such that a global optimum solution could be identified. To my best knowledge, no work has been done to retrieve LAI from a canopy RT model with a GA optimization method. In this chapter, a GA is explored to invert LAI from a widely used canopy RT model (Kuusk, 1995b; Kuusk, 2001). In contrast to previous GA optimization in remote sensing applications, this study: 1) makes use of reflectances derived from high resolution, atmospherically corrected Landsat ETM+ data; 2) uses reflectance data to construct the merit function because they can be directly measured from ground and indirectly estimated from satellite measurement; 3) retrieves

LAI using a genetic algorithm from a canopy RT model; 4) validates the LAI values with field measurements, which many studies lacked.

This chapter begins with an introduction of the genetic algorithm and the canopy RT model. It is followed by a description of the experimental plans. The results are presented in section 3.4. A brief summary is given at the end of the chapter.

3.2 The genetic algorithm and the radiative transfer model

My objective is to estimate LAI using a GA in conjunction with a canopy RT model from field-measured reflectance and the retrieved ETM+ spectral reflectance. In this section, the GA and the canopy RT models are introduced. GA simulates the process of natural selection and evolutionary genetics. A detailed description of GA can be found in Goldberg (1989) and Davis (1991). A typical algorithm is composed of a number of *ad hoc* steps, including:

1) Determination of the parameter space (e.g., x_1, x_2, …);
2) Development of an arbitrary encoding algorithm to establish a one-to-one relationship between each chromosome and the discrete points of the parameter space (e.g., x_1: 1~10, x_2: 1-100, …);
3) Random generation of a trial set of parameters known as the initial population (e.g., x_1=3.5, x_2=57, …);

4) Selection of high-performance parameters according to the objective function known as natural selection (e.g., x_1 and x_2 are selected);
5) Mating and mutation of the parameters for the next generation (e.g., x_1=3.2, and x_2=53 work best);
6) Repeat of steps 4 and 5 until the convergence is reached (x_1, x_2 values are the solutions).

A simple GA model includes reproduction, crossover, and mutation. These genetic operations alter the composition of 'offspring' during reproduction. A complete GA also needs other parameters, such as population size, probabilities of applying genetic operators, etc. Determining these GA operators and parameters can be a highly difficult and time-consuming task. The definition of an optimum set varies from task to task. Investigation of the variability of these parameters is not intended. Thus, a trial-and-error process was carried out in this experiment to get the more suitable values for some parameters. For others, existing settings will be used which have been reported to work well across a variety of applications.

The genetic software used in this study, GENESIS (Grefenstette, 1990), is a package frequently mentioned in the GA literature. GENESIS is easy to use and it provides default parameter settings that are robust for a variety of applications. In the GA, each chromosome could be represented with binary or real numbers. Using the real number is more popular and was applied in this experiment. The chromosome is composed of genes. Each gene (or free parameter) takes a range of floating point values, with a user-

defined output format. The existing settings in GENESIS are used in the experiment, which work reasonably well across a variety of applications (Clark and Cañas, 1995).

Many canopy RT models have been inverted to obtain the land surface biophysical parameters (Goel and Kuusk, 1992; Kuusk, 1994; Liang and Strahler, 1994b; Privette et al., 1994; Verhoef, 1984; Verstaete et al., 1990). I focus on the popular Markov chain reflectance model (MCRM) developed by Dr. Kuusk (Kuusk, 1995b; Kuusk, 2001). The MCRM calculates the angular distribution of the canopy reflectance for a given solar direction from 400-2500nm (Kuusk, 1995b). This model incorporates the Markov properties of stand geometry into an analytical multispectral canopy reflectance model (Nilson and Kuusk, 1989). The inputs of the forward MCRM are summarized in Table 3.1. The solar zenith angle θ_i represents the value when the ETM+ data were acquired. Jacquemoud et al. (1996) provide the leaf water content and leaf dry matter content (protein, cellulose and lignin). For ETM+ data, only nadir viewing angle was considered. In this case, the sensitivity of the inversion to the hot-spot parameter S_L (=0.15) is very low. Two leaf angle distribution parameters are set to zero (e=0; θ_m=0), assuming a spherical leaf orientation. Therefore, there is no dependence on the leaf angle θ_m (Kuusk, 1995a). Six free parameters were identified: LAI, S_z, C_{ab}, N, r_{s1} and r_{s2}. Their effective ranges are displayed in Table 3.1. The MCRM calculates the nadir reflectance with the spectral resolution of 5 nm.

Table 3.1 Input parameters to the canopy radiative transfer model, MCRM.

Parameters	Symbol	Values
External parameters		
Solar zenith angle	θ_i	27.8º, 46.6º, 31.4º, and 30.2º
Angstrom turbidity factor	τ	0.1
Canopy structure parameters		
Leaf area index*	LAI	0 ~ 10.0
Leaf linear dimension/canopy height ratio,	S_L	0.15
Markov parameter describing clumping*	S_z	0.4 ~ 1
Eccentricity of the leaf angle distribution	E	0.0
Mean leaf angle of the elliptical LAD	θ_m	0.0
Leaf spectral and directional properties		
Chlorophyll AB concentration (ug/cm^2) *	C_{ab}	20 ~ 90
Leaf equivalent water thickness (cm)	C_w	0.01
Leaf protein content (g/cm^2)	C_p	0.001
Leaf cellulose and lignin content (g/cm^2)	C_c	0.002
Leaf structure parameter*	N	1 ~ 3.
Soil spectral and directional properties (Price, 1990)		
Weight of the 1st Price function*	r_{s1}	0 ~ 1.0
Weight of the 2nd Price function*	r_{s2}	-1.0 ~ 1.0
Weight of the 3rd, and 4th Price function	r_{s3}, r_{s4}	0.0

* free parameters

3.3 Experimental study

The approach sought the best match between the measured reflectance and the computed values by a canopy RT model. Figure 3-1 shows the general scheme of this study. GENESIS was coupled with the MCRM for automatic exchange of input and output data files between the two models. The strategy behind the optimization scheme was based on creating the reflectance values using the MCRM model. A random number generator, which sets the values within user-defined minimum and maximum values, generated the initial values for land surface biophysical parameters (Table 3.1). For each pair of biophysical parameters, the MCRM model was run and the model output used in the genetic algorithm for optimization processing. A goodness-of-fit between the measured and simulated reflectances was calculated using Eq. (1.7), which served as the merit function.

3.3.1 Surface reflectance and LAI measurements

Atmospheric correction of the satellite images has been shown to significantly improve the accuracy of image classification and surface parameter estimation (Liang et al., 2001; Rahman, 2001). A new atmospheric correction algorithm has been described in Chapter 2 and was applied to carry out atmospheric correction for the four Landsat ETM+ images (May 11, 2000, Oct 2, 2000, Apr 28, 2001 and Aug 2, 2001). The field

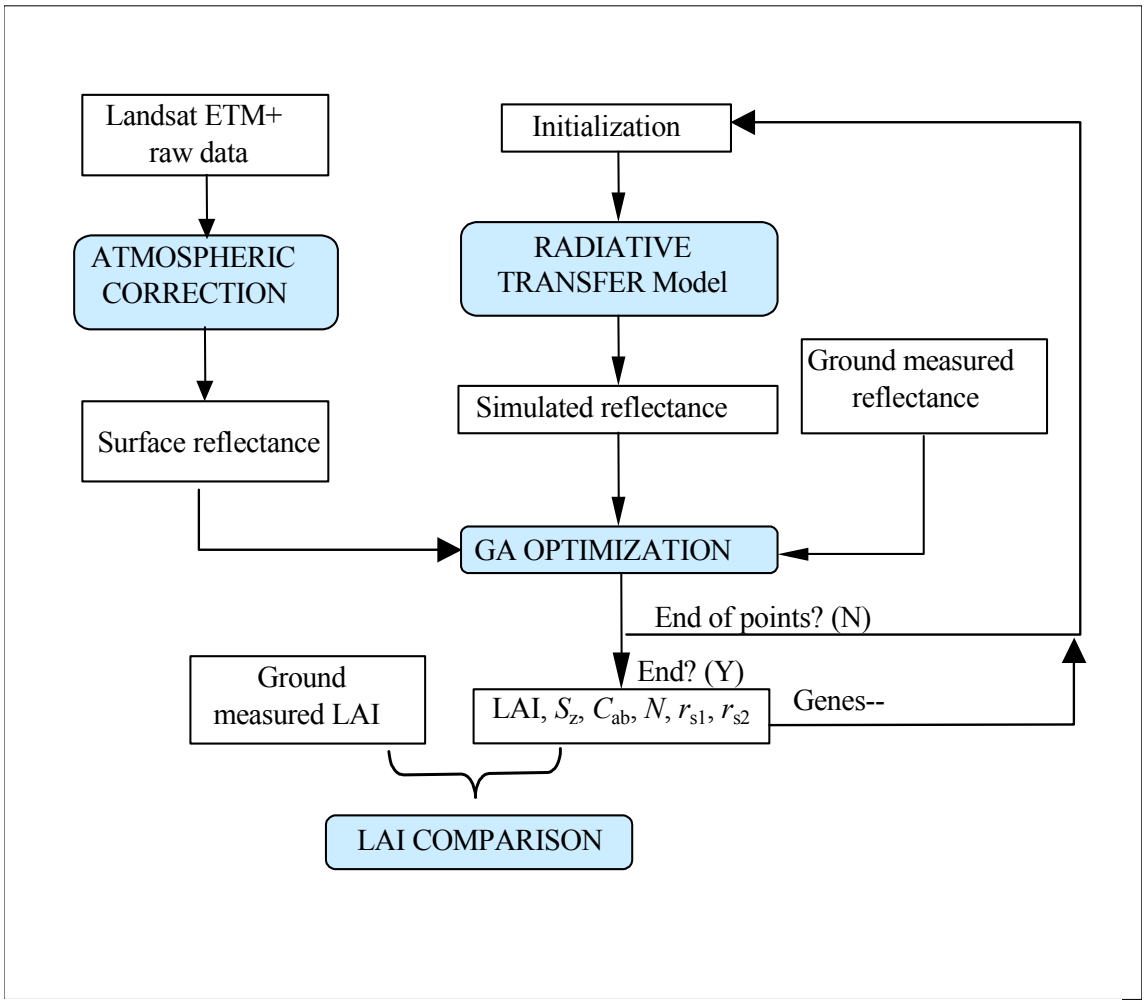

Figure 3-1 Flowchart of the approach to estimate LAI with a genetic algorithm optimization method.

validation results showed that the cluster-match method works very well for all the Landsat ETM+ data.

During each of the four Landsat overpasses, field measurements were carried out in the study area at BARC. Several field plots were selected, which are typical, homogeneous, and 200-300 meters on each side. The surface reflectance was measured with the Analytical Spectral Devices (ASD) (Analytical Spectral Devices (ASD), 2000). In each plot, about 50-100 points along several random transects were measured. The average reflectance of these points was used to represent the mean reflectance of that plot. The LAI of the plots was measured with an LAI-2000 Plant Canopy Analyzer (LAI-COR, 1991) around satellite overpass time. For each plot, about 5-20 or more random points were measured and the average of these was used to represent the mean LAI of that plot. Some typical land cover types were measured, such as alfalfa, wheat, corn, grasses, soybean, and forest (Table 3.2).

Field LAI measurement has some limitations. First, the Beer-Lambert Law is used to convert the gap-fraction data (the ratio for each ring's above- and below-canopy radiation value) measured by LAI-2000 to LAI values assuming that the foliage is black and only skylights are seen by the sensor beneath the canopy. Actually, no real canopy conforms exactly to this assumption. Second, field LAI measurement is usually affected by foliage clumping, stems and fruits. The LAI value could change as the season progresses through senescence and normal maturation of the canopy. Third, for the forest sites, the measured LAI is actually the apparent LAI because it includes trunks and

branches. LAI-2000 could overestimate the LAI of canopies containing numerous dead branches (Denison and Russotti, 1997).

Table 3.2 has also shown the range of coefficient of variance (CV, standard deviation divided by mean value) for each date. Of the 51 plots, only three plots have a CV larger than 0.40. Of all the nine different cover types (Table 3.2b), the maximum CV (0.38) was observed for the alfalfa plot on Aug 2, 2001. The CV values for all other cover types were less than 0.27. This shows that the field plots were generally homogeneous. LAI performance among different vegetation types is complicated by seanonal changes. In this study, more points for hairy vetch and other high LAI fields are still needed.

For the forest sites, a strategic random sampling method was applied. At each forest site, at least 2 plots were randomly picked. In each plot, five points were identified. They were the center point and then 15 meters north, east, south and west from the center. For more accurate measurements, take into account the influence of shoot structure, dead branches and stems (Chen, 1996b). In this study, the leafless LAI of trunks and branches of the same sites was measured on Mar 20, 2001 when the deciduous trees were leafless (mean leafless LAI=1.41). Thus, the green LAI (LAI_g, denoted as LAI in this dissertation) was calculated using the difference between summer and winter measurements.

Table 3.2 Field LAI measurements at BARC. (a) shows the mean, standard deviation (std) and coefficient of variation (CV), number of points, and cover type[a] of each plot. (b) shows the mean CV and the total number of plots (in brackets) of each cover type for the four dates.

(a)

Mean	Std	CV	Points	Type	Mean	Std	CV	Points	Type
May 11, 2000					Apr 28, 2001				
0.97	0.386	0.399	6	G	4.80	0.193	0.040	5	G
1.34	0.412	0.308	6	G	4.17	0.890	0.214	7	W
1.23	0.042	0.034	3	G	4.98	0.544	0.109	7	W
4.50	1.519	0.337	5	W	1.46	0.360	0.247	3	G
6.41	0.243	0.038	5	W	2.31	0.528	0.229	6	G
5.67	0.647	0.114	5	H	1.42	0.247	0.174	6	G
6.59	0.752	0.114	5	H	2.82	0.624	0.221	7	G
1.07	0.329	0.307	15	F	1.42	0.637	0.449	7	G
3.15	0.329	0.104	15	F	1.24	0.501	0.405	8	G
2.08	0.584	0.280	15	F	3.39	0.314	0.093	8	B
2.05	0.397	0.193	20	F	1.55	0.319	0.207	11	F
2.52	0.315	0.125	20	F	1.77	0.261	0.148	10	F
Oct 2, 2001					Aug 2, 2001				
5.11	0.326	0.064	27	S	2.18	0.483	0.222	12	O
3.57	1.352	0.379	22	S	2.44	0.492	0.202	12	C
2.72	0.417	0.153	6	C	1.77	0.504	0.284	12	C
3.20	0.686	0.214	11	C	1.11	0.421	0.378	9	A
2.62	0.590	0.225	18	C	1.38	0.527	0.381	10	C
2.79	0.569	0.204	5	C	2.47	0.567	0.230	5	C
4.47	0.826	0.185	18	G	0.63	0.172	0.271	6	C
5.53	0.730	0.132	18	G	3.20	0.551	0.172	7	G
5.36	0.865	0.161	17	A	2.04	0.272	0.134	15	F
1.61	0.456	0.283	15	F	2.07	0.277	0.134	10	F
2.76	0.327	0.118	14	F	2.90	0.586	0.202	10	F
1.75	0.671	0.383	15	F	3.83	0.283	0.074	15	F
1.80	0.807	0.448	30	F					
2.52	0.315	0.125	20	F					
3.31	0.299	0.090	21	F					

(b)

	A	B	C	F	G	H	O	S	W
May 11, 2000				0.202(5)	0.247(3)	0.114(2)			0.188(2)
Oct 2, 2000	0.161(1)		0.199(4)	0.241(6)	0.159(2)			0.222(2)	
Apr 28, 2001		0.093(1)		0.178(2)	0.252(7)				0.162(2)
Aug 2, 2001	0.378(1)		0.274(5)	0.136(4)	0.172(1)		0.222(1)		

[a]A: alfalfa; B: Barley; C: corn; F: deciduous forest; G: grass; H: hairy vetch; O: Orchard grass; S: soybean; W: wheat.

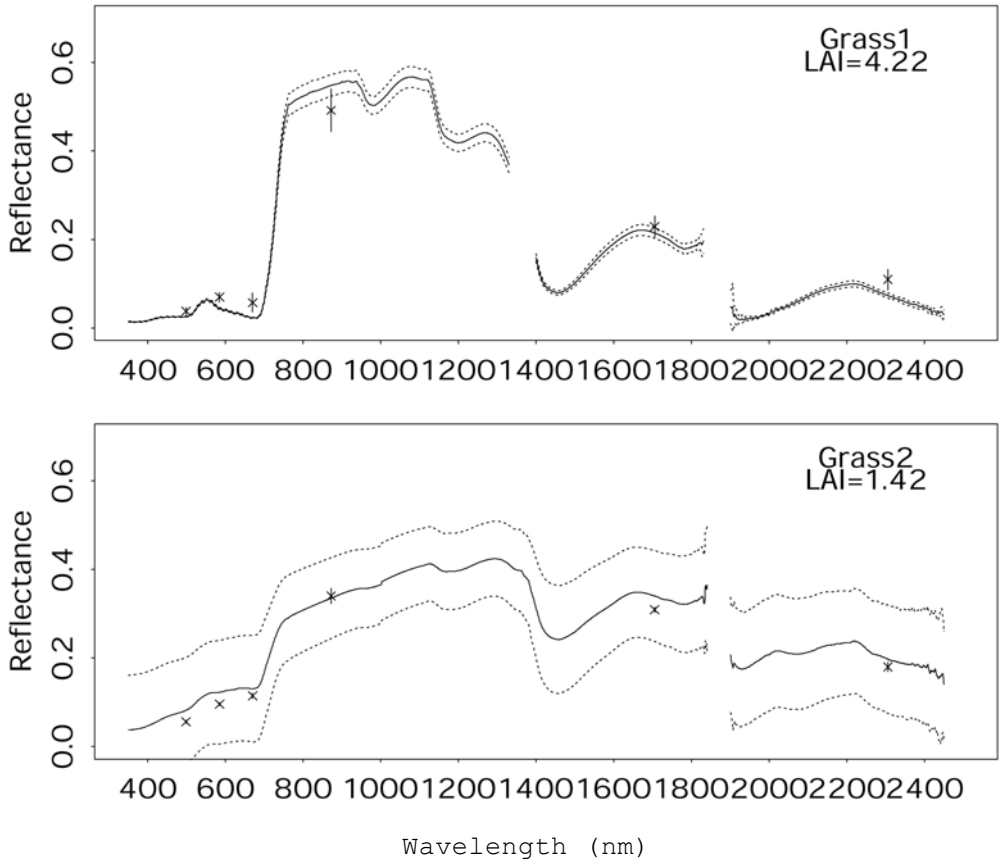

Figure 3-2 Two examples of simultaneous ASD-measured surface spectral reflectances (lines) and the atmospherically corrected reflectances from ETM+ (crosses). Vertical line segments denote the standard deviation of the ETM+ reflectances. Dashed lines are one standard deviation away from the mean reflectances (solid line).

Figure 3-2 illustrates two examples of the atmospherically corrected (using the new method described in Chapter 2) ETM + reflectance and the ASD-measured surface reflectance. These two have the lowest and highest CV among ASD measured reflectances. The solid lines are the mean reflectance, and the two dashed lines correspond to mean reflectance ± one standard deviation. Grass1 was denser (LAI=4.22) and its radiometric information was very stable. It was one of the most homogeneous fields where the ASD measurements were taken with a CV of 0.0748. In contrast, grass2 was sparser (LAI=1.42) and had a comparatively high CV (0.5978).

The ETM+ pixels were extracted from the homogeneous test sites manually. Normally, 5 to 15 pixels were used based on different field sizes. The one standard deviation range of the corresponding ETM+ pixels are also shown in Figure 3-2 with vertical line segments. The CVs of the ETM+ reflectance for these two grass fields are 0.1952 (grass1) and 0.0493 (grass2) respectively. From Figure 3-2, we can see that the retrieved ETM+ reflectances in all six bands match well with the ASD measurements. In building equation (1.7), the mean values of the ASD measurements were used, keeping in mind that some points may have higher deviation than others. Of course, the number of bands (B in 1.7) will be less than 420 if noise gaps exist.

3.3.2 Experiments with different reflectance data sets

For clarification, the LAI values derived by the GA method are denoted by LAI-GA. The experiments were conducted for three scenarios with different n and B values in equation (1.7).

- Invert LAI from Landsat ETM+ bands (n=51, B=1~6)

  Among the field measurements, 51 mean LAI values were obtained from different large homogeneous sites (Table 3.2). For these 51 plots, canopy reflectances were derived from atmospheric correction of ETM+ six reflective bands. The model calculated spectral reflectance (5 nm) was integrated into six ETM+ bands using their sensor spectral response functions. LAI values were retrieved using all six ETM+ bands (B=6), NIR band, red band, and both red and NIR bands (B=1~2). Previous inversion of the MCRM (Kuusk, 1995b) using NIR band reflectance showed much better results than using the red band reflectance. The best results were obtained when both red and NIR bands were used (Kuusk, 1995b).

- Invert LAI from field measured ASD reflectance (n=14, B=420)

  There were 14 homogeneous plots where LAI and field reflectance data were measured simultaneously. The field measured ASD reflectance ranges from 350-2500nm with the spectral resolution of 1 nm. Because the model outputs reflectance at the spectral resolution of 5 nm, the ASD reflectance data were aggregated to 5nm to match the MCRM results. Thus, B=420 in this case.

- Invert LAI from Landsat ETM+ (n=900, B=6)

  The GA method was applied to retrieve LAI from a 30×30 pixel area of an ETM+ image (n=900). LAI-GA was compared with the results derived by the Powell inversion method in MCRM.

3.3.3 Strategies to fix free parameters and select ETM+ bands

In practice, the number of genes is very crucial in inversion. Some studies have found that the inversion is more robust if the number of free parameters is small (Kimes et al., 2000). For accurate inversions, the number of free parameters that significantly impact the canopy reflectance ought to be minimal (Kimes et al., 2000). Some parameters that change less rapidly need to be fixed (Kimes et al., 2000). In this study, starting from 6 free parameters, three parameters (S_z =0.8, C_{ab} =50 and N=1.8) were then fixed one after another. The fixed values represent the general conditions of the study area in the inversion experiments.

The experiment starts by using all six genes and six ETM+ bands. Figure 3-3 shows the preliminary GA optimization results for S_z, C_{ab} and N. The distribution of the corresponding merit function (1.7) is also illustrated in the last row. It is noticed that the value of ε^2 tends to decrease with increasing LAI, which means it is easier to reach global optima at higher LAI. This may be because of the more reliable reflectances from ETM+ and RT simulation for higher LAI. This figure does not include LAI and the two soil parameters as they will be discussed in section 3.4.

The first row of Figure 3-3 displays the distribution of the retrieved S_z and LAI values. Their statistical values (mean, standard deviation and CV) were also calculated. From Figure 3-3 and its statistics, it is easy to determine that the S_z is the least variable

parameter in the test site. With NIR only, a stable S_z value (0.8) can be achieved with the lowest CV (0.1286). Other parameters, such as C_{ab} and N change more rapidly over the area. In this case, S_z =0.8 was chosen to represent the general status of the study area and it was fixed in later inversions. It is inevitable to introduce some uncertainties during this kind of simplification. Further validation of the S_z value would require instantaneous field measurements. After S_z was fixed, the similar GA optimization procedure was conducted to fix the subsequent C_{ab} (50) and N (1.8); and thus, the number of genes was reduced from 6 to 5, 4 and 3.

It is reasonable that when the number of free parameters is decreased, the retrieved C_{ab} and N values may differ from what they were in the previous inversion. Because the field LAI is available, the retrieved LAI performance was observed as a subsidiary criterion, besides ε^2, to determine the optimal fixing values for S_z, C_{ab} and N. During these optimization processes, some of the necessary GA characteristics were kept the same, such as population size (50), crossover rate (0.6), mutation rate (0.001), and total trials (1000).

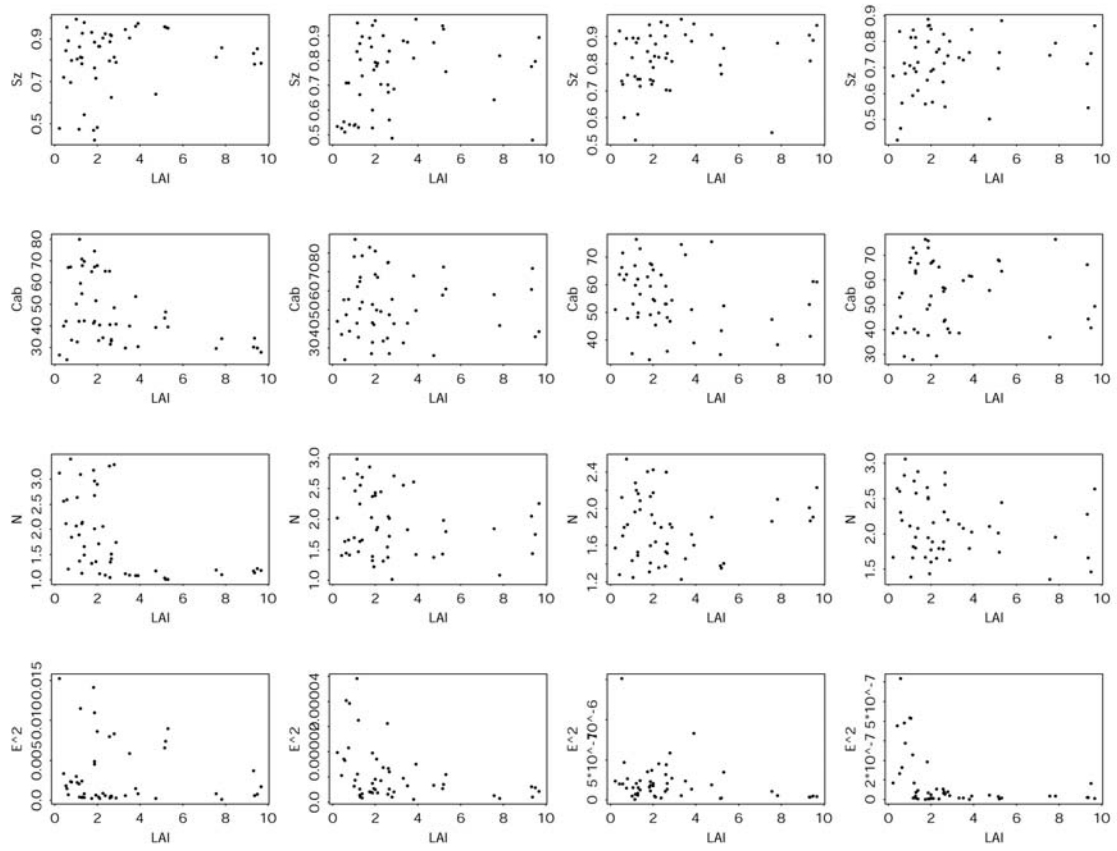

Figure 3-3 The distribution of S_z, C_{ab}, N and ε^2(E^2) (rows) as derived with the GA optimization method. The four columns are using: all six ETM+ bands, RED+NIR, NIR only, and red only, respectively.

3.4 Results and analysis

3.4.1 Using the retrieved ETM+ reflectance

The estimated LAI values derived from Landsat ETM+ reflectances were compared with field measurements. The results of the LAI-GA using all free parameters are displayed in Figure 3-4. The effects of fixing S_z, C_{ab} and N and using five, four and three genes were examined and they are presented in Figure 3-5 through Figure 3-7, respectively. Figure 3-4 through Figure 3-7 show the standard deviation of the retrieved LAI-GA. The standard deviation of the field LAI values is shown only in Figure 3-4. The variations of the field measured LAI values for other cases (G5, G4 and G3) are not shown in the figures because the results would be similar and redundant. At each plot, at least 5 samples were measured and their average value was used to represent the field LAI value. The R-square and the root mean-square error (RMSE) between the LAI-GA and field LAI are also displayed. The LAI-GA for different vegetation types are illustrated with different symbols in subplots (e)~(h) of each figure.

From these figures, we can see that LAI can be well retrieved using all six Landsat ETM+ bands (R^2>0.73 and RMSE<1.47). The best results (R^2=0.776, RMSE=1.064) were obtained from both red and NIR bands using 3 genes (Figure 3-7b). The result shown in Figure 3-7b was used later to test the algorithm for a slightly larger ETM+ area (Figure 3-10). LAI-GA likely overestimates when field LAI > 4 using all six bands

(Figure 3-4a, Figure 3-5a, and Figure 3-6a), but that is not the case if only NIR band is used. Inversion of this model using both red and NIR band reflectance has provided a very good estimation of LAI (R^2>0.71, and RMSE<1.06). In G3, using all six bands performs more poorly than using red and NIR bands only. The inversion looks fine using the NIR band only, but very bad when using the red band alone. With red band only, LAI-GA is likely to overestimate field LAI. No matter the number of genes used, use of the NIR band always provides much better results than the red band. Kuusk (1995b) also reported this. In other research: Privette et al. (1996) also used NOAA AVHRR NIR band only to invert LAI as the NIR band is more sensitive to canopy structural parameters.

In Figure 3-4e, LAI-GA match well with the field measured data except for a couple of hairy vetch points. In addition to the hairy vetch, higher deviation was also observed for a grass and soybean point whose measured LAI are larger than 4.0. For both six bands and NIR only, LAI-GA overestimate higher field LAI points for G6, G5 and G4. Since only one fifth of field LAI are larger than 4.0, more higher LAI plots are needed in this study for a better examination of the GA performance over different vegetation types.

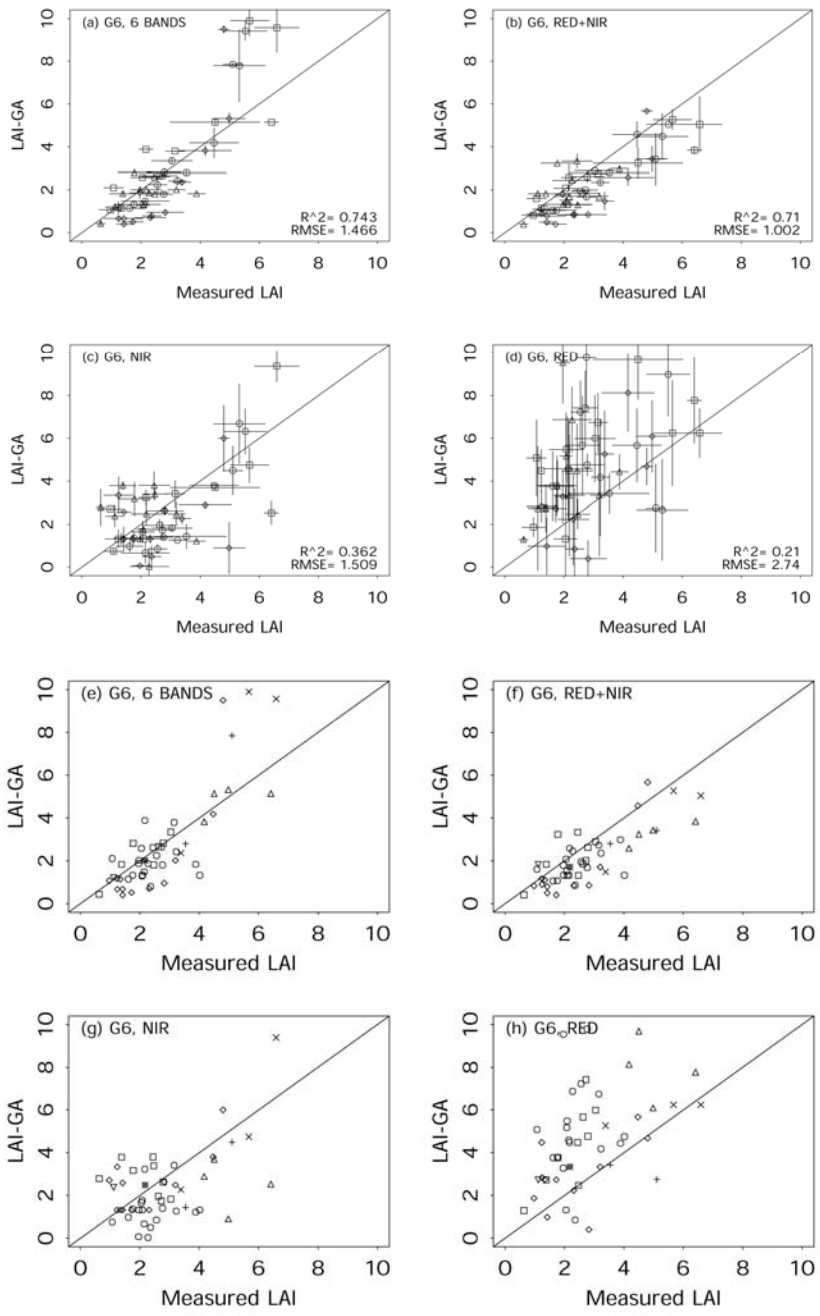

Figure 3-4 Comparison of LAI-GA with field LAI. LAI-GA is estimated from Landsat ETM+ images using: a) all six bands; b) red and near infrared band only; c) NIR band only; and d) red band only. Symbols for a)~d): May 11 (□) and Oct 2 (○) 2000 and Apr 28 (◇) and Aug 2 (△) 2001. The one standard deviation of field LAI and LAI-GA are shown with line segments. R^2: R square. 6 genes (LAI, S_z, C_{ab}, N, r_{s1} and r_{s2}) were used. (e)~h) compare LAI of different cover types, alfalfa (∇), barley, hairy vetch and orchard grass (×), corn (□), deciduous forest (○), grass (◇), soybean (+), and wheat (△).

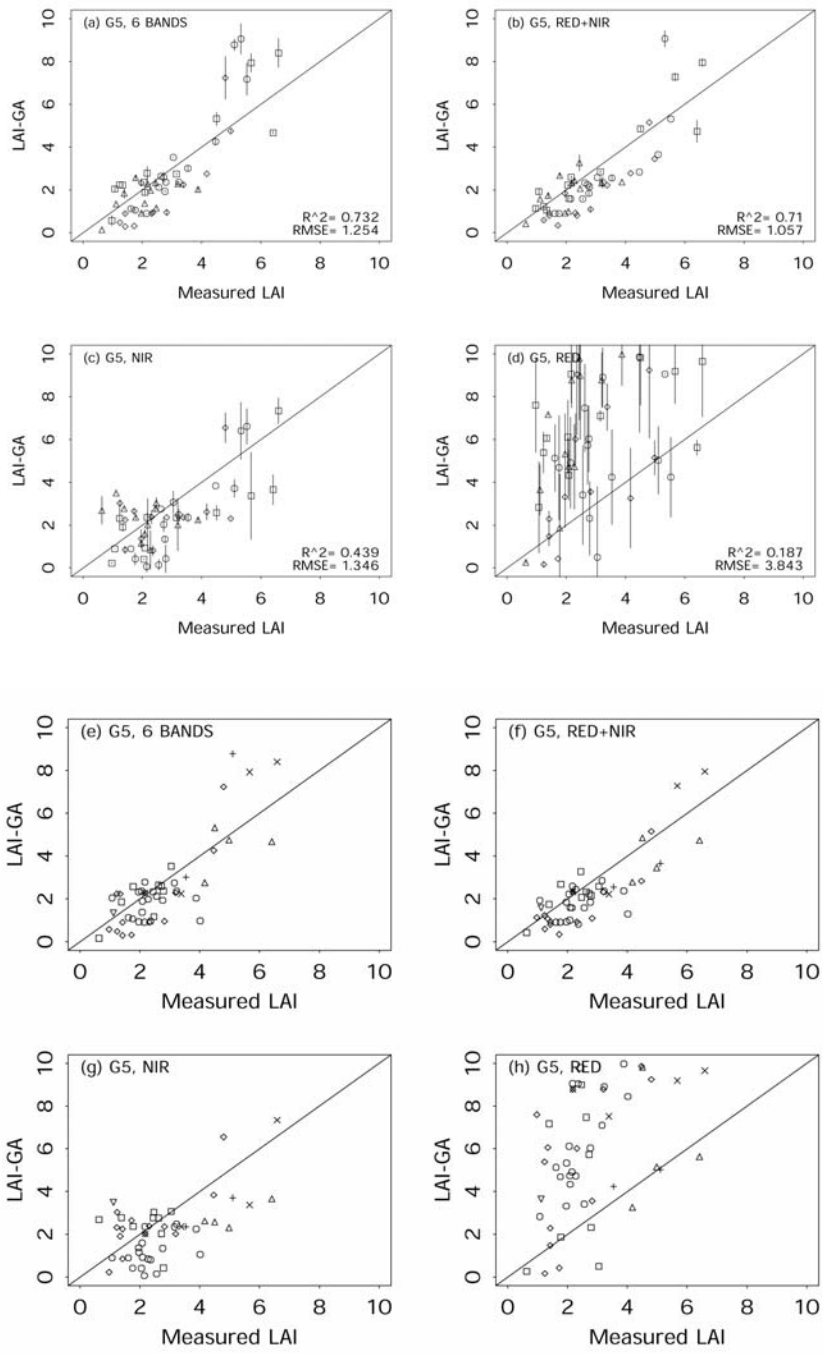

Figure 3-5 Comparison of field LAI with LAI-GA derived from Landsat ETM+ with five genes (LAI, C_{ab}, N, r_{s1} and r_{s2}) fixing S_z=0.8. (a)~(d) compare LAI of different dates. One standard deviation of LAI-GA is shown. (e)~(h) compare LAI of different cover types. Symbols: refer to Figure 3-4.

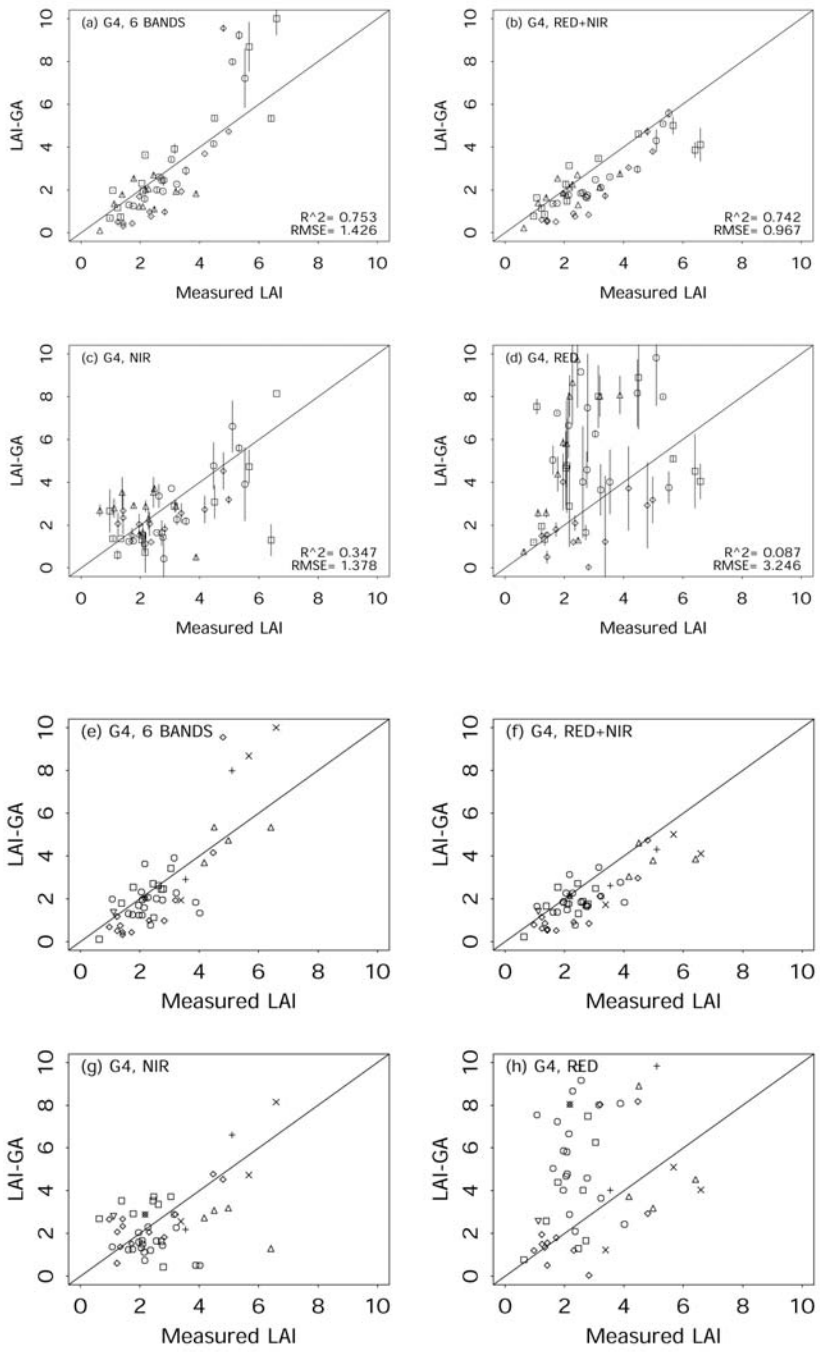

Figure 3-6 Comparison of field LAI with LAI-GA derived from Landsat ETM+ with four genes (LAI, N, r_{s1} and r_{s2}) fixing S_z=0.8 and C_{ab}=50. (a)~(d) compare LAI of different dates. One standard deviation of LAI-GA is shown. (e)~(h) compare LAI of different cover types. Refer to Figure 3-4 for symbols.

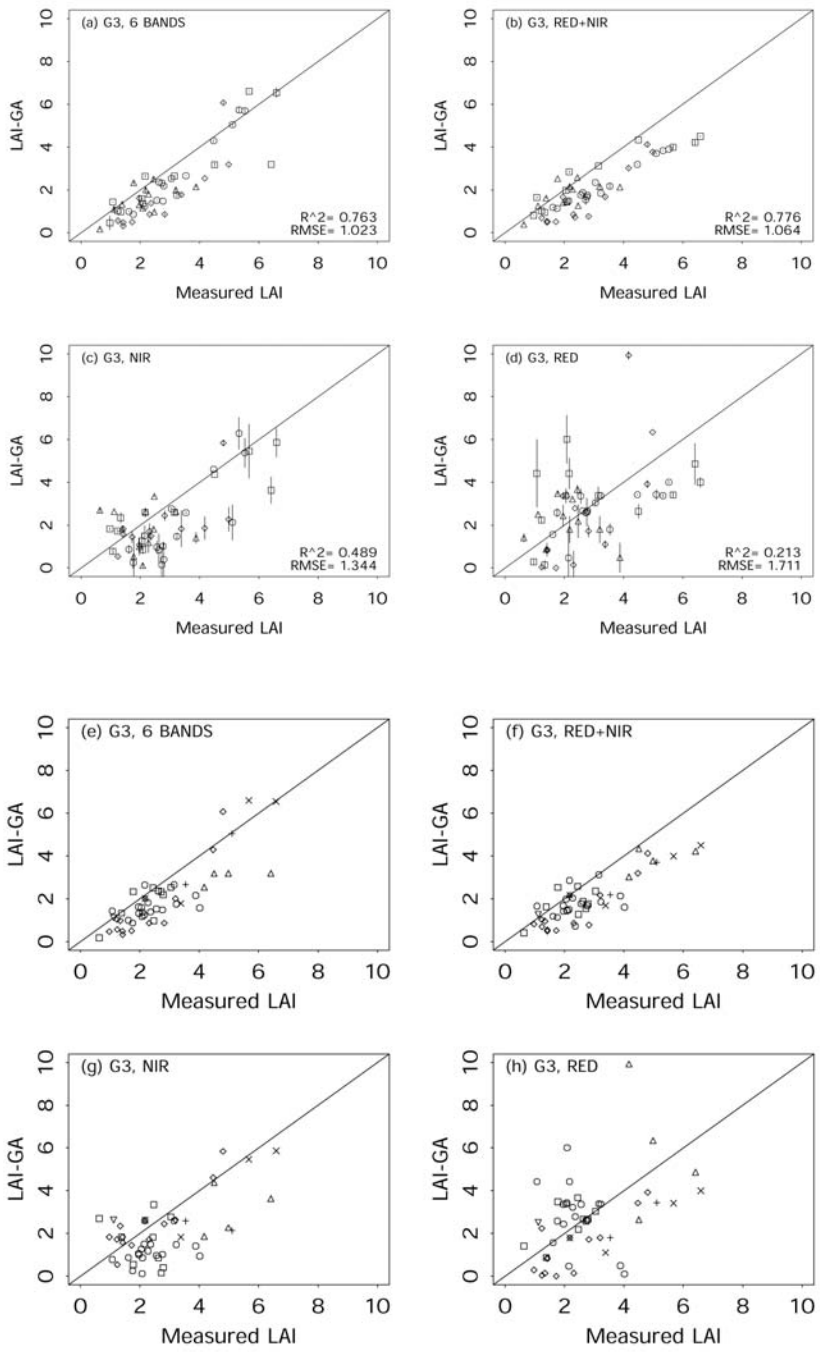

Figure 3-7 Comparison of field LAI with LAI-GA derived from Landsat ETM+ with three genes (LAI, r_{s1} and r_{s2}) fixing S_z =0.8, C_{ab} =50 and N=1.8. (a)~(d) compare LAI of different dates. One standard deviation of LAI-GA is shown. (e)~(h) compare LAI of different cover types. Refer to Figure 3-4 for symbols.

It is instructive to examine these figures more closely. One advantage of GA is that it reaches the global minimum of the merit function while providing the local minimum values simultaneously. A typical GA output looks like Table 3.3 for one point. Column ε^2 provides a number of (10 in this study) local minimum values, while the italicized row stands for the global minimum ε^2. Each LAI-GA point in the figures is denoted as the value at the local minimum of the merit function. As seen in Figure 3-4 to Figure 3-7 and Table 3.4, LAI-GA values have much larger variations at higher LAI (≥3). The only exception is at G3 with red band only when LAI-GA varies larger at lower values (<3). LAI-GA varies the highest when only the red band is used, then followed by the NIR band, red and NIR, and all six bands, which indicates the general trend of the solutions. For example, in G6, the standard deviations for all LAI-GA points are 1.624, 0.553, 0.237 and 0.169 for red, NIR, both red and NIR, and six bands.

Table 3.3 An example of a genetic algorithm output (six genes).

LAI-GA	S_z	C_{ab}	N	r_{s1}	r_{s2}	ε^2	Generations	No. trials
2.53	0.95	65	3.41	0.06	-0.02	8.16E-03	26	791
2.53	0.43	67	3.19	0.02	-0.08	7.81E-03	30	900
2.53	0.96	68	3.41	0.06	-0.02	8.22E-03	27	826
2.61	*0.44*	*68*	*2.58*	*0.02*	*-0.08*	*7.69E-03*	*24*	*750*
2.58	0.95	67	3.48	0.03	-0.02	8.09E-03	31	929
2.59	0.94	65	3.5	0.02	-0.08	7.90E-03	22	686
2.58	0.95	69	3.5	0.02	-0.08	7.94E-03	21	658
2.61	0.44	68	2.58	0.02	-0.08	7.70E-03	32	963
2.59	0.96	48	3.5	0.02	-0.08	8.28E-03	23	722
2.58	0.95	69	3.48	0.02	-0.08	7.97E-03	17	542

Table 3.4 The mean standard deviation of the LAI-GA and field LAI for different number of genes (6, 5, 4 and 3) and band combinations.

Gene number	Band combination	LAI-GA<3	LAI-GA≥3	All LAI-GAs
G6	6 Bands	0.088	0.347	0.169
	RED+NIR	0.117	0.574	0.237
	NIR	0.32	0.938	0.553
	RED	1.175	1.827	1.624
G5	6 Bands	0.074	0.385	0.161
	RED+NIR	0.056	0.174	0.085
	NIR	0.258	0.554	0.34
	RED	1.049	1.561	1.469
G4	6 Bands	0.065	0.468	0.197
	RED+NIR	0.05	0.275	0.109
	NIR	0.358	0.836	0.507
	RED	0.552	1.277	1.015
G3	6 Bands	0.058	0.084	0.065
	RED+NIR	0.034	0.06	0.041
	NIR	0.299	0.379	0.318
	RED	0.397	0.291	0.352
Field LAI: 0.427 (LAI<3), 0.568 (LAI≥3) and 0.487 (all LAI)				

If all six bands or both red and NIR bands are used, the variation of LAI-GA appears smaller than the field measured LAI values. Biases between LAI-GA and measured LAI may occur because of: 1) the heterogeneity of the ground types as they were assumed homogeneous in LAI measurement; 2) the scale differences between the field LAI (averaged point measurement) and the LAI-GA derived from ETM+ pixel (30 m); and 3) inaccuracies in the optimization algorithm or the canopy RT model and other factors.

Fixing S_z, C_{ab}, and N does improve the results. For example, the R-square value increases from 0.743 to 0.763 when the number of genes decreases from 6 to 3 when using all six bands. Greater improvement could be seen when using both red and NIR bands (from 0.71 to 0.776). Decreasing the number of free parameters increases stability of retrieving LAI values, especially for higher LAI values (Figure 3-4 to Figure 3-7 and Table 3.4). For example, the standard deviation of 43.1% LAI-GA is greater than 0.1 for G6 when the red band or NIR band was used (Figure 3-4b), but only 7.8% for G3 when both the red and NIR bands were used (Figure 3-7b). The lowest deviations were observed for G3, 0.065, 0.041, 0.318 and 0.352 when using six bands, both red and NIR bands, NIR band and red band. In addition, decreasing the number of genes will significantly improve computational efficiency.

Figure 3-8 represents the LAI values for different ground types. The LAI values were derived from the results of Figure 3-5b. In the BARC area, LAI values vary between 1.54 (grass) and 4.25 (hairy vetch). The mean LAI for deciduous forest is 1.74. These results are valuable for looking into the LAI of different land cover types.

3.4.2 Using field measured reflectance data

To further test the proposed approach using hyperspectral data, the seasonal ground-based radiometric measurements were used to estimate LAI using equation (1.7) and compared with simultaneous in-situ LAI measurements. At these sites, fourteen pairs of ground radiometric and LAI measurements were available to form direct comparisons. The proposed approach appears to have produced good estimates of LAI within this region. The estimated LAI-GA agrees well with the in-situ measurements (Figure 3-9, R^2 = 0.611, 0.65, 0.563, and 0.66; RMSE=2.621, 2.464, 2.895 and 1.181), but did not meet the expectation that ground-measured reflectance data would provide the best results, since they were supposed to be the "true" reflectance. The R-square value was lower than the results from B=2 (Figure 3-7b). This could be partly because of the way that the reflectances were measured. In the field, the ASD sensor was pointed at the canopy within less than 2 meters above the canopy. In this case, only part of the canopy was located within the ASD field of view (FOV); therefore, the spectral measurement may not have represented the whole canopy for some crops. Noise may also be caused in the water absorption bands within the total 420 bands. There was no general trend how the gene number affects the inversion accuracy for these points. The R-square values for G5 and G3 were very close (0.65 and 0.66); however, the lowest RMSE (1.181) was obtained for 3 genes. Figure 3-9e~h show that LAI-GA overestimates field LAI for hairy vetch and some high LAI points for G6, G5 and G4. This agrees with its performance with the ETM+ bands (Figure 3-4~Figure 3-7).

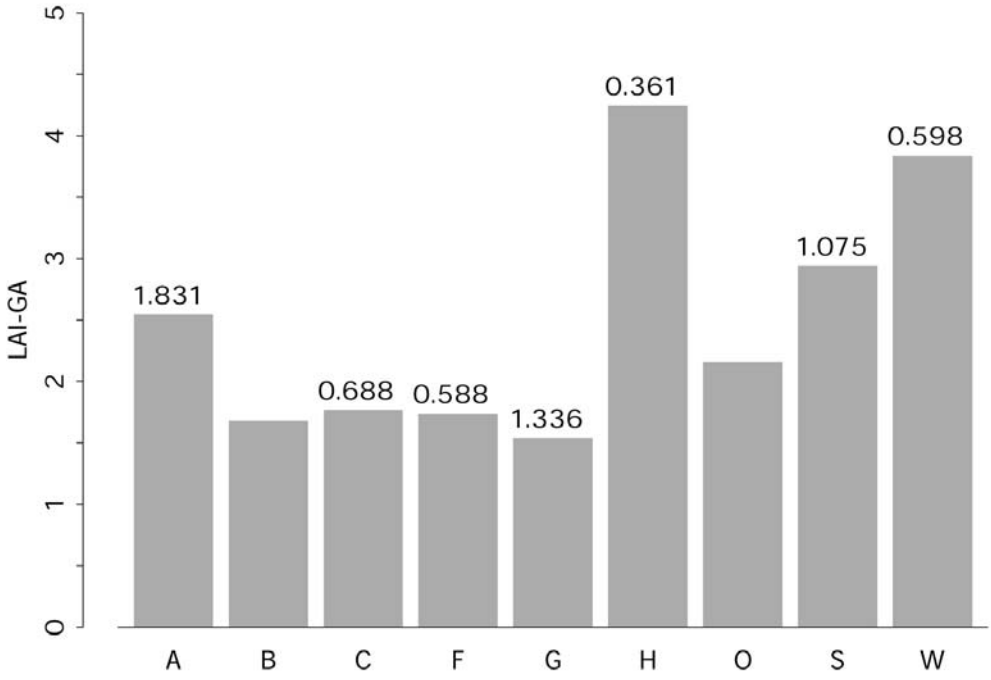

Figure 3-8 Retrieved LAI-GA values for different ground types (A: alfalfa; B: barley; C: corn; F: deciduous forest; G: grass; H: hairy vetch; O: orchard grass; S: soybean; W: wheat). The numbers above the bars are one standard deviation.

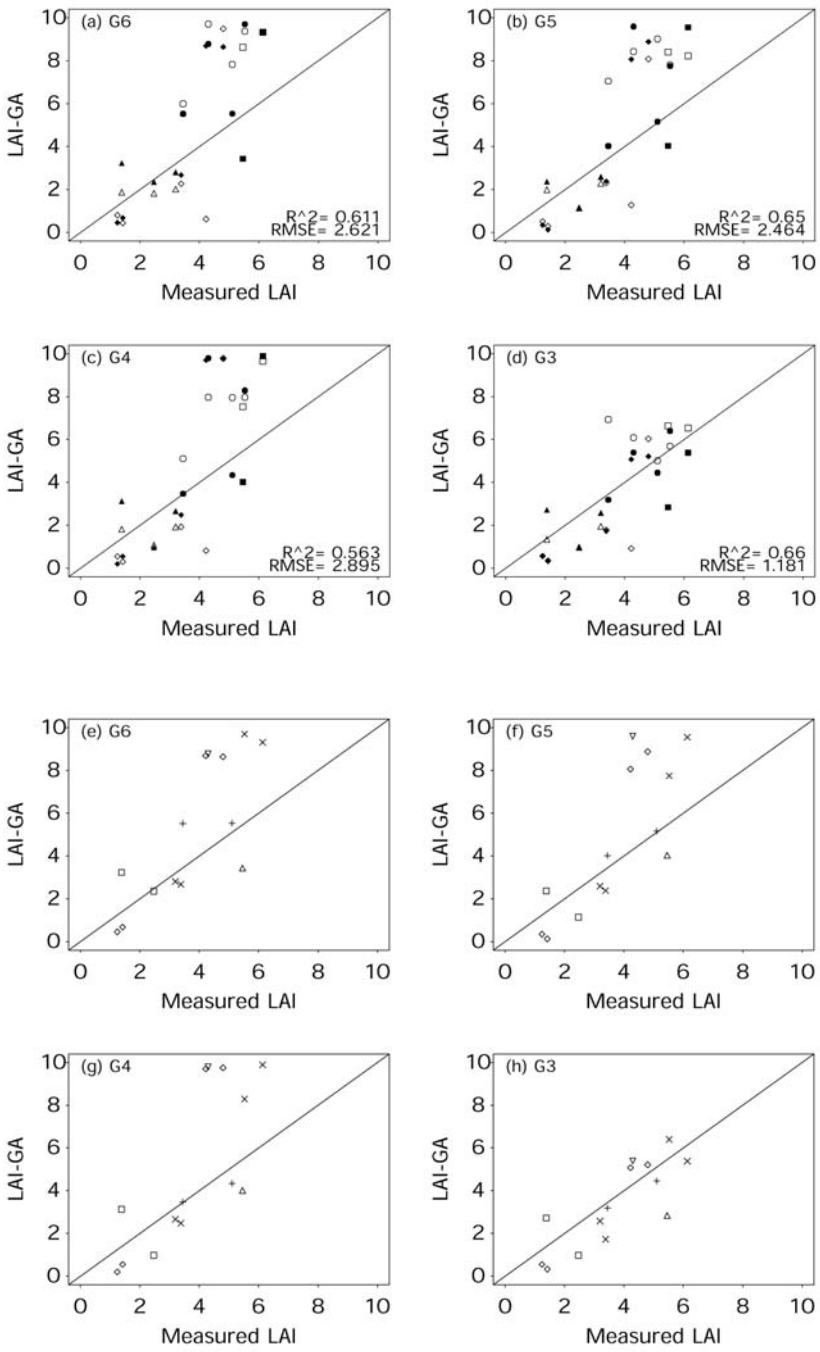

Figure 3-9 Comparison of LAI-GA (solid points) with field measured LAI. LAI-GA was derived from field ASD-measured reflectance data collected at BARC, USDA. The LAI derived from ETM+ 6 bands (hollow points) are also shown. (a)~(d) compare LAI of different dates. (e)~(h) compare LAI of different cover types. Refer to Figure 3-4 for symbols.

The common points for both ETM+ and ground reflectance measurements were found. The LAI values derived from ETM+ (6 bands) are shown as hollow symbols in Figure 3-9. Generally speaking, the 6 ETM+ bands have very similar results to the hyperspectral ASD measurements. This suggests that many of the ASD bands are redundant for LAI retrieval. From their R-square and RMSE value, ASD works a little better than ETM+ for G6, G5 and G3. The only exception is in G4 when ETM+ produces a higher correlation and lower RMSE with field LAI. Because of the limited number of points, more ground-based reflectance and LAI measurements are needed for more conclusive results. This approach is useful for other similar hyperspectral remotely sensed data, such as the EO1 Hyperion data.

3.4.3 Comparison with other methods

It is interesting to compare the GA optimization with other methods mentioned in the introduction section. For example, the LUT method does not have the initial guess selection problem and the solution is searched over the whole space of canopy realization. Nonetheless, as pointed out in the introduction, the LUT method treats the continuous numerical optimization problems as discrete. In this way, the accuracy of the database that the LUT needs is based on the coding accuracy of the input parameters.

In this chapter, the GA-based inversion method was compared with the Powell algorithm in IMCR (Inversion of the Markov Canopy Reflectance model) provided by Kuusk (2001). The Powell algorithm is often used when there are a large number of free

parameters. It is noted that the GA method does not require the initial guess of the parameters while the Powell method does. The initial values are determined based on a priori field knowledge. For comparison, an example of the VI approach was also presented at the end of this section.

The LAI maps (30×30 pixels) for Apr 28 and Aug 2, 2001 (Figure 3-10) were generated with both GA and Powell optimization methods. The LAI-GA and LAI-Powell maps were made with the same conditions as Figure 3-7b. The spatial patterns of the two methods were very similar, although the absolute LAI values may differ. The brown points were either bare lands or roads, the gray/white areas being houses; yellow and green pixels were either crops or forests. The estimated LAI-GA values ranged from 0.12 to 6.02 on Apr 28 and from 0.26 to 3.85 on Aug 2. However, most LAI on Apr 28 (Figure 3-10) is below 4.0. There are only 6 dense grass pixels whose LAI-GA is greater than 4.0.

To further examine the similarity and differences between the two approaches, the LAI data are compared in Figure 3-11. Statistical analysis indicated that there was no significant difference between the LAI maps generated with the GA optimization

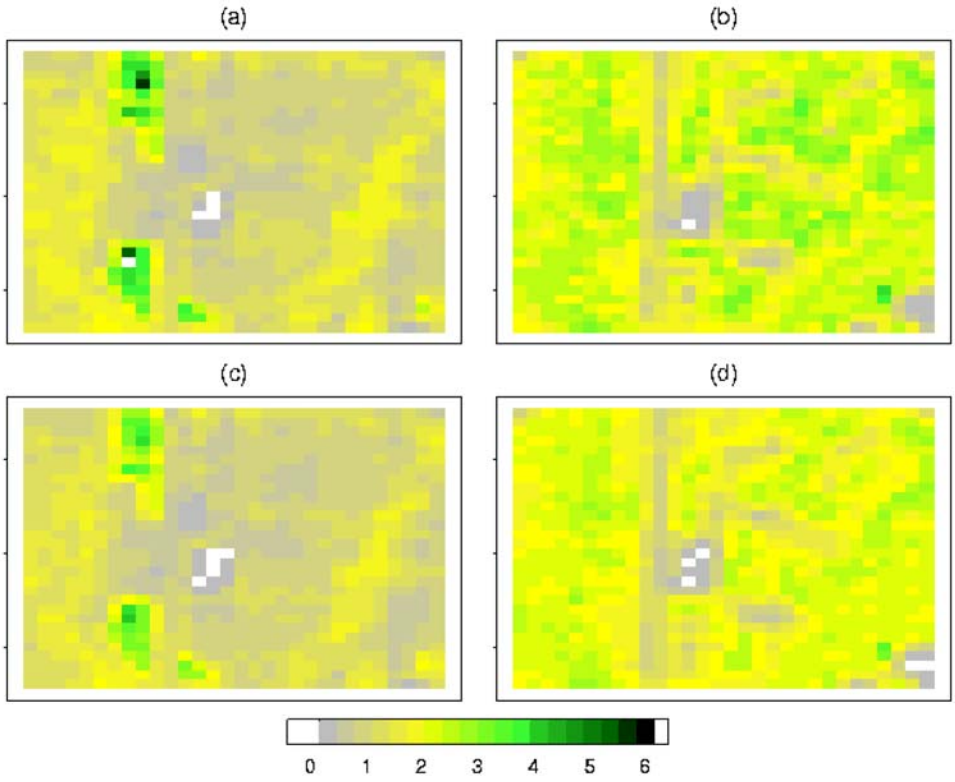

Figure 3-10 Comparison of LAI maps generated for (a) Apr 28 and (b) Aug 2, 2001 using GA method; (c) Apr 28 and (d) Aug 2, 2001 using the Powell inversion algorithm.

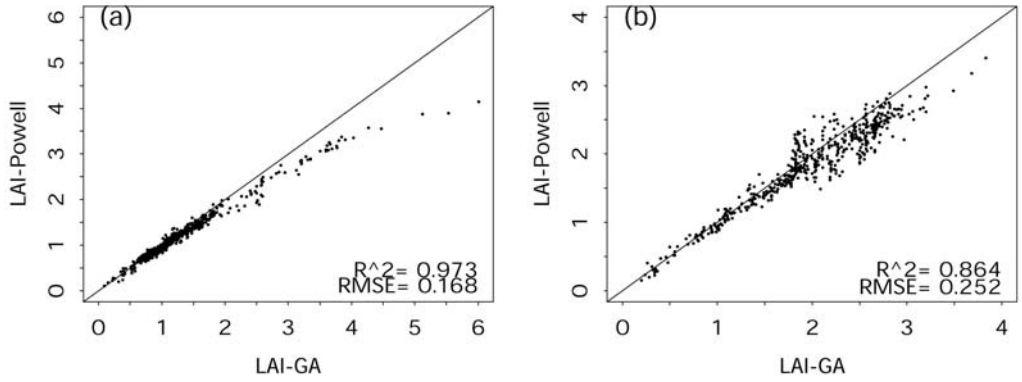

Figure 3-11 Comparison of LAI retrieved with GA optimization method (LAI-GA) and with the Powell inversion algorithm (LAI-Powell) for (a) Apr 28 and (b) Aug 2, 2001.

method and the Powell method. LAI-GA tends to be greater than LAI-Powell, especially when LAI>3. The results of Apr 28 (R^2=0.973) agree better with LAI-Powell than that of the Aug 2, 2001 (R^2=0.864). This may be because of the low LAI on Apr 28 where 92.1% pixels are less than 2.0 (mean LAI=1.33). On Aug 28, LAI increases (mean LAI=2.17) and only 35.8% are less than 2.0.

As mentioned in the Chapter 1, many relationships have been established between VIs and LAI (Baret and Guyot, 1991). The most commonly used vegetation indices are RVI and NDVI. In this study, it is difficult to use the LAI-VI method as it involves nine ground cover types on different dates (Table 3.2). Figure 3-12 shows the LAI-NDVI scatterplot with several fitted curves. NDVI approaches a saturation level for LAI>4. Generally, both the polynomial and power function fit the LAI-NDVI poorly. This also necessitates the effort to look into the GA for retrieving LAI.

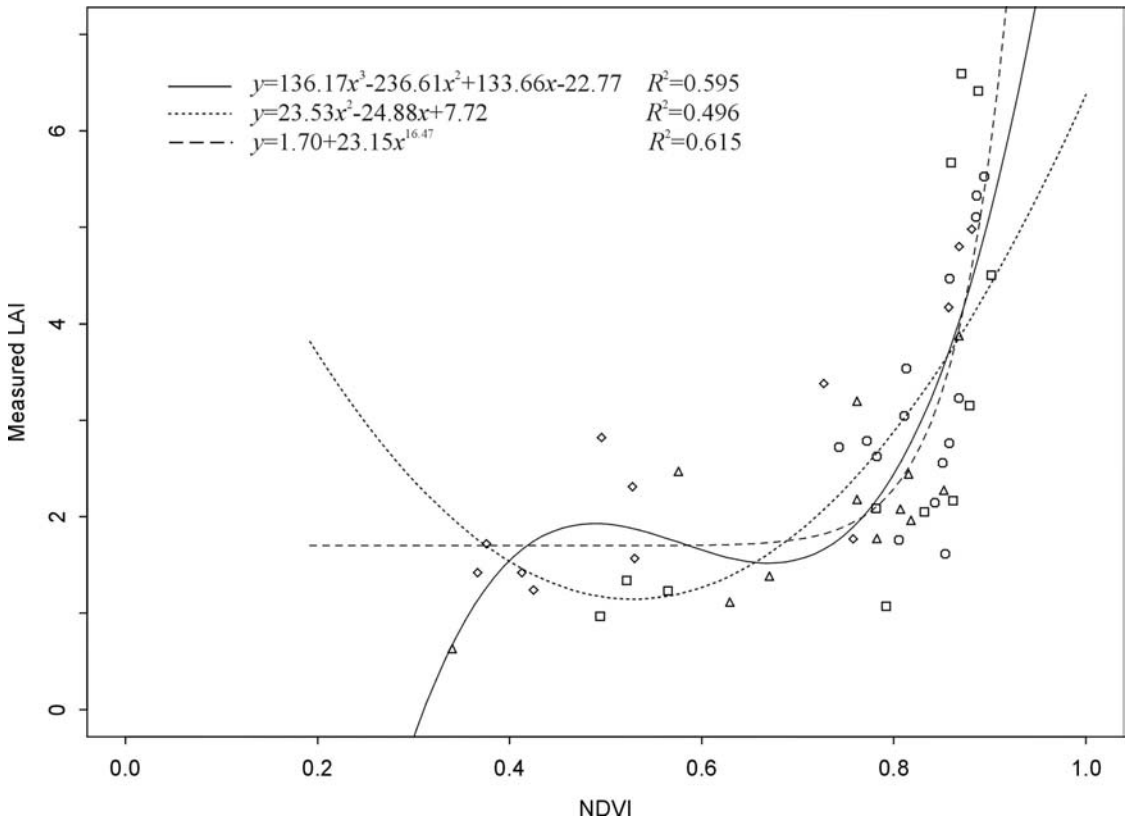

Figure 3-12 LAI-NDVI relationships. Polynomial and power functions are used to correlate NDVI and LAI.

3.5 Summary

In this work, the GA optimization methods have been explored for retrieving LAI from Landsat-7 ETM+ images and the field measured reflectance. The Markov chain model of canopy reflectance (Kuusk, 2001) was used to simulate surface reflectance. Both reflectance data derived from ETM+ image after atmospheric correction and from field measurement were used to construct the merit function.

Six free parameters, LAI, S_z, C_{ab}, N, r_{s1}, and r_{s2} (see Table 3.1), were considered in the retrieval. Different ETM+ band combinations were tested, i.e., with all six bands, both NIR and red bands, NIR band, and red band. The retrieved LAI was in agreement with the measured LAI. Overall, the best results were obtained with three genes (LAI, r_{s1}, and r_{s2}) from ETM+ red and NIR bands (R^2=0.776, RMSE=1.064). Generally speaking, the results meet the Global Climate Observation System (GCOS) and the Global Terrestrial Observation System (GTOS) requirements, which need an accuracy of ±0.2~1.0 for terrestrial climate modeling (CEOS/WMO, Dec, 2001). The results were also reasonable when only the NIR band was used, but appeared unacceptable when just the red band was used.

Starting from six, the number of free parameters was reduced by fixing the least dispersed ones. Four cases were tested, with six, five, four and three genes by fixing S_z, C_{ab} and N successively. In this study, reducing the number of genes does change the inversion accuracy. It can be seen from Figure 3-4 to Figure 3-7 that the LAI-GA's

accuracy changes with the number of genes. As expected, LAI values have large variations over the study area. The retrieved LAI-GA values tend to be more stable with fewer genes, demonstrated by the decreasing standard deviation. Considering the computational efficiency, three genes and both red and NIR bands were used to map the LAI in the study area. The results using the Powell minimization algorithm were compared with the LAI-GA. The difference between LAI-GA and LAI-Powell is very small for lower LAI (<3), and increases when LAI>3.

The GA optimization method provides an alternative to invert the RT models in remote sensing. The advantage of GA is two-fold: first, it scans all the initial conditions and provides several possible solutions for detailed examination of the global optimum solution, thus it avoids the inaccuracies introduced by conventional minimization algorithms; second, it only runs the forward RT model with constrained parameter space and is straightforward in the optimization process. Experiments are needed to test this method in more complicated areas. For similar research, it is suggested that the minimum number of genes using both the red and NIR bands be utilized.

Chapter 4 LAI Retrieval from ETM+ with a Hybrid Approach

4.1 Introduction

The application of the genetic algorithm in the optimization process of the RT model inversion was described in the previous chapter. Existing RT model inversion with an iterative process is both time consuming and difficult to use on regional and global scales (Kimes et al., 2000). Nonparametric methods (see 1.2.3) can speed up the inversion process significantly, but they are still dependent upon the accuracy of biophysically-based RT models. In addition, although they are easy to use, they have not been generalized to handle arbitrary directional and spectral combinations (Kimes et al., 2002). My objective is developing an improved hybrid approach which integrates the advantages of RT methods and nonparametric methods while avoiding their limitations. Both the artificial neural network (NN) approach and the projection pursuit regression (PPR) approach were tested in this hybrid approach. This chapter discusses the integration of RT and NN methods and their application in ETM+. The extension of this method to MODIS and the integration of RT and PPR will be introduced in the next chapter.

The process of an NN inversion may be outlined as follows: 1) given a set of empirical environmental, leaf, canopy and soil parameters, determine the set of canopy reflectances with a forward RT model; 2) initiate the NN training (or learning) process with part of the look-up table obtained in the first step, and find the relationship between the input data and the output reflectances; 3) check the NN training with the other part of

the LUT data or ground measurements; and 4) apply the trained and checked NN model to a new scenario to predict the input parameters. The LUT must be general enough to include all the possible variations.

In this chapter, two LAI retrieval schemes with an NN method are examined and applied to retrieve LAI from Landsat ETM+ imagery. The first scheme retrieves LAI from the atmospherically corrected surface reflectances; the second one from the top-of-atmosphere raw radiances detected by the ETM+ sensor. The second approach was suggested by Smith (1993) who used the TOA reflectance to estimate LAI with a neural network method. No atmospheric correction was applied, instead, the effective green-band reflectance at the TOA was used by Smith (1993) to estimate LAI. Turner et al. (1999) have also tested the applicability of using raw radiance values when they assessed LAI-VI relationships across vegetation types. In their study (Turner et al., 1999), the VIs were derived from raw digital numbers (DN), radiances, TOA reflectances, and atmospherically corrected reflectances, respectively. It is meaningful, therefore, to test the relationship between TOA radiance and surface LAI with the neural network method. Similar ideas, proposed by Liang (2003a), estimated land surface broadband albedo directly from MODIS imagery.

For each scheme, a database was created through RT model simulation. The structures of these two databases were identical except for the fact that the second database incorporated atmospheric effects. Previous research, as well as my tests, has identified soil background reflectance as one of the most sensitive parameters affecting LAI

inversion. In most of the current NN training experiments, randomly selected soil reflectance was used to construct the LUT. It is believed that the use of more realistic soil reflectance data would greatly improve LAI estimates. This chapter makes use of soil reflectance derived from satellite data to drive the RT model, construct the LUT and train the neural network. For comparison with other soil reflectance options, three companion soil reflectance scenarios were tested.

The following section introduces the RT model and the principles of the neural network method. The concept of the soil reflectance index (*SRI*), database construction and the neural network training procedure are then discussed. The predicted LAI with both reflectance and radiance derived from ETM+ data will be described and validated with field measurements in the results and analysis section.

4.2 Background

4.2.1 Creating the LUT with a RT model

Creating an appropriate LUT is the first step in the use of the NN algorithm to retrieve surface biophysical parameters. The RT models relate the fundamental surface parameters (e.g., LAI and leaf optical properties) to scene reflectance for a given sun-surface-sensor geometry. As mentioned before, the main deficiency of the radiative transfer equation is the inherent complexity of its parameter inversion, a major barrier when large amounts of satellite data are used. Like the previous chapter, Kuusk's

(1995b) Markov chain reflectance model (MCRM) was used. Details about the model were described in section 3.2. In MCRM, soil spectral and directional properties are described by a spectral model (Price, 1990) in which four parameters give the proportion of each of the four spectral terms, r_{s1}, r_{s2}, r_{s3}, and r_{s4}. In

Table 4.1 Parameter values used to establish the canopy reflectance database.

Parameters	Values	Sources
Solar zenith angle	10°, 20°, 30°, 40°, 50°, 60°, and 70°	
Angstrom turbidity factor	0.1	(Kuusk, 1995a)
Leaf area index	0 ~ 10.0 by 0.1	
Leaf linear dimension/canopy height ratio	0.15	(Kuusk, 1995a)
Markov parameter describing clumping	0.8	(Chap. 3)
Eccentricity of the leaf angle distribution	0.0	(Kuusk, 1995a)
Mean leaf angle of the elliptical LAD	0.0	(Kuusk, 1995a)
Chlorophyll AB concentration	50	(Chap. 3)
Leaf equivalent water thickness	0.01	(Jacquemoud et al., 1996)
Leaf protein content	0.001	(Jacquemoud et al., 1996)
Leaf cellulose and lignin content	0.002	(Jacquemoud et al., 1996)
Leaf structure parameter	1.8	(Chap. 3)
Weight of the 1st Price function	0.01, 0.05, 0.1, 0.15, 0.2, 0.25, 0.3, 0.4, 0.5, 0.6, 0.8, 1	
Weight of the 2nd Price function	0.02	(Bicheron and Leroy, 1999)
Weight of the 3rd, and 4th Price function	0.0	(Bicheron and Leroy, 1999)

this study, a nadir viewing angle simulated the view of Landsat ETM+. A series of solar zenith angle (θ_1) values were tested. The Angstrom turbidity factor was set to 0.1 throughout this chapter. The Markov parameter, chlorophyll content and the leaf structure parameters are derived from results in chapter 3. All input parameters are listed in Table 4.1.

The soil reflectance is my particular interest here. Soil reflectance, especially for small LAI values, is one of the most sensitive parameters. When LAI increases (>3), the importance of the soil background decreases (Bicheron and Leroy, 1999). Different researchers have used various ways to deal with the soil reflectance in RT model simulations. These methods can be grouped into four categories. The first group uses the field measured soil reflectance data. For example, the soil reflectance in one of the studies (Smith, 1993) was obtained from field measurements corresponding to medium-dark and medium-bright soils. When Abuelgasim et al. (1998) inverted the geometric optical model of Li and Strahler (1992), sunlit background reflectance in the red band was chosen to represent the typical reflectance observed in this region (0.24 ~ 0.31). Qi et al. (2000) also used measured soil optical properties to invert the SAIL model. The second approach uses the soil reflectances from a soil spectral library. For example, Broge and Leblanc (2001) used minimum and maximum soil reflectances from some representative soils to create the LUT. The third approach uses the randomly generated soil reflectances. For example, Kimes et al. (2002) defined a soil parameter (S), and soil reflectances in green, red and NIR bands were calculated as S×0.2, S×0.25 and S×0.3, respectively. The final group uses reflectances derived from the soil line. For example,

the soil reflectance in the red band is randomly generated (0.02 ~ 0.40) (Baret et al., 1995) where the soil reflectance for the NIR was deduced using the soil line (ρ_{NIR}=1.253ρ_R+0.030). It should be noted that the soil line need to be obtained a priori (Baret et al., 1995).

Generally, using field-measured soil reflectance is the most accurate approach if the data are available. Reflectances from a soil spectral library may not represent real conditions in the field. Randomly generated or soil line reflectances are appropriate when they are applied to a particular soil background because they are derived from empirical observations. The soil reflectance index (*SRI*) that will be introduced and used in this study is determined from the soil line derived directly from satellite imagery.

4.2.2 Neural network method

As introduced in 1.2.3, neural networks provide a very efficient tool to establish the relationship between the simulated reflectances and the corresponding biophysical variables of interest (Baret et al., 1995; Baret and Fourty, 1997; Jin and Liu, 1997; Smith, 1993). For example, Smith inverted a simple multiple scattering model to estimate LAI from reflectances at three wavelengths which were subsequently used to train an NN that was applied to satellite observations. However, previous work (Gong et al., 1999; Qi et al., 2000; Smith, 1993) makes use of the simulated database from a RT model in both training and checking processes; i.e., part of the simulated data are used for training and the rest for testing. A significant disadvantage of checking with

simulated data is that the simulated data may not be representative of the real environmental conditions. It is more desirable to apply the training results to reflectance data derived from satellite observations, and calibrate the results with field-measured data.

The training process is usually computationally intensive. Because some of the satellite bands are closely related, only those bands that have the largest information content are applied in the training iteration. The commonly used bands are green, red, and NIR. NDVI has also been used in many studies. The benefit of using NDVI is that it exemplifies the inherent information in both red and NIR bands through the division operation. Because NDVI integrates the information content of both red and NIR, Smith only used green band (0.55 μm) reflectances and NDVI in the input training process. Simulations were made using three POLDER spectral bands (green, red and NIR) with the central wavelengths at 443, 670, and 865 nm, respectively (Kimes et al., 2002). Some researchers use both red and NIR wavelengths in the training process (Baret et al., 1995), while others use red, NIR and NDVI (Qi et al., 2000). The effect of different band combinations (NDVI as a separate band) will be examined later.

4.3 Methodology

A description of the study area, field LAI and reflectance measurements is provided in section 3.3.1. Fifty one LAI field measurements were obtained for different large homogeneous sites. For each LAI point, surface reflectances were derived from the

atmospherically corrected Landsat ETM+ data (see Chap 2). Because the conventional empirical vegetation index approach, such as using NDVI, was not appropriate for this study area (section 3.4.3), the hybrid approach to retrieve LAI was investigated.

4.3.1 The soil reflectance index (SRI)

The concept of soil reflectance index evolved from soil lines. The linear relationship between red and near infrared bare soil reflectances describe the soil line, which is widely used for the interpretation of remotely sensed data (Baret et al., 1993). Some authors assume that all the soil types might be represented by a unique "global" soil line, while Huete (1984) points out that specific soil lines better describe the optical properties of individual soil types. The formula for a soil line follows

$$\rho_{NIR} = \alpha\rho_R + \beta \tag{4.1}$$

where ρ_R, ρ_{NIR} are the reflectances in the red and near infrared bands, respectively, and α, β are the slope and intercept of the soil line that vary from one time to another. In this study, the soil line parameters for each date were determined from the red-NIR spectral space. Table 4.2 shows the soil line parameters for various dates. The intercept (β) is not a single point; instead, a buffer range is given (a more descriptive name might be soil pixel 'strip'). All pixels located in this buffer zone are treated as soil pixels. Figure 4-1 is a soil pixel strip obtained from the May 11, 2000 image.

To calculate the *SRI*, the minimum and maximum reflectances of the soil line must be calculated first, which are derived from the mean values of the lower and upper cluster of the soil pixels, using:

$$\begin{aligned} \rho_1 &= Mean(S_1) \\ \rho_2 &= Mean(S_2) \end{aligned} \tag{4.2}$$

and

$$\begin{aligned} S_1 &= \forall(\rho - \rho_{G\min}) / (\rho_{G\max} - \rho_{G\min}) < L_1 \\ S_2 &= \forall(\rho_{G\max} - \rho) / (\rho_{G\max} - \rho_{G\min}) < L_2 \end{aligned} \tag{4.3}$$

where ρ_1, ρ_2 are the minimum and maximum reflectances derived from the soil line. $\{S_1\}$ and $\{S_2\}$ are the lower and upper clusters of soil pixels used to calculate ρ_1 and ρ_2. ρ_{Gmin}, ρ_{Gmax} are the global minimum and maximum reflectances from the soil line. L_1, L_2 are two boundary percentiles. The lower and upper percentiles for calculating the minimum and maximum reflectances are listed in Table 4.2. For this analysis, both S_1 and S_2 were identified manually in R-NIR space (Figure 4-1), but they are not too difficult to be determined automatically. For simplification, S_1 and S_2 were decided based on the red band reflectance with equation (4.3).

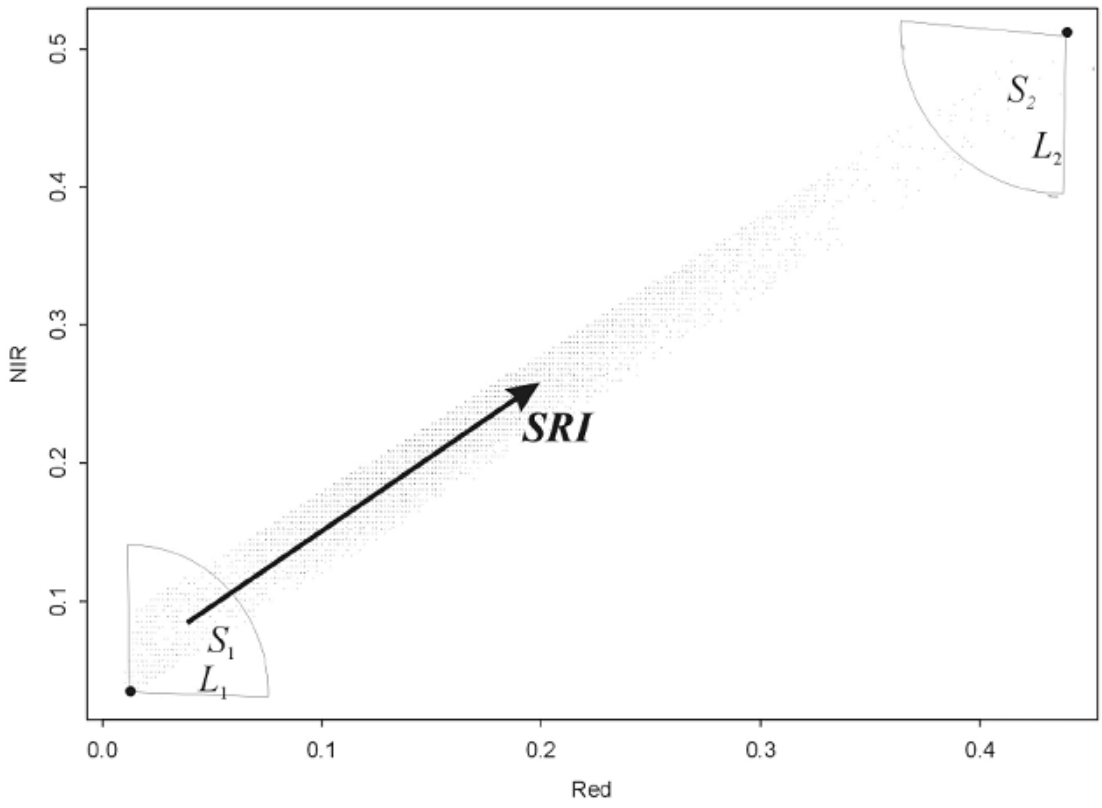

Figure 4-1 Reflectance of soil pixels in red and NIR bands. S_1 (or S_2) are a set of pixels within radius L_1 (or L_2) from the two dark points which are global minimum (ρ_{Gmin}) and maximum (ρ_{Gmax}) reflectance, respectively.

Table 4.2 Soil line parameters extracted from various dates. L_1 and L_2 are the lower and upper percentiles of the reflectance of pixels in band 3 to calculate the minimum and maximum soil reflectances used for SRI.

Dates	Slope (α)	Intercept (β)	L_1	L_2
May 11, 2000	1.0	0.02~0.08	0.01	0.02
Oct 2, 2000	1.03	0.008~0.08	0.02	0.02
Apr 28, 2001	1.1	0.008~0.08	0.01	0.02
Aug 2, 2001	1.05	0.008~0.08	0.01	0.02

Having determined the soil line from the R-NIR space, the *SRI* is defined as

$$SRI = \frac{\rho_s - \rho_1}{(\rho_2 - \rho_1)} \tag{4.4}$$

where ρ_1 and ρ_2 are the minimum and maximum red reflectances, respectively, on the soil line determined in (4.2), and ρ_s is the soil reflectance in the red band. Consequently, the soil background reflectance for each pixel can be calculated by

$$\rho_{is} = \rho_{i1} + (\rho_{i2} - \rho_{i1}) * SRI \tag{4.5}$$

where ρ_{i1}, and ρ_{i2} are the minimum and maximum soil reflectances, respectively, at band *i*.

The soil reflectance index is a new concept introduced in this study. My objective is to represent the soil reflectance in a simple way by using the *SRI*. In so doing, the MCRM model only needs minor modifications and its computation will be simplified.

4.3.2 Companion methods to calculate soil reflectance

In addition to the *SRI* method introduced above, other methods can be used to calculate the soil reflectance depending on various application scenarios. In the following part, some of them will be elaborated on.

1) Scenario 1 (SN1): MCRM has two spectral soil parameters (r_{s1} and r_{s2}) and two directional soil parameters (r_{s3} and r_{s4}). The soil reflectance reads

$$\rho_s(\lambda,\theta_1,\theta_2,\phi) = (r_{s1}\varphi_1(\lambda) + r_{s1}\varphi_1(\lambda)) * (1 + r_{s3}\theta_1\theta_2\cos\phi + r_{s4}\theta_1^2\theta_2^2) \qquad (4.6)$$

where λ, θ_1, θ_2, and ϕ are the wavelength, sun and view zenith angles, and the relative azimuth between the sun and view angles, respectively. φ_1 and φ_2 are the two first basis functions of Price (1990). In Table 4.1, the r_{s2}, r_{s3} and r_{s4} values are fixed (Bicheron and Leroy, 1999). Only the view angle at nadir (θ_2=0; ϕ=0) was considered. Soil reflectance is primarily controlled by r_{s1} (0 ~ 1.0).

2) Scenario 2 (SN2): In this scenario, the soil reflectance is based on the minimum and maximum soil reflectances measured in the field. It has been shown that the range of reflectance values for a given soil because of different soil moisture conditions is often greater than that found between soils of different taxonomic classes (Muller and Décamps, 2001). For a particular soil type, soil moisture content governs the magnitude of the soil spectral reflectance, whereas the overall shape of the spectral reflectance curve seems to be unaffected by varying moisture conditions. Soil reflectance is calculated with

$$\rho_{is} = \rho_{i1} + (\rho_{i2} - \rho_{i1}) * RI \tag{4.7}$$

where ρ_{i1} and ρ_{i2} are the minimum (wet soil) and maximum (dry soil) reflectance at band *i*. A reflectance index (*RI*) is used to define the magnitude of the soil spectral reflectance between the minimum and maximum reflectances. The major soil types in the BARC area are Codorus and Othello. The soil reflectance database of Codorus (Figure 4-2) was created from topsoil samples as part of a study by Daughtry (2001) and was used in this study. The wet and dry soil reflectances reported here were measured in the laboratory.

3) Scenario 3 (SN3): For simplification, soil reflectance is assumed to be constant over the spectrum, and the magnitude of the reflectance changes with soil moisture. Among the five representative mineral soil reflectance spectra (Stoner, 1979), the iron-dominated soil (high ion content, fine texture) is the only one that has very little variation over the spectrum. It is not my contention that this scenario represents all soil

types. Its purpose is to test the viability of the NN method. In this simulation, soil reflectance varies from 0 to 1.0.

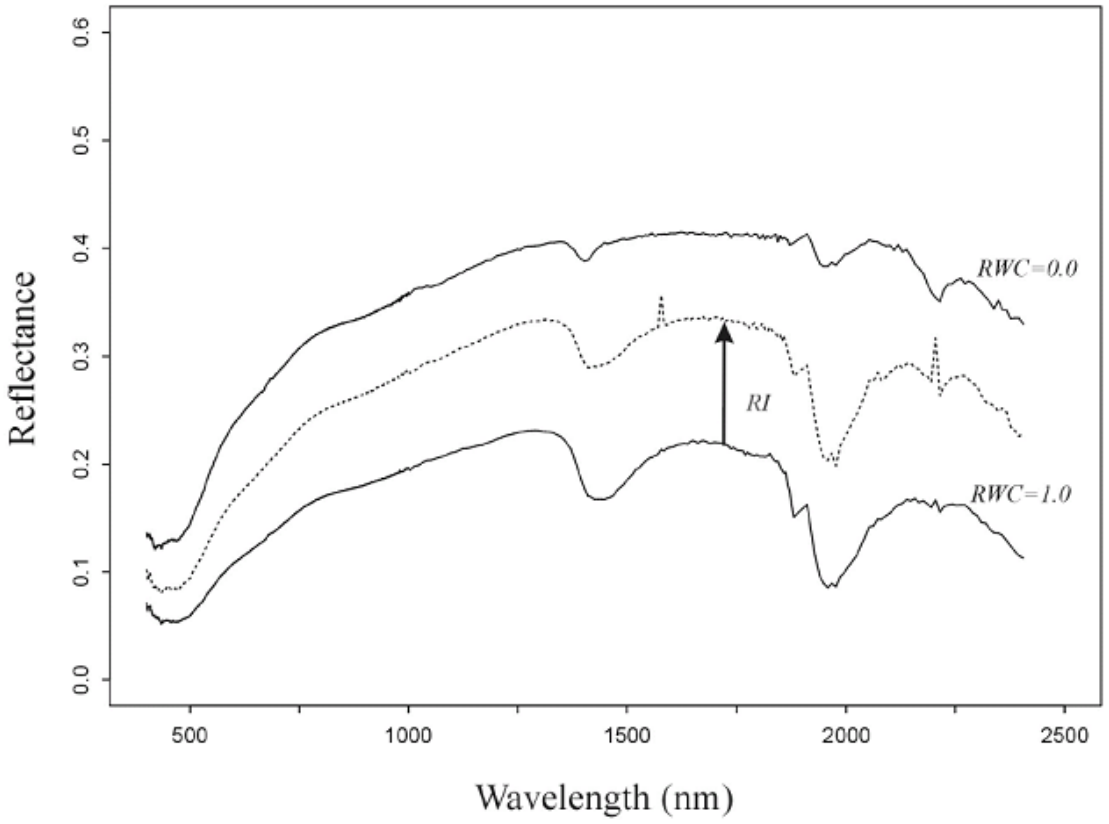

Figure 4-2 Spectral reflectance of Codorus soil at a range of relative water contents (RWC) from oven dry (RWC = 0.0) to water saturated (RWC = 1.0). *RI* (reflectance index) represents the magnitude between the minimum and maximum reflectances.

4.3.3 Creating the databases

Together with *SRI*, Kuusk's forward model MCRM was run with variable θ_l and LAI for the three comparison scenarios which required modifications to the MCRM soil reflectance calculation. SN1 makes use of the default r_{s1} in Kuusk's model. For SN2, SN3, and *SRI,* the canopy model code needed to be revised. SN2 uses the measured minimum and maximum reflectance data. SN3 assumes a common soil reflectance (varies within 0~1.0) for all bands. *SRI*, derived from the soil line of the red-NIR spectral space, reflects the instantaneous soil reflectance acquired from satellite data. Besides soil reflectance, all other parameters were the same for the four cases (*SRI*, SN1, SN2 and SN3). The parameters were fixed with the following values: S_L =0.15, C_n=0.95, C_w=0.01 cm, C_p=0.001 g/cm^2, C_c=0.002 g/cm^2, r_{s2}=0.02 and an assumed spherical leaf orientation (e=0; θ_m=0) (Table 4.1). The output is nadir reflectance in the 400-2500 nm range with a spectral resolution of 5 nm. The reflectance was integrated into Landsat ETM+ bands with the sensor spectral response function. Four LUTs were constructed from the reflectance simulations for neural network training and prediction.

The second database was based on the TOA radiance. In order to explicitly model the physical state of the land surface, the surface bidirectional reflectance distribution function (BRDF) was used. Earlier studies (Coulson et al., 1966; Koepke and Kriebel, 1978) found significant differences between radiances at TOA over natural surfaces and their Lambertian-model equivalent, even though their albedos were equal. Other studies

(Lee and Kaufman, 1986; Tanré et al., 1983) which investigated the interactions between the atmosphere and an underlying non-Lambertian surface also found that the use of the Lambertian assumption could result in a considerable amount of error in an upward radiance calculation from satellite.

For database 2, the TOA radiance, L_t, is simulated using an approximate expression (Qiu, 2001)

$$L_t = L_p + \frac{T_p F \rho_e}{1 - S\overline{\overline{\rho}}} \tag{4.8}$$

Where L_p is the atmospheric path radiance, T_p is the atmospheric transmittance of the atmosphere between the ground surface and the sensor, F is the downwelling radiative flux above the surface of zero reflectance, S is the fraction of surface radiance reflected by the atmosphere back to the surface, and ρ_e is the effective spectral reflectance of the surface expressed by:

$$\rho_e = b\rho_L(\mu_s) + (1-b)\overline{\overline{\rho}} \tag{4.9}$$

$$b = \frac{\exp\{-[1-(1-S^3)(\mu_s - 0.5)]\tau / \mu_s\}}{T_p} \tag{4.10}$$

ρ_L is regarded as the equivalent Lambertian albedo (Qiu, 2001) and $\overline{\overline{\rho}}$ is approximated by the hemispherical albedo of the surface as in (Vermote et al., 1997). τ is the aerosol optical thickness, and μ_s is the cosine of the solar zenith angle.

There are two types of coefficients in (4.8)—atmosphere related (L_p, S, T_p and F) and surface related (ρ_e and $\overline{\overline{\rho}}$). Atmospherically related coefficients were calculated using an atmospheric RT model (MODTRAN 4.0) based on a Lambertian assumption. Five atmospheric visibility values (2, 5, 10, 50 and 200 km) were used to reflect different aerosol loadings. The mid-latitude rural atmospheric profile was applied. The atmospheric water vapor content varied from 0.0 to 3.0 cm (0.0, 0.5, 1.0, 2.0, and 3.0 cm). A range of solar zenith angles (SZAs) are simulated from 10° to 70° at a 10° increment. Surface coefficients were determined from the BRDF simulation—regardless of atmospheric conditions—because surface BRDF is an intrinsic property of the surface (Qiu et al., 2001). The parameters ρ_e and $\overline{\overline{\rho}}$ were derived from the MCRM model with minor modifications. After determining L_p, S, T_p and F, the TOA radiance was calculated by (4.8).

4.3.4 Estimating LAI with the NN method

Different ETM+ band combinations can be used to invert LAI from a RT model with the NN method. All data points in the two databases were used to train the NN. ETM+ reflectance, radiance and field-measured LAI were used in the verification process. The

training and checking data sets included reflectances in the green, red, NIR and middle infrared (MIR) spectral region as well as computed NDVI (Table 4.3 for database 1). The green, red, NIR and MIR band radiances were also used for the training and checking of database 2. (NDVI for database 2 was calculated using red and NIR radiances) The R-square value and RMSE were calculated for different scenarios and *SRI* for each band combination. I did not exhaust all possible band combinations, but did evaluate the most commonly used.

The computations were performed using the Splus neural network tool (Venables and Ripley, 1994). After identifying the best band combination, the training process was conducted with the corresponding LUT and field measurements were used for verification. The best band combination was used to map LAI from the ETM+ imagery.

4.4 Results and analysis

4.4.1 LAI retrieval from ETM+ surface reflectance

In Table 4.3, all RMSEs<1.0 are italicized. For SN1, all of the RMSEs are greater than 1.0. For SN2, three combinations have a RMSE<1.0, while for SN3, six band combinations had that value. The best results were observed for the *SRI* which had seven RMSE<1.0. Including NDVI improved the retrieval accuracy to some extent. For example, the R^2/RMSE for the band combinations of (2, 3), (2, 4), and (2, 5) are 0.55/1.64, 0.75/1.67, and 0.01/2.04; while R^2/RMSE for (2, 3, NDVI), (2, 4, NDVI), and

(2, 5, NDVI) are 0.76/0.91, 0.75/1.07, and 0.50/1.52, respectively. Because NDVI incorporates the information content of bands 3 and 4, the R^2/RMSE of (3, 4) and (3, 4, NDVI) were almost the same. In addition, the introduction of the green band (i.e., band 2) did not improve the results. The R^2/RMSE for (3, NDVI) and (4, NDVI) decreased from 0.80/0.85 and 0.80/0.80 to 0.76/0.91 and 0.75/1.07 when band 2 was used. Moreover, poor results (RMSE<1.0) were obtained when band 5 was used and unacceptable results occurred when more than four bands (NDVI as a separate band) were used.

4.4.2 LAI retrieval from ETM+ raw radiance

The results of LAI retrieval from the ETM+ raw radiance are displayed in Table 4.4 (RMSE<1.5 are italicized). In contrast to the results shown in Table 4.3, there is no combination for SN1 whose RMSE is less than 1.5. This implies that SN1 may not be appropriate for TOA radiance calculation. In addition, only one RMSE was less than 1.5 for the TOA radiance with SN2. This is not surprising because the laboratory-measured soil reflectance did not fully represent actual field conditions. Errors were also introduced because database 2 was calculated from an empirical equation (4.8). For SN3, there is only one combination (4, NDVI) with an RMSE<1.5. The best results are seen with the combination of band 4 (NIR) and NDVI (R^2=0.74, RMSE=1.17) for the SRI case which suggests that this band combination should be used for estimating LAI from TOA radiance. These results may be explained by the fact that visible bands are significantly affected by atmospheric conditions,

Table 4.3 Comparison of R^2 and RMSE for different neural network scenarios and the application of the soil reflectance index (SRI). Band combinations use surface reflectances simulated from MCRM.

Band	SN1		SN2		SN3		SRI	
combination	R^2	RMSE	R^2	RMSE	R^2	RMSE	R^2	RMSE
2, 3	0.4023	1.6349	0.2101	2.7	0.6075	1.6784	0.5522	1.6389
2, 4	0.7722	1.032	0.6236	1.7824	*0.8361*	*0.725*	0.7536	1.6655
2, 5	0.1054	2.3065	0.0161	4.2217	0.0447	2.1306	0.0139	2.0362
2, NDVI	0.7459	1.1813	0.7264	1.087	0.7196	1.2436	*0.7378*	*0.9916*
3, 4	0.8081	1.1332	0.6816	1.3071	0.8137	0.9254	*0.8015*	*0.8095*
3, 5	0.3062	2.6583	0.0245	3.1032	0.0716	2.0174	0.1333	1.9811
3, NDVI	0.8013	1.1285	0.7383	1.1772	*0.8101*	*0.9192*	*0.7952*	*0.8508*
4, 5	0.6078	19.161	0.7158	18.095	0.7803	3.7898	0.8196	4.9209
4, NDVI	0.8115	1.1009	*0.7967*	*0.9494*	*0.816*	*0.8942*	*0.8021*	*0.8048*
5, NDVI	0.5332	2.145	0.0261	3.2974	0.5214	1.7316	0.5452	1.5214
2, 3, 4	0.4571	1.2638	*0.7709*	*0.9387*	*0.7925*	*0.9132*	*0.7742*	*0.9551*
2, 3, 5	0.3488	20.071	0.0401	9.285	0.2154	3.651	0.0581	5.3729
2, 3, NDVI	0.561	1.4124	0.7399	1.0352	0.7319	1.3805	*0.7597*	*0.9063*
2, 4, 5	0.0552	14.559	0.0725	13.155	0.0151	11.36	0.2765	17.423
2, 4, NDVI	0.2106	2.7003	0.0901	2.6999	*0.8247*	*0.8444*	0.745	1.066
2, 5, NDVI	0.6934	1.6588	0.3775	2.0413	0.4265	1.7554	0.4953	1.5194
3, 4, 5	0.0038	40.357	0.3078	32.144	0.0689	12.806	0.5972	19.22
3, 4, NDVI	0.8071	1.106	*0.7996*	*0.9806*	*0.8141*	*0.9019*	*0.8051*	*0.8022*
3, 5, NDVI	0.051	8.7336	0.3346	2.1553	0.2037	2.0226	0.3095	2.6856
4, 5, NDVI	0.6387	31.337	0.0377	2.28	0.0705	7.1147	0.2002	27.52
2, 3, 4, 5	0.029	26.226	0.2964	10.917	0.1435	5.2947	0.3338	7.2955
2, 3, 4, NDVI	0.3378	1.4478	0.2846	2.7	0.0042	2.7001	0.6949	1.2642
2, 3, 5, NDVI	0.2933	6.4625	0.3254	2.2912	0.0002	2.0724	0.7848	1.2787
2, 4, 5, NDVI	0.5788	1.6387	0.5299	20.077	0.6317	8.4994	0.0872	27.467
3, 4, 5, NDVI	0.7551	18.533	0.4793	25.14	0.0916	1.8153	0.7141	3.2424
2, 3, 4, 5, NDVI	0.2053	18.157	0.0818	12.027	0.145	6.5945	0.159	2.6857

Table 4.4 Same to Table 4.3 , but using TOA radiance in band combinations.

Band combination	SN1		SN2		SN3		*SRI*	
	R^2	RMSE	R^2	RMSE	R^2	RMSE	R^2	RMSE
2, 3	0.1700	5.2625	0.0223	40.4603	0.0822	67.5674	0.0438	29.2868
2, 4	0.0391	2.0105	0.0002	2.3056	0.0648	2.1652	0.1048	2.2036
2, 5	0.0702	4.3581	0.0712	3.0718	0.0690	2.3562	0.0816	2.2777
2, NDVI	0.5557	2.1632	0.5397	24.3915	0.2150	22.6303	0.4674	3.4295
3, 4	0.4003	2.1518	*0.6235*	*1.3118*	0.6955	1.6551	0.4408	1.7748
3, 5	0.0052	2.2525	0.0312	2.8464	0.0826	2.6193	0.0159	2.3495
3, NDVI	0.6699	1.9020	0.5193	2.4603	0.5755	1.8780	0.3285	1.9902
4, 5	0.0090	6.0347	0.0027	5.6974	0.0174	7.4843	0.0004	55.4644
4, NDVI	0.2131	2.3706	0.6385	1.5869	*0.7372*	*1.2019*	*0.7442*	*1.1701*
5, NDVI	0.0010	2.1486	0.0307	2.6477	0.0303	2.5607	0.0603	2.6699
2, 3, 4	0.0156	1.7759	0.0121	2.0391	0.0568	1.7057	0.0012	1.9701
2, 3, 5	0.0307	4.0950	0.0040	5.3889	0.0833	84.7633	0.0932	3.0354
2, 3, NDVI	0.0891	2.9434	0.6875	11.2830	0.4711	75.9847	0.0447	68.7834
2, 4, 5	0.0479	5.3905	0.0694	4.4210	0.0885	4.5779	0.0079	4.9147
2, 4, NDVI	0.5549	2.2269	0.4978	2.6760	0.6466	3.9618	0.6875	2.8680
2, 5, NDVI	0.0219	17.4510	0.4069	9.7468	0.0049	8.7707	0.5951	10.6470
3, 4, 5	0.0462	6.0392	0.0094	4.9709	0.0098	11.2123	0.0013	5.5459
3, 4, NDVI	0.6377	1.8139	0.5693	1.7601	0.3793	1.7854	0.5496	1.7832
3, 5, NDVI	0.0180	5.5558	0.1570	1.9513	0.6091	1.6705	*0.5330*	*1.4873*
4, 5, NDVI	0.0000	4.3379	0.0021	27.1991	0.5849	1.9930	0.5401	3.0628
2, 3, 4, 5	0.0659	5.1442	0.1017	3.7472	0.0097	6.4394	0.1030	3.4869
2, 3, 4, NDVI	0.1840	2.5507	0.1762	2.0701	0.3513	15.2807	0.0490	2.4762
2, 3, 5, NDVI	0.1361	5.8437	0.0120	162.7613	0.0383	159.8680	0.0343	108.8274
2, 4, 5, NDVI	0.0148	6.0143	0.1189	44.0487	0.0681	55.9402	0.5703	59.6755
3, 4, 5, NDVI	0.0615	5.4126	0.4532	80.8209	0.0944	45.6471	0.2572	37.4586
2, 3, 4, 5, NDVI	0.0001	4.6033	0.0014	45.7972	0.0001	129.6289	0.0086	28.8632

while infrared bands are not. Moreover, NDVI is not significantly affected by atmospheric effects because these factors are normalized out in the process of calculation (Kaufman and Tanré, 1992).

Similar to database 1, the results of database 2 were very poor when the combination used more than 4 bands. The effect of adding NDVI varies with different band combinations. For most cases, using NDVI did not improve the results. The introduction of green band radiance deteriorated the results to some extent and the effect of band 5 was also negative—all RMSEs >1.5 when band 5 was used.

For SN2, SN3 and *SRI*, database 1 performed much better than database 2. It is not surprising that LAI could be better estimated from atmospherically corrected surface reflectance data than from raw TOA radiances. Similar results were reported by Turner et al. (1999) who used both reflectance and radiance to calculate VIs and found that the LAI-VI relationships based on reflectance data were stronger than those based on radiance data. In this analysis, a perfect atmospheric correction has been assumed for database 1. Yet, if it is believed that atmospheric correction introduced large uncertainties to the surface reflectance, the second scheme might be a better solution.

The best results were obtained from (3,4) in database 1 with the *SRI* method. Therefore, Landsat ETM+ reflectances in the red and NIR were picked to map LAI with the trained NN. The strategy behind this selection was based on choosing the best R^2 and RMSE as well as considering computation efficiency. This result was also obtained by Baret et al.

(1995). All simulated points in the LUT were used to train the NN which was then applied to Landsat ETM+ red and NIR reflectances to predict LAI.

4.4.3 Validation

To validate the proposed approach, the NN derived LAIs were compared with field measurements. Figure 4-3 shows that the *SRI* method performs well (R^2=0.801, RMSE=0.811) in estimating LAI. The constant soil reflectance approach in SN3 also performs well (R^2=0.814, RMSE=0.925). When LAI>4.0, both SN1 and SN2 tend to underestimate LAI for the two hairy vetch points and a wheat point (Figure 4-3e~h). Using SN1 seems unrealistic, and SN2 is not representative for this study area. Although Kuusk (1998) mentioned that MCRM may not work well for forests, most of the retrieved forest LAIs agreed well with the field-measured green LAIs (Figure 4-4) for LAI<3. There is a strong bias for high LAI (>3), possibly caused by the saturation of the forest reflectance. Among the four options, the largest deviation is seen in SN2 (Figure 4-4).

Errors caused by model simulation, sensor calibration or measurement should be taken into account. To test the sensitivity of the neural network approach to uncertainty in the input reflectance, three bias levels (±15%, ±10% and ±5%) were generated for evaluation. The relative errors were added to the ETM+ surface reflectance and TOA radiance dataset. The relative R^2 and RMSE differences were calculated between the biased and the original datasets

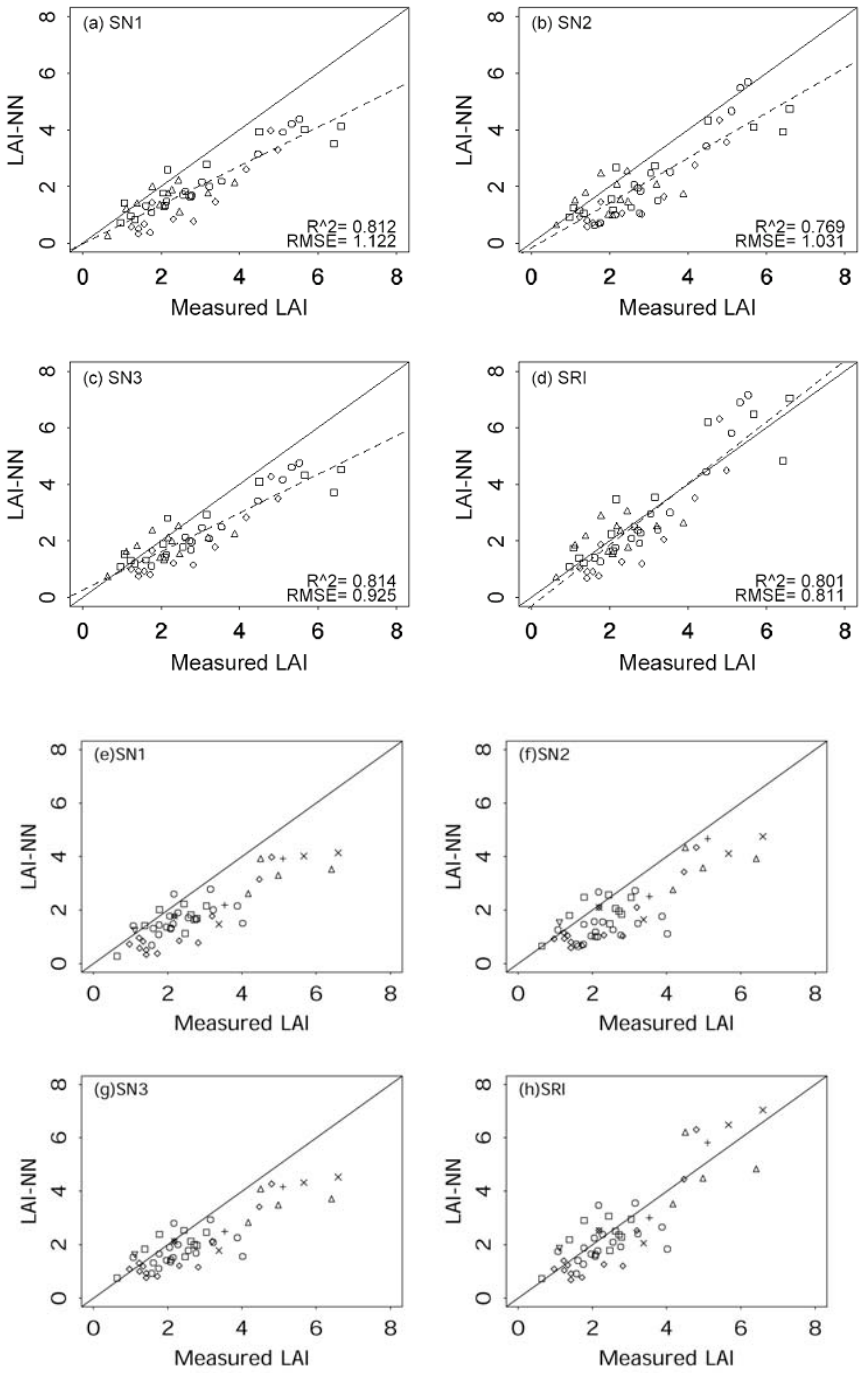

Figure 4-3 Comparison of LAI-NN with field LAI. LAI-NN is estimated from Landsat ETM+ images with the neural network methods for four different soil reflectance options: a) SN1; b) SN2; c) SN3; and d) SRI. Symbols: May 11 (□) and Oct 2 (○) 2000 and Apr 28 (◇) and Aug 2 (△) 2001. (e)~h) compare LAI of different cover types, alfalfa (▽), barley, hairy vetch and orchard grass (×), corn (□), deciduous forest (○), grass (◇), soybean (+), and wheat (△). R^2: R square. The solid line is the 1:1 line, and the dashed one the regression line.

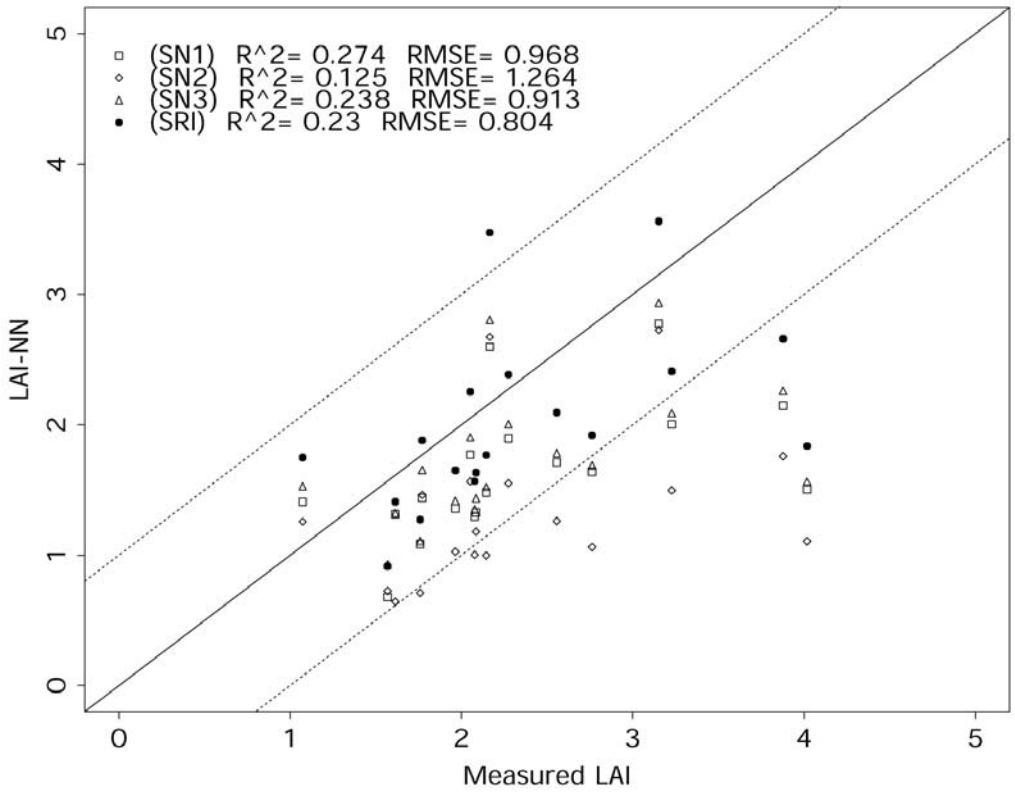

Figure 4-4 Comparison of retrieved forest LAI-NN values retrieved with SN1 (□), SN2 (◇), SN3 (Δ) and the SRI (•), respectively, with measure LAI. The intercepts of the dashed lines are ±1.

$$(\mathbf{R}'-\mathbf{R})/\mathbf{R}$$

where **R** and **R′** are the R^2 or RMSE obtained using the original and biased datasets, respectively. Table 4.5 lists the relative R^2 and RMSE differences using *SRI*. This table includes band combinations that performed well—bands 3 and 4 for surface reflectance and 4, NDVI for TOA radiance.

For the surface reflectance, the R^2 nearly keeps constant across different noise levels. The RMSE values are lower at low noise levels and are a little biased when the absolute biases are greater than 10%. This indicates that this approach is robust to different reflectance noise levels and thus lends itself to practical applications. On the other hand, the noise has significant effects on LAI estimated from TOA radiance. All R^2 are much lower than the original values for different bias levels. The RMSE is lower at low noise levels but increases quickly when noise increases. This is an indication that using TOA radiance may be unrealistic for LAI estimation if there are too many uncertainties.

4.4.4 Comparison with the genetic algorithm results

It is interesting to compare the LAI results from both the GA optimization method in the previous chapter and the NN approach developed in this chapter. The results are shown in Figure 4-5. This scatterplot compares the LAI values from both the neural network method and GA method for two days (Apr 28 and Aug 2, 2001). The results from the two approaches generally agree well with each other (R^2=0.943 and 0.883 for the two

Table 4.5 Relative R^2 and the RMSE differences for different bias levels. Band (3,4) is used for surface reflectance and (4, NDVI) for TOA radiance.

Bias levels		-15%	-10%	-5%	+5%	+10%	+15%
(3,4)	R^2	0.0034	0.0035	0.0021	-0.0026	-0.0045	-0.0053
	RMSE	0.1282	-0.0051	-0.0521	0.1711	0.4091	0.6973
(4,NDVI)	R^2	-0.9219	-0.8547	-0.7469	-0.6293	-0.7174	-0.7729
	RMSE	0.8336	0.7151	0.6228	1.3337	3.2187	6.1858

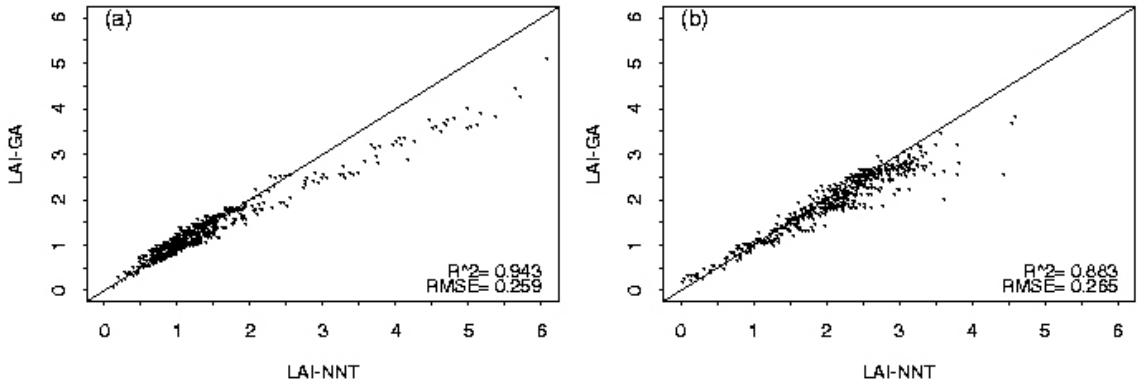

Figure 4-5 Comparison of LAI derived from the neural network method (LAI-NNT) and the genetic algorithm (LAI-GA) of two 30×30 pixels regions in Figure 3-10. (a) Apr 28, 2001; (b) Aug 2, 2001.

dates, respectively). The RMSE is less than 0.26, very small compared with the measurement uncertainties. For both dates, LAI-NNT is larger than LAI-GA for higher LAI values (>3).

In retrieving LAI with the genetic algorithm, the surface background reflectance is the same as scenario 1 (SN1) in this chapter (equation 4.6). The new *SRI* concept developed in this chapter was not applied in the GA experiments in the previous chapter. In addition, the neural network simulation work in this chapter used some results (e.g. S_z, C_{ab} and N) derived from the previous GA optimization outputs to represent the general conditions of the study area. While further work is needed for the GA method, it is believed that that the neural network is more practical in its current stage.

4.4.5 LAI mapping

NN training results from the *SRI* (Figure 4-3) were used to estimate LAI for four Landsat ETM+ images (Figure 4-6). The May 11, and Oct. 2, 2000 images are 512 × 512 and 600 × 600 pixels, respectively. The Apr. 28, and Aug. 2, 2001 images are 300 × 300 each. In Figure 4-6, brown areas were either bare land or roads, and the gray-white areas were construction sites. The yellow and green pixels were either crops or forests. The LAI maps correspond well with local landscape characteristics. Statistics from the LAI maps are shown in Table 4.6. May 11, 2000 and Aug. 2, 2001 have the highest mean LAI values. The LAI standard deviation of May 11, 2000 is greater than that of Aug. 2, 2001, possibly due to variability caused by differing planting and emergence dates. Most areas

have LAI values less than 4.0 (Table 4.6). However, some dark green pixels on the Apr. 28, 2001 LAI-NN map were dense grasses with an LAI-NN greater than 6.0. Because this method seems to provide accurate estimates of vegetation amounts throughout the growing season, this approach could be applied to a large area for regional LAI mapping (see an example in Figure 4-7). Large area LAI estimation is valuable for comparison with LAI products from other sensors such as MODIS (next chapter) or MISR.

4.5 Summary

This chapter has demonstrated how a hybrid approach (RT+NN) can be used to retrieve LAI from the Landsat 7 ETM+ surface reflectance and TOA radiance. The NN was trained with two databases to estimate LAI from atmospherically corrected surface reflectance (database 1) and raw TOA radiance (database 2). Database 1 was constructed with a canopy RT model and database 2 with the combined atmospheric and canopy RT models. A soil reflectance index (*SRI*) was proposed to account for soil background reflectance. To define the *SRI*, the shape of the soil-line in the red-NIR spectral space is needed. *SRI* minimizes the number of parameters involved in computing the soil spectral reflectance.

The results show that LAI can be obtained through the NN approach from both surface reflectance and TOA radiance. The outputs were compared with field-measured LAI datasets from four different dates. The surface reflectance approach resulted in an

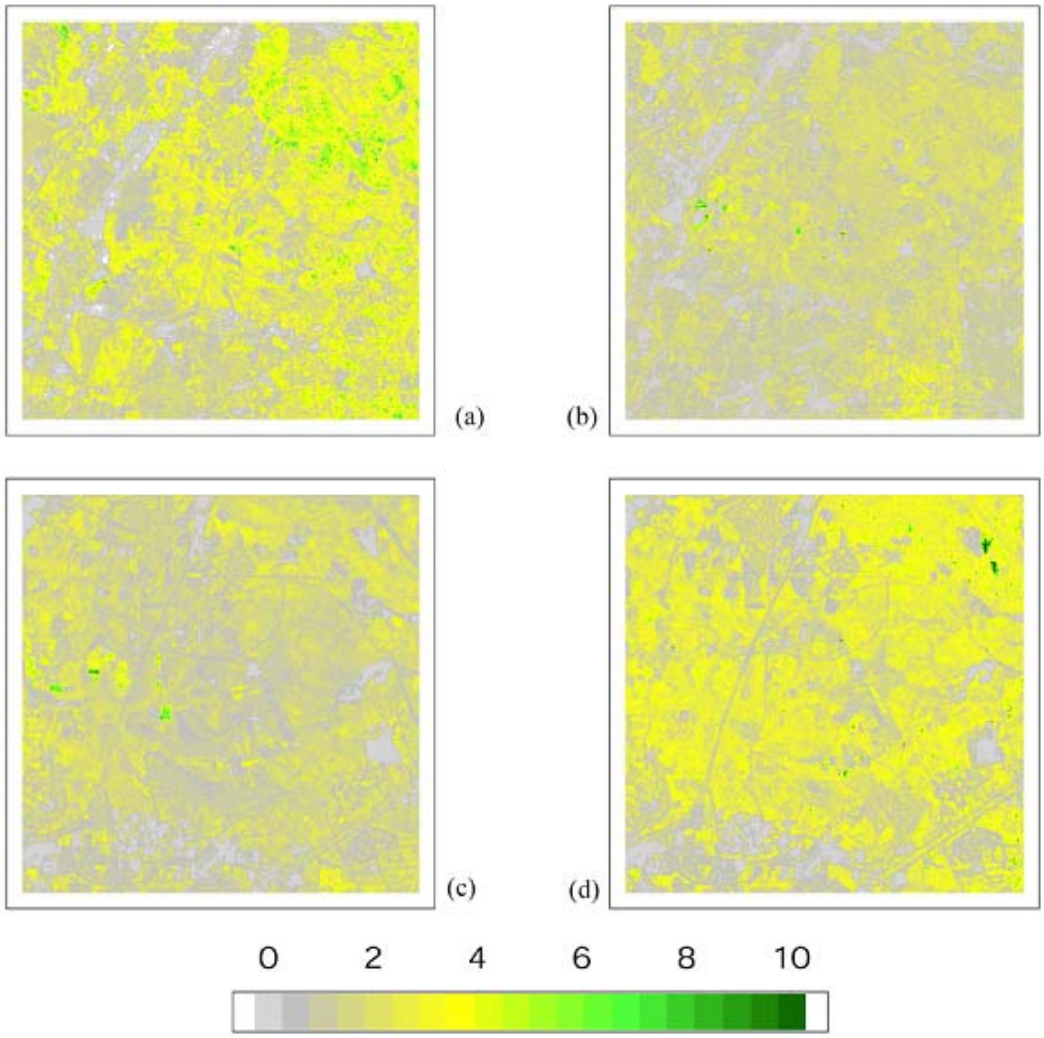

Figure 4-6 LAI maps generated with the neural network method from ETM+ reflectances. (a) May 11, 2000; (b) Oct 2, 2000; (c) Apr 28, 2001; (d) Aug 2, 2001. Band (3, 4) and SRI are used in the NN training.

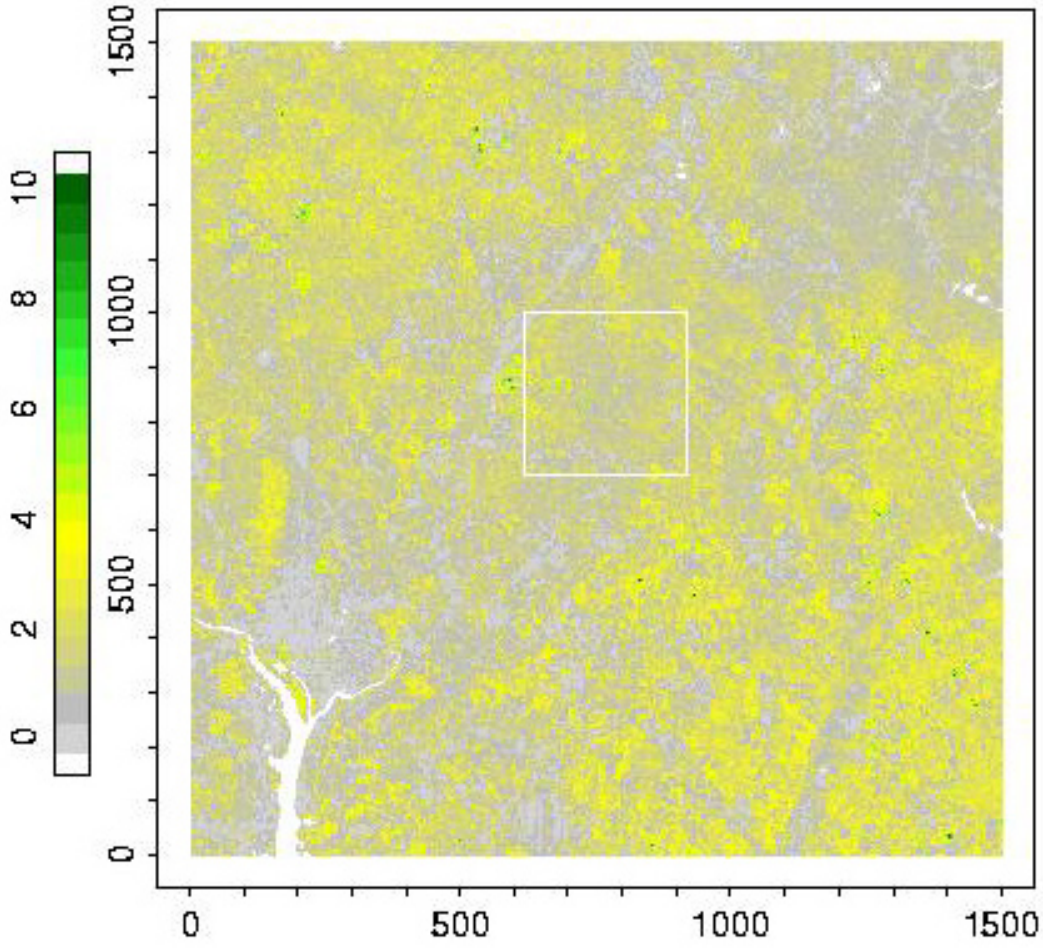

Figure 4-7 LAI distribution estimated using the proposed hybrid approach with ETM+ for Apr 28, 2001 over the Washington, DC area. White box shows the Figure 4-6c area. Size: 1500 by 1500 pixels.

Table 4.6 Statistics of the LAI-NN estimated from the four ETM+ reflectances.

Dates	Minimum	Maximum	Mean LAI	Standard deviation	LAI<4 pixels (%)
May 11, 2000	0.0	6.39	2.28	1.31	91.43
Oct 2, 2000	0.0	6.44	1.54	0.76	99.5
Apr 28, 2001	0.0	6.22	1.57	0.68	99.45
Aug 2, 2001	0.0	8.81	2.26	0.97	98.15

R^2=0.801 and RMSE=0.811 using input bands 3 and 4. When the TOA radiance of band 4 and NDVI were used, the results were not as good: R^2=0.74, RMSE=1.17. Estimating LAI from TOA radiance does, however, have the advantage of avoiding performing a complicated atmospheric correction process. In general, bands 3 and 4 are recommended for estimating LAI from ETM+ surface reflectance, while band 4 and NDVI are recommended if TOA radiance is used. The sensitivity experiment showed that this approach is very robust, especially when surface reflectance is used.

Chapter 5 Mapping LAI from MODIS Using a Hybrid Inversion Method

5.1 Introduction

In Chapter 4, a hybrid approach (RT+NN) was developed to estimate LAI from high resolution Landsat ETM+ data. Its applicability to MODIS, still unknown, requires further experiments and validation work. Therefore, the objective of this chapter is to explore the hybrid method to estimate LAI from moderate resolution sensors, such as MODIS. In addition, two nonparametric algorithms, NN and PPR will be compared in this chapter.

The MODIS science team is producing an LAI product systematically. The land biome type classification is indispensable for this algorithm. It makes use of predefined leaf optical and structural properties for each biome type. Thus, the accuracy of the algorithm is dependent on the accuracy of the land cover classification. Another well-recognized limitation in the MODIS LAI algorithm is its inclusion of pre-defined soil reflectances (Knyazikhin et al., 1998b). In Chapter 4, a soil reflectance index (SRI) derived from the satellite image was developed to represent the soil reflectance when the satellite overpasses. Thus, the intensive computation using canopy RT simulation is greatly simplified.

Several validation techniques have been used to determine the uncertainties of land surface products, such as comparisons with *in situ* data, with products from other

sensors, trend analysis, and application analysis (Morisette et al., 2002; Privette et al., 1998). It is also crucial to compare the LAI products with those derived from other independent methods.

The hybrid algorithm is presented in the following sections. It starts with a brief summary of the study area and experiment data. After the ETM+ data preprocessing, the SRI is determined from the ETM+ reflectance image. With inputs of different plant and environment parameters, a big database is simulated for nonparametric training. The trained results are then used in the prediction step to produce LAI maps from MODIS data. The experimental design is illustrated in Figure 5-1.

5.1.1 The MODIS LAI algorithm

The operational MODIS LAI algorithm makes uses of vegetation maps as a priori information to constrain the vegetation structural and optical parameter space (Myneni et al., 1997). Six major biomes were used: Grasses and Cereal Crops (biome 1), Shrubs (biome 2), Broadleaf Crops (biome 3), Savannas (biome 4), Broadleaf Forests (biome 5) and Needle Forests (biome 6). For each land pixel, numerical solutions of the three-dimensional canopy radiative transfer equation are used to model the bi-directional reflectance factors (BRF) of the biomes for varying sun-view geometry and canopy/soil patterns (Knyazikhin et al., 1998a; Knyazikhin et al., 1998b). A look-up table is constructed which includes a suite of representative canopy variables and

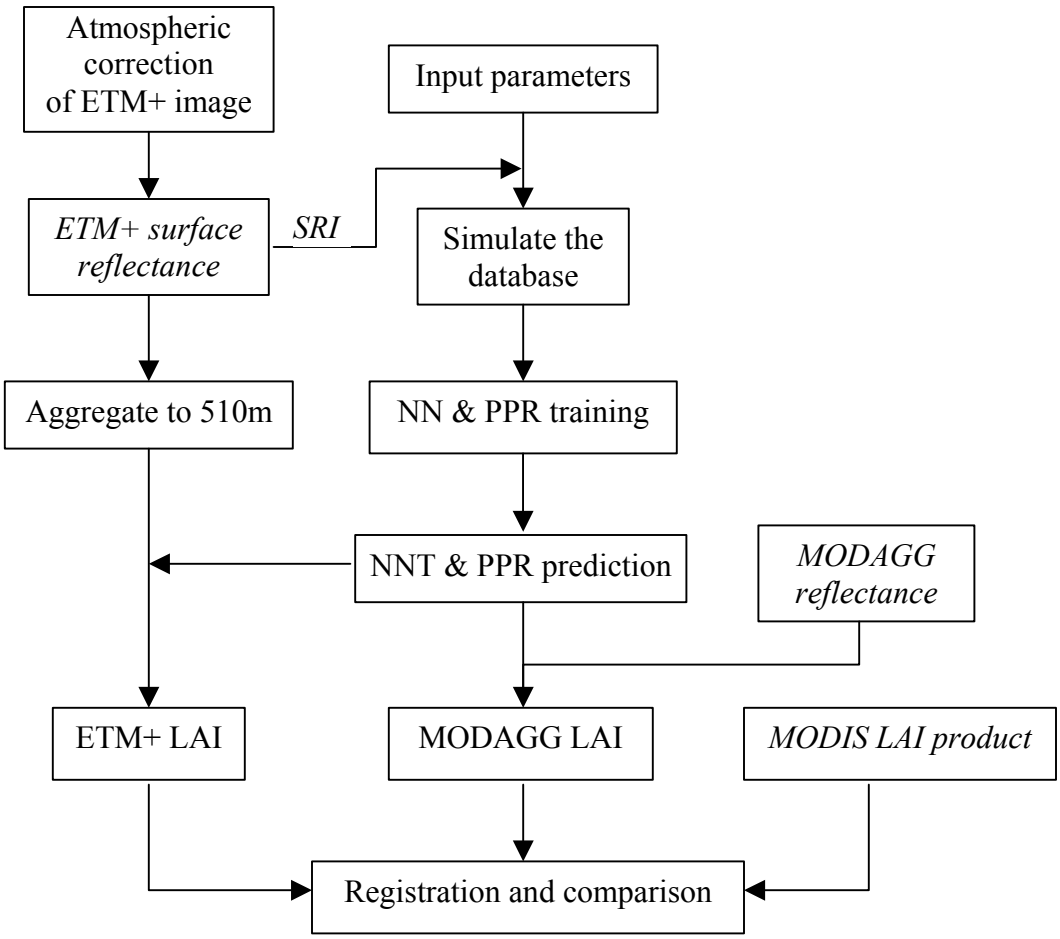

Figure 5-1 Work flow of the hybrid approach to estimating leaf area index with remote sensing imagery.

soil characteristics of each biome. The present version of the LUT contains 25 patterns of effective ground reflectances evaluated from the soil reflectance model of Jacquemoud et al. (1992). By comparing the observed and modeled BRFs, LAI is retrieved. The solution is usually not unique; therefore, the mean values of LAI averaged over all acceptable values and their dispersions are taken as the retrievals and their uncertainties (Knyazikhin et al., 1998a; Knyazikhin et al., 1998b). Should this main algorithm fail, a back-up algorithm is triggered to estimate LAI using NDVI. The backup algorithm makes use of the pixel NDVI and a unique NDVI-LAI relationship for each biome. The LAI product has a value between 0.0 and 8.0 assigned to each 1-km cell of the global gridded database.

The MODIS LAI algorithm has been prototyped with various sensors such as POLDER, LASUR, Landsat Thematic Mapper (TM), and SeaWiFS data (Tian et al., 2000; Wang et al., 2001; Zhang et al., 2000). It is noted that the operation and accuracy of the MODIS LAI algorithm is based on other MODIS upstream products. First of all, this algorithm is based on six biome types; misclassification will lead to accumuated errors in the final LAI products. Second, the accuracy of this algorithm is also dependant on the daily atmosphere-corrected spectral BRDF in the solar spectrum (MOD09). More importantly, some variables, such as the soil refelctance, leaf reflectance and transmittance, need to be fixed with a priori constants. However, most of these variables vary dramatically. Fixing them with constants will bring large uncertainties (Walthall et al., 2000).

5.2 Methodology

5.2.1 Data preparation

In the study area at Beltsville, Maryland, two clear Landsat ETM+ images were obtained on April 28 and August 2, 2001, respectively (path 15/row 33). They represent two different vegetation growing states. In late April, the vegetation and crops are in the typical early-spring growing season. In early August, crops are in the middle-late growing season. ETM+ and MODIS are in the same orbit, about 45 minutes apart, on Landsat 7 and Terra, respectively. The MODIS imagery over the test site was acquired on the same day as ETM+. The MODIS imagery had a very small viewing angle (<1° for both images at the 10×10 km core site or <8° over the ETM+ coverage). Hence, both ETM+ and MODAGG reflectance were treated as nadir view. The solar zenith angles (SZA) were 31.41° and 30.19° for the two ETM+ images respectively, and 27.22° and 25.55° for the MODIS images.

In the MODIS land data production sequence, the Level 2G (MOD09) and level 3 data are accumulated to create the LAI/FPAR products as well as other land data products (Justice et al., 2002). The MODIS Level 2G (MOD09) data are daily, cloud-cleared, and atmospherically-corrected surface reflectances. The level 3 MODAGG data are 1 km intermediate products aggregated and binned daily from the MOD09 1-7 channels. The MODAGG data are used as the primary input for the MOD43B BRDF/Albedo product (MOD43B), the nadir BRDF adjusted reflectance (NBAR or MOD43B4), and the 16-

day enhanced vegetation index product (MOD13A2). MODAGG is directly used to produce the MODIS LAI products because it has the required projections and spatial resolution. These constitute very sound reasons to utilize the MODAGG data to test the new approach.

5.2.2 Atmospheric correction, aggregation and registration of ETM+ imagery

Atmospheric correction of the clear ETM+ imagery was undertaken using the methods in Chapter 2. After the ETM+ reflectance data were calibrated with field-measured reflectance, they were aggregated into the MODIS resolutions. The ETM+ data from band 3 and band 4 in the study area were spatially averaged using commercial image software to generate data of 240-, 510-, and 990-m resolutions, close to the MODIS 250, 500 and 1000m resolutions. This aggregation was accomplished by simply averaging every 8× 8, 17×17, and 33×33 ETM+ pixels. The spatial averaging was just a simplification of the complicated spatial convolution and resampling process to aggregate ETM+ imagery to MODIS sensor resolution (Barker et al., 1992). The aggregated 510m resolution ETM+ imagery was then registered with the 1 km MODIS imagery by manually selecting the common ground control points (GCP), such as rivers, coastal lines and other distinct ground features. It is clear that the accuracy of validation depends to a large extent on the accuracy of the spatial registration. In this study, an average registration error of less than one MODIS pixel was achieved for both month's images.

While the overall mean value remains invariant, the spatial aggregation results in a decreased variance, and thus leads to the discrepancy within different ground cover types. This is accompanied by an increased number of mixed pixels and in the degree of spatial mixture within pixels when the spatial resolution becomes coarser. It is noted that I did not average high-resolution LAI data, but the reflectance data. This is mainly because of the different spatial scaling characteristics of reflectance and LAI. Unlike the surface reflectance, the situation is quite different for the LAI in the scaling process. Liang's (2000) work has shown that LAI values retrieved from coarse-resolution remotely sensed data are not always equal to the true LAI values if the surface is highly heterogeneous. The simulation work conducted by Tian et al. (2003) also indicates that LAI retrieval errors at coarse resolution are inversely related to the proportion of the dominant land cover in the mixed pixel. Those simulations indicate that one cannot simply average and aggregate the high-resolution LAI values and compare them with coarse resolution LAI. In this study, LAI inaccuracies were still unavoidable even when first averaging reflectances and then performing LAI retrievals. The error increases correlative to decreasing resolution because of the nonlinear relationship between LAI and reflectances (Liang, 2000; Weiss et al., 2000).

5.2.3 Determining the soil reflectance index

In the previous chapter, the concept of soil reflectance index (*SRI*) was proposed based on the "soil line." The *SRI* is a simplification of the complex soil radiometric properties and can be directly derived from the satellite data. One merit of the *SRI* is that it is based

on the soil line parameters obtained from the instantaneous red-NIR reflectance space. Examples of the red-NIR reflectance scatterplot are shown in Figure 5-2. The intercept (β) is not a single value. Instead, a buffer range is given. All pixels located in this buffer zone are treated as soil pixels. Figure 5-2 shows examples of the soil pixel stripe (within dashed lines) obtained from the aggregated ETM+ and MODAGG data.

As discussed above, upscaling reflectance from the 30m resolution (ETM+) to the 1 km resolution (MODIS) is highly linear (Liang, 2000). Therefore, the 30m ETM+ reflectance was averaged to the MODIS products of 1 km without introducing any significant errors. A typical red-NIR reflectance scatterplot would look like Figure 5-2, resembling a slant 'V' shape. Figure 5-2 illustrates the spectral space of red and near-infrared reflectances (Red-NIR) for different spatial resolutions. The study area, a typical heterogeneous surface, includes several common land cover types, such as vegetation (forests, grasses and crops), built-up areas, bare soils and water bodies. The soil line can easily be drawn manually from this figure. When the red-NIR space was scaled from high-resolution to moderate and low resolution, the 'V' shape changed accordingly because of the pixel mixing. This process was nonlinear and resulted in an averaging filter effect for all pixels, i.e, the dark surface objects appeared brighter and bright surface objects darker. While the distribution of the NIR reflectance remained similar for different resolutions, the degradation of the red reflectance was very distinct when the resolution decreased. This should be attributed to the dissolution of the soil pixels into their neighboring vegetated pixels. This decrease in red reflectance is particular to this study site because the scaling process is dependent on the mixed pixel element fraction. Most likely, other trends of red-NIR shrinking could be seen at other sites.

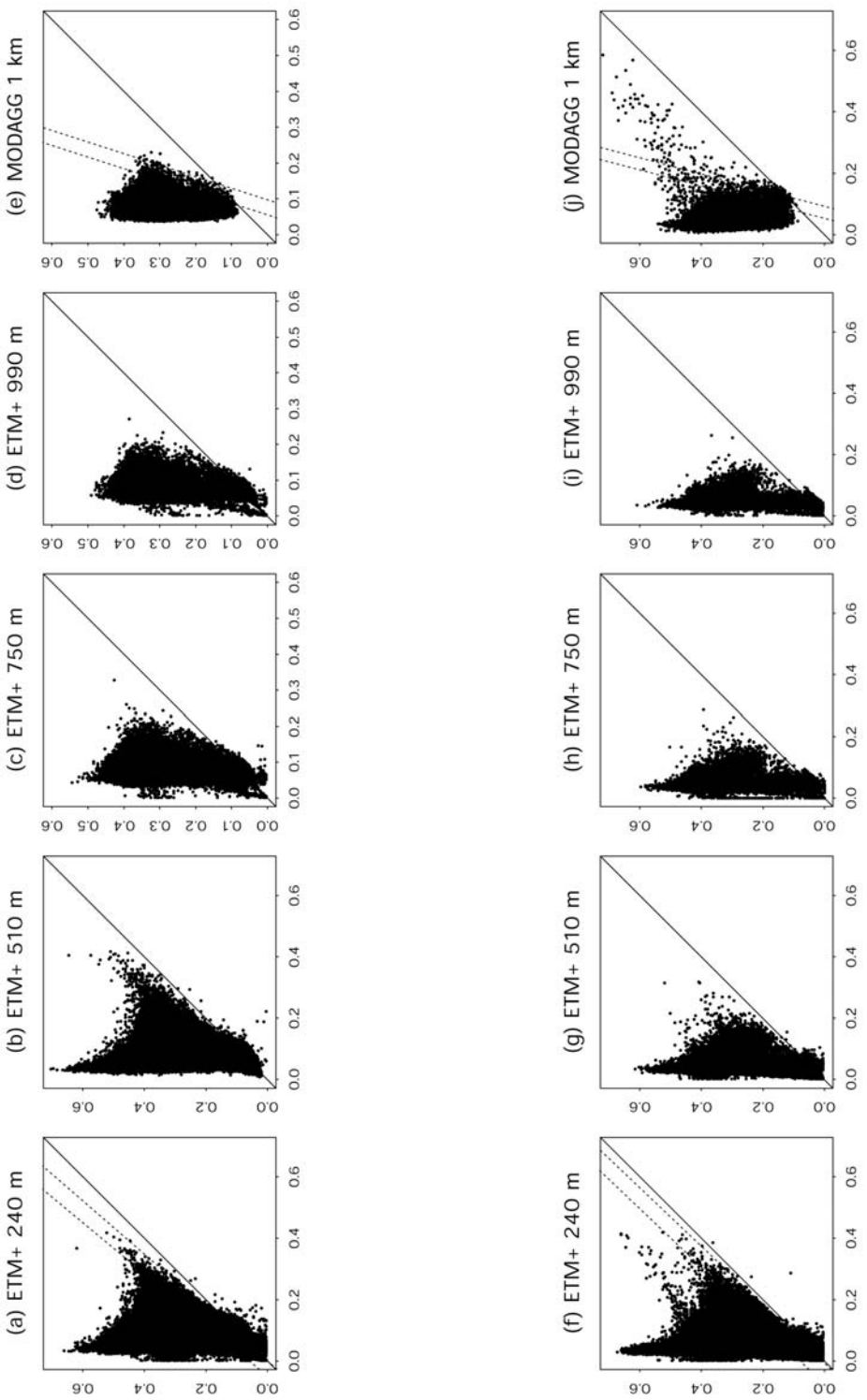

Figure 5-2 The scatterplot of the red (x) and near-infrared (y) reflectances for ETM+ and MODAGG imageries. The ETM+ scatterplots are of different resolutions (240m, 510m, 750m and 990m). The strip within the dashed lines shows the soil pixels.

The direct consequence of the red-NIR pixel mixing is that it makes soil line identification difficult to impossible. Without proper pixel unmixing, it is unrealistic to draw a soil line as in the high-resolution red-NIR space. For the current study, the coherent high-resolution ETM+ red-NIR space was used as an alternative, keeping in mind that the scaling of surface reflectance could be treated as linear. The soil and vegetation reflectances of a certain pixel were treated as invariable whatever the pixel's resolution. However, their fractions change relative to variable resolutions. According to this rationale, the soil reflectance index, and thus the soil reflectance derived from the ETM+ imagery (30 m), were used as inputs in the RT simulation process.

Note that the MODIS and ETM+ bands have different spectral response functions. To relate the ETM+ reflectance bands to the MODIS reflectance bands, statistical relations have been established based on extensive surface reflectance spectra of different cover types (Liang, 2001). These reflectance spectra were integrated with both MODIS and ETM+ sensor spectral response functions and a simple linear regression was then performed. For brevity, the empirical formulae (Liang et al., 2002a) to predict MODIS spectral band reflectance from ETM+ spectral band reflectance were not listed here. Once the soil reflectance index and the soil reflectance were determined from the coherent ETM+ imagery, the soil reflectance needed in MODIS simulation was calculated using these formulae.

Although not illustrated here, I did try to locate an empirical soil line from the MODAGG red and NIR reflectance scatterplot. The low-right strip pixels in the red-NIR

space were treated as soil pixels (within the dashed lines in Figure 5-2e&j). Obviously, this method will result in a soil line with a high slope and a very low intercept. It is very interesting to note that the final retrieved LAI values were not totally unrealistic using this empirical soil line. There are two possible reasons for this behavior. The first is that the soil reflectance may have a very insignificant effect on the total reflectance in the coarse resolution pixel. Because of pixel mixing, the soil element in a coarse pixel does not contribute as much reflectance to the mixed pixel as in the high-resolution imagery. Second, it is expected that soil lines will rotate and shift when spatial resolution changes. In this study, the soil line rotates counter-clockwise with the decreasing reflectance of the mixed pixels when the spatial resolution decreases (Figure 5-2). Those right-hand strips of pixels are not pure soil pixels any more—they simply have more 'soil' than other pixels. One can then determine the soil reflectance index directly from MODIS data in the future, even if its accuracy may be questionable. A better soil line can be obtained from the 250m MODIS Level 2 band 1 and 2 surface reflectance data. In principle, the *SRI* obtained in this way should be more realistic and practical for simulating canopy reflectance. This will be further explored in the future.

To the best of my knowledge, all current soil lines need to be determined manually. Research for this dissertation did not yield any published methods for automated soil line identification. In this and other similar studies, a semi-automated soil line identification method was attempted based on the pixels' red-NIR reflectance shape. More effort is needed in this direction.

5.2.4 Creating the database with the radiative transfer model

The MCRM model (Kuusk, 2001) simulates two-layer crop canopies based on the homogeneous model MSRM (Kuusk, 1994) and on the Markov chain reflectance model (Kuusk, 1995b). The MCRM was run with variable solar zenith angles (SZA: 20, 30, 35, 40, 45, 50, 55, 60), LAI (0.1~10 by 0.1) and different *SRI* values (0.01, 0.05, 0.1, 0.15, 0.2, 0.25, 0.3, 0.4, 0.5, 0.6, 0.8, 1.0). Please note that the *SRI* was derived from the soil line of the simultaneous ETM+ red-NIR space. The leaf orientation was assumed spherical. Other parameters were fixed with the same values as in section 4.2. All chlorophyll A + B (40, 50 ug/cm^2), the Markov parameter (0.8) and the leaf structure parameter (1.8) were fixed with the GA-optimized values in Chapter 3. These values were thought to be representative of the general conditions over the study site.

The time required to precompute the database is proportional to the number of spectral channels. The high spectral resolution (set to 5 nm) of the MCRM output was used initially. However, using such a high spectral resolution, integrating ETM+ spectral band response function becomes very time-consuming. Instead, the MCRM code was tuned so as to yield the reflectances at the ETM+ central wavelength only. Thus, the computation is much more efficient while attaining a comparable accuracy.

5.2.5 Nonparametric training and prediction

Both the neural network (NN) method and the projection pursuit regression (PPR) methods were briefly outlined in section 1.2.3. Once the simulated database is ready, these two non-parametric methods are applied to train the datasets and predict LAI from the remotely sensed data.

The training process is usually computationally intensive. Because some of the satellite bands are closely related, only those bands which have the most information are usually applied in the training iteration. Commonly used bands include green, red, NIR, and the NDVI, either as single bands or in combinations (Baret et al., 1995; Kimes et al., 2002; Qi et al., 2000; Smith, 1993). Obviously, different MODIS band combinations could be used to invert the LAI from the simulated database. In another similar study, different band combinations were tested to determine their effect on the final LAI accuracy estimated from EO1 ALI data (Liang et al., 2002b). In this study, only the MODIS red (band 1) and NIR (band 2) band were used in the training and the next prediction processes. This is similar to the strategy applied in the MODIS LAI algorithms. In addition, my previous tests have shown that use of the red and NIR can have an equivalent accuracy with relative computational simplicity compared with that using all bands.

As in other studies (Gong et al., 1999; Qi et al., 2000; Smith, 1993), the training process was carried out with the simulated database. However, training with only the simulated databases may not represent the real environment and can lead to anomalous results in the final LAI map. To overcome this problem, some real image pixels were added to the

database before training. The bare ground points are especially necessary because they have zero LAI (or at least very low) and are easily over fitted. Please note that I did not include LAI=0.0 in the simulation process in the above section. In this study, the nonvegetated pixels (bare soils, constructed areas, seashores, etc.) were extracted from MODIS surface reflectance data using NDVI (<0.3), and band 6 and 7 as the thresholds. Bare ground reflectances and LAI (=0.0) were added to the database in the training step to represent the true natural conditions.

Many statistical software producers provide NN and the PPR packages. Here, both were performed with the Splus package (Venables and Ripley, 1994). The same simulated database was used in both the PPR and NN training processes. The training process created an input-output relationship between reflectance and LAI. After training, the aggregated ETM+ and the MODAGG red (band 1) and NIR (band 2) reflectances were used to map LAI based on the trained input-output relationship.

5.3 Results

Figure 5-3 shows a color composite image of the LAI derived from the MODIS products, the aggregated ETM+ and the MODAGG in the Chesapeake Bay region. This figure also depicts the registration results between the aggregated ETM+ and the MODIS data. The ETM+ image is diamond-shaped and covers the center of the rectangle.

The MODIS LAI algorithm relies on the major biome information for its priori canopy physiological parameters (Knyazikhin et al., 1998a; Knyazikhin et al., 1998b). A biome type map (Figure 5-4) was obtained from the NASA EOS Data Gateway (EDG). These data were used to produce the MODIS standard LAI map (Figure 5-5). From its classification system, there are three major vegetation types in the map, broadleaf forest (50.3% of vegetation), broadleaf crops (26.9% of vegetation), and needleleaf forest (10.2% of vegetation). There are some grasses and cereal crops but they only occupy 3.5% of the vegetation. Except all these vegetation pixels, there are some shrubs and savanna pixels and unvegetated pixels.

MODIS and MODAGG LAI values are displayed in red and blue, respectively, within the rectangle. Figure 5-5 shows the MODIS standard LAI product retrieved from both the main (RT) method and the empirical backup method on May 1, 2001 and Aug 5, 2001. The MODIS LAI quality control (QC) mask was employed. In this figure, all water, barren, permanent wetlands/marshes, and built-up areas are filled with zero values. Moreover, all clouds and shadows were excluded in the subsequent comparison work. Table 5.1 compares the minimum, mean, and maximum LAI estimated by different approaches. LAI values derived from the main RT method and the empirical backup method were also compared in this table. The main RT method and the empirical produce nearly the same results (Table 5.1). At the beginning of the growing season (Figure 5-5a), most LAI values ranged between 5~6.9 (Table 5.1), with exceptions located on the east peninsula and in the northwest mountains (LAI: 2~4). In the middle of the growing season (Figure 5-5c), nearly all areas had a very large LAI (between

5~6.9, green in the figure). According to my field experience, these LAI values from both dates seem too large. In addition, there is not much difference (mean difference=0.2) between May 1 and Aug 5, 2001. I have also compared the specific LAI mean values for different biome types and for the two LAI retrieval algorithms. The MODIS LAI products were all found larger than the other MODAGG and ETM+ results.

Table 5.1 Statistics of the MODIS LAI products, LAI estimated from the aggregated ETM+ data and from the MODAGG data. The minimum (Min), mean and maximum (Max) values of the neural network (NN) and the projection pursuit regression (PPR) methods are shown for the two dates. The two mean values correspond to pixels with the main RT method and backup method, respectively.

		Apr 28, 2001			Aug 2, 2001		
		Min	Mean	Max	Min	Mean	Max
MODIS LAI*		0.2	5.6/5.6	6.9	0.6	6.0/6.0	6.9
ETM+ LAI	NN	0.1	1.9/1.9	8.2	0.1	2.6/2.6	8.6
	PPR	0.1	2.0/2.0	8	0.1	2.7/2.8	7.9
MODAGG	NN	0.1	1.9/1.9	5.1	0.1	2.8/2.9	8.9
LAI	PPR	0.1	2.1/2.1	5.1	0.1	3.0/3.1	8.3

* The MODIS LAI data were of May 1 and Aug 5, 2001 respectively.

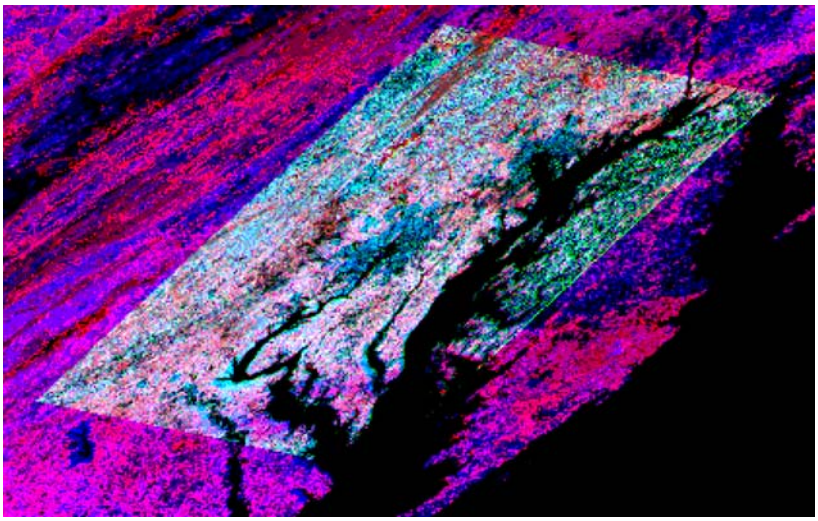

Figure 5-3 Presentation of the registration of the MODIS LAI product (red), the aggregated ETM+ LAI (green) and the MODAGG LAI (blue) of the study area. The ETM+ (the smaller lozenge region) and MODAGG data are of Aug 28, 2001. The MODIS LAI product is of May 1, 2001.

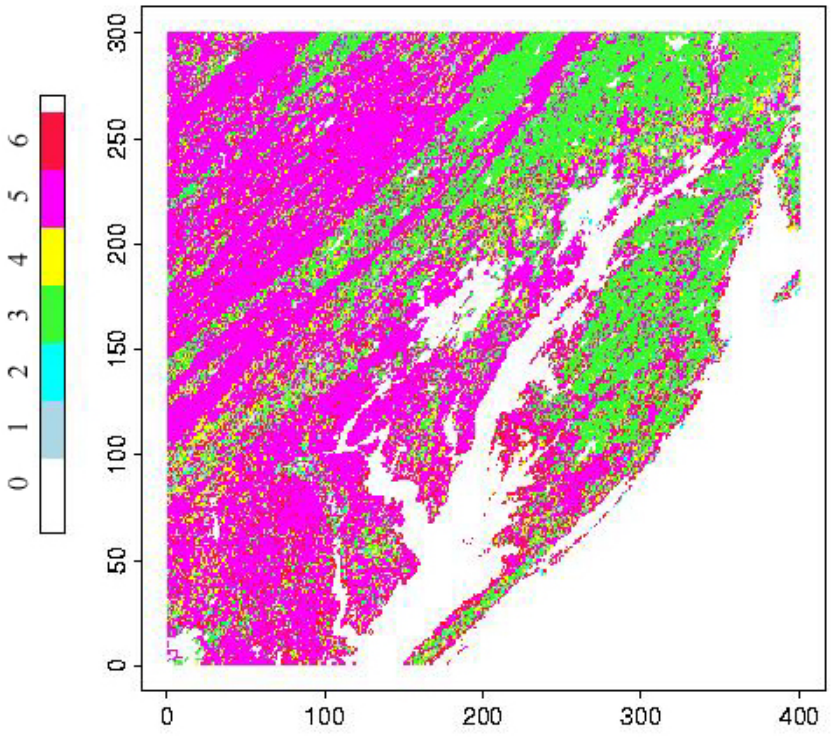

Figure 5-4 MODIS biome types for LAI products. Color numbers: 0, Water or unclassified; 1, Grasses/Cereal crops; 2, Shrubs; 3, Broadleaf crops; 4, Savannah; 5, Broadleaf forest; 6, Needleleaf forest.

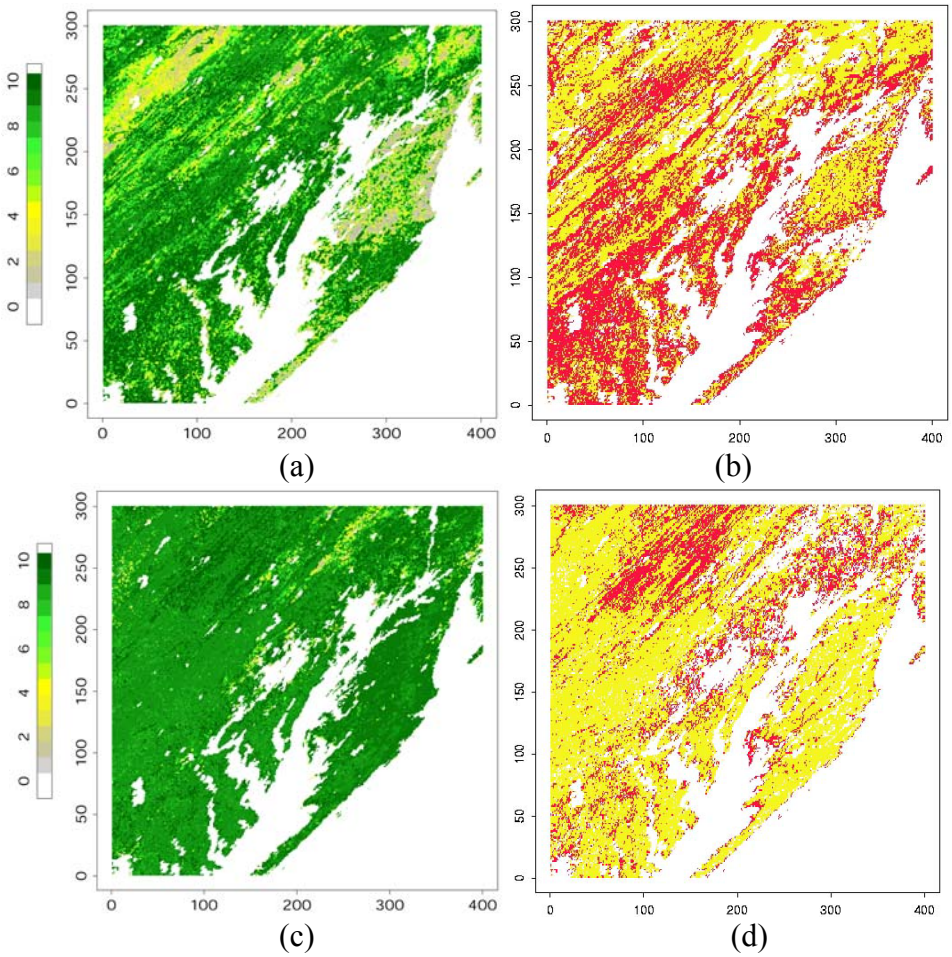

Figure 5-5 MODIS LAI products for (a) May 1, 2001 and (c) Aug 5, 2001. (b) and (d) depict the MODIS LAI algorithms for the two dates. Red (yellow) color represents that the main radiative transfer method (the empirical backup method) is used.

5.3.1 LAI maps from MODAGG

LAI maps for Apr 28 and Aug 2, 2001 were generated from MODAGG data using the neural network and the projection pursuit regression methods (Figure 5-6). The estimated LAI values ranged from 0.1 to 5.1 on Apr 28, and from 0.1 to 8.9 on Aug 2 with the NN method (zero values were masked). Their mean LAI values increased from 1.6 to 2.7. The PPR method produced very similar results as those of the NN approach, and both results agree well with each other spatially. The regional land cover maps (Hansen et al., 2000) show that those high LAI values correspond to broadleaf forests. Temporal dynamics of the forest LAI distribution are visually distinct in Figure 5-6. On Apr 28, most of the green patches were located in the central and southwest side of the image, while on Aug 2, the green patches shifted toward the northwest mountain areas.

5.3.2 LAI maps from aggregated ETM+

The LAI maps from the aggregated ETM+ imagery are shown in Figure 5-7 with a spatial resolution of 510m. The spatial pattern of the LAI map generated by the neural network (Figure 5-7a&c), is similar to that generated by the PPR approach (Figure 5-7b&d). The color gradient of the ETM+ LAI maps differs from that of the MODAGG results. More regions become greener from Apr 28 to Aug 2, which means

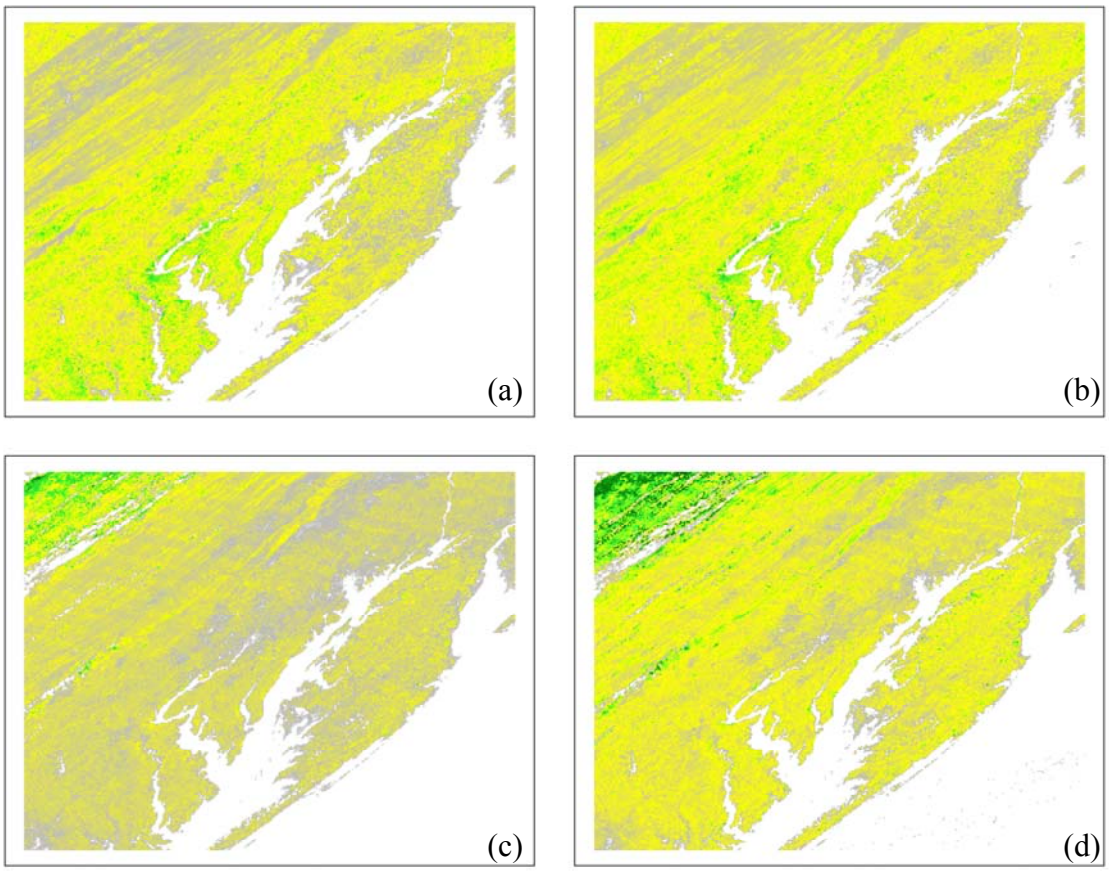

Figure 5-6 LAI estimated from MODAGG data (1 km). The top two are for Apr 28, 2001 and the bottom two Aug 2, 2001. (a) and (c) are from the neural network algorithm; (b) and (d) are with the projection pursuit regression method. LAI legend same as Figure 5-5.

that the LAI has increased. This trend is also shown statistically. Table 5.1 shows that the estimated mean LAI increased from 1.7 to 2.5 with the NN and from 1.8 to 2.6 with the PPR. The statistical results of Table 5.1 represent slightly different areas for ETM+ and MODAGG because of their different resolutions and spatial coverage. For example, the maximum LAI estimated from ETM+ (8.2/8 for NN/PPR) was larger than MODAGG (5.1/5.1). Nevertheless, the LAI statistics have followed reasonable temporal dynamics of the vegetation in the study area. Note that the SZA has a 5 degree difference between the ETM+ and MODIS images.

5.3.3 Comparison of LAI distributions

To further compare the results from this approach with those from the MODIS standard products, the histograms of the coherent MODIS LAI, ETM+ LAI and MODAGG LAI are compared in Figure 5-8. In this figure, the MODIS QC mask has been applied to exclude the filled values (≥249). A common mask was used to delineate the same geographic region for all three datasets. The MODAGG LAI (Figure 5-8G to J) agreed well with ETM+ LAI (Figure 5-8C to F). Their histograms closely resemble one another, although their absolute LAI values may differ. The NN and the PPR produce nearly identical results as shown by their LAI distributions. This suggests that the NN and PPR are two easy and operational techniques to estimate LAI from MODIS images. However, it is found that MODIS LAI products have significantly more

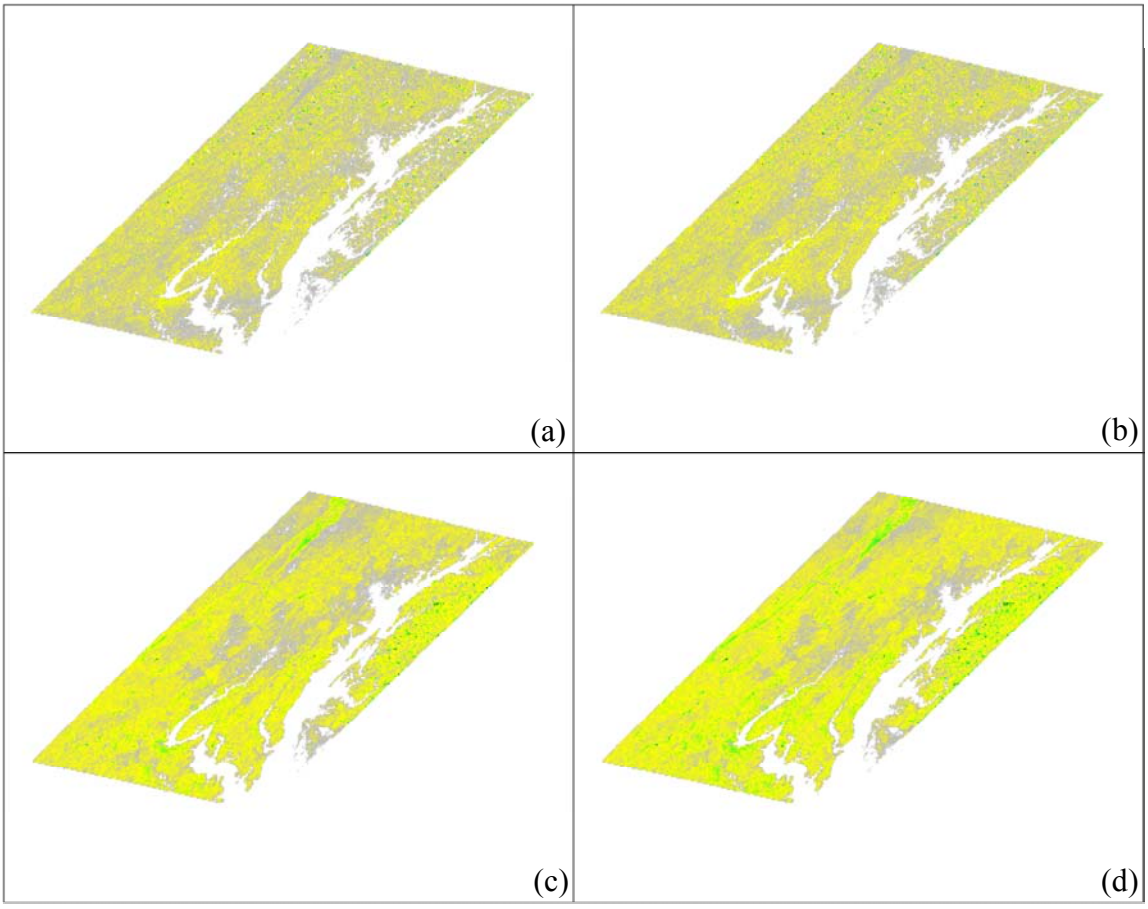

Figure 5-7 LAI estimated from aggregated ETM+ reflectance (510 m). The top two are for Aug 28, 2001 and the bottom two Aug 2, 2001. (a) and (c) are from the neural network algorithm; (b) and (d) are with the projection pursuit regression method. LAI legend same as Figure 5-5.

pixels peaked at the high end and less pixels in the middle range of LAI in comparison to the ETM+ and MODAGG LAI outputs. This led to very high MODIS LAI mean values (5.9 and 6.1 in Table 5.1) although their LAI ranges are reasonable in view of the field LAI. Extensive ground measurements demonstrate that typical LAI values in this study area are about 1.2~3.5 for corn, 2.5~5.5 for soybeans, 2.0~5.0 for grasses, and 2.1~3.6 for mixed forests. It is noted that there are several dense wheat fields having high LAI values (above 6.0). The LAI derived from ETM+ and MODAGG are representative of the mean and seasonal LAI characteristics over this study area. Some of the maximum ETM+ and MODAGG LAI are larger than 8.0, which are treated as outliers in this study. A close examination of these pixels is needed in the future to identify the causes.

5.4 Discussion and summary

In this chapter, two non-parametric regression methods, the neural network (NN) and the projection pursuit regression (PPR) were integrated with radiative transfer (RT) to estimate LAI from MODIS reflectances. To simplify the RT simulation process, a soil reflectance index (*SRI*) calculated from ETM+ image was used to compute the MODIS soil reflectance in the RT simulation process.

To compare the MODIS LAI products with ones from ETM+, the ETM+ reflectance was aggregated to 510m resolution and registered with the MODIS imagery. The NN and the PPR methods establish the relationships between the simulated canopy reflectance

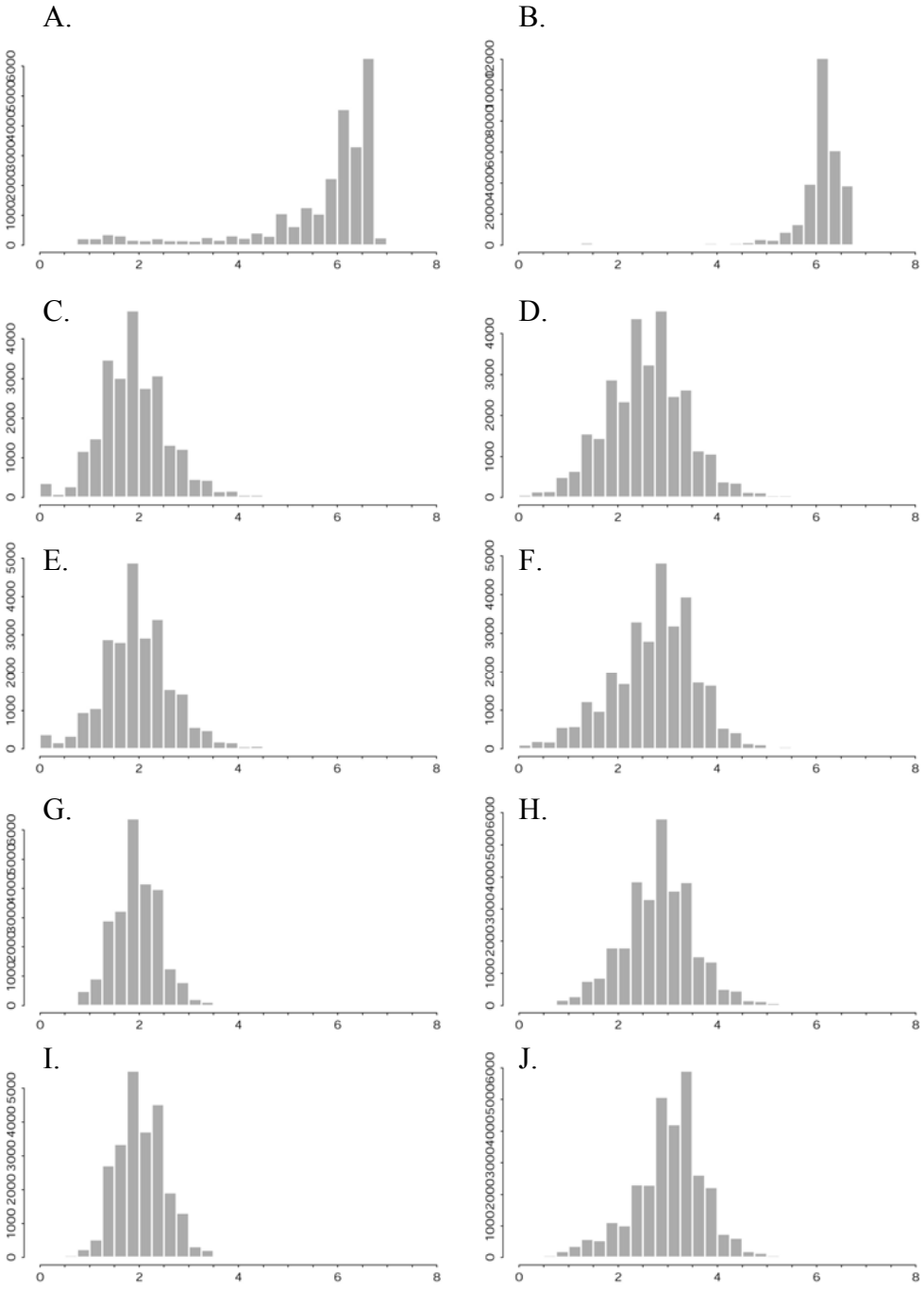

Figure 5-8 Histogram comparison of the MODIS LAI products and LAI derived from MODAGG and aggregated ETM+ data. The two columns represent the results of two dates (Apr 28 and Aug 2, 2001 respectively). (A-B) MODIS LAI products; (C-D) From ETM+ with NN method; (E-F) From ETM+ with PPR method; (G-H) From MODAGG with NN method; and (I-J) from MODAGG with PPR method.

and the biophysical parameters (LAI in this case). Applying the relationship to MODIS reflectance data, LAI is derived and compared with results from the aggregated ETM+ reflectance.

The same MODAGG data as used by the MODIS instrument LAI algorithm were used to produce LAI with the alternative approaches (NN and PPR). LAI maps generated with the MODAGG data were very similar to those using the aggregated ETM+ data. Seasonal dynamics of LAI are clearly illustrated in the two days. In the MODIS image, the LAI ranged between 0.2~6.9, which matches the ground-measured LAI values very well. However, the MODIS LAI mean values (around 6) were found to be larger than those from the other two datasets in the study area (Table 5.1). Because the initial work was based on two days for a specific location, general conclusions should be made only after further analysis at other sites.

The NN and PPR produced almost identical results. Therefore, the NN and PPR provide two practical approaches to estimate LAI from MODIS images. Experimental tests in the study area demonstrate that nonparametric algorithms can be used as an independent validation tool for the MODIS LAI product. One of the advantages of the nonparametric methods is that they do not require a priori biome information and image segmentation (Tian et al., 2002). Other information requirements, such as canopy structure, are the same as for the MODIS LAI algorithms. The only weakness is that the training process may be lengthy.

To gain improved understanding of the usefulness and limitations of non-parametric methods at other landscapes, especially in sparsely-vegetated sites, more extensive experiments are needed. One issue concerning the relating of remote sensing reflectance to LAI is saturation, problematic because canopy reflectances do not change with increasing LAI. The algorithm introduced in this chapter did not address this issue specifically. Field-measured LAI could be as high as 6 (or greater) in some dense wheat fields. The MODIS LAI algorithm quantifies these situations by introducing a solution-distribution function which can be used when this algorithm is extended to other sites.

Chapter 6 Conclusion

LAI defines the leaf area that interacts with solar radiation and is responsible for carbon exchange with the atmosphere. Over the past decades, remote sensing techniques have been widely applied to derive LAI (Plummer, 2000). The research presented in this dissertation investigated several new algorithms to improve the estimation of LAI from remote sensing data. When the images (e.g. ETM+ or MODIS) were partly hazy, the new atmospheric correction algorithm was very crucial to removing the haze and producing improved images for LAI estimation. A new genetic algorithm (GA) was explored and shown to be very effective in the optimization process of a radiative transfer (RT) model inversion. The preliminary GA results were used in the next hybrid LAI estimation process. The hybrid LAI algorithm successfully estimated LAI from both ETM+ and MODIS images. Clearly demonstrated was that surface reflectance provides better LAI estimation than the digital numbers or radiances of raw imagery. LAIs estimated with the hybrid method were validated in the study area and the results were very accurate. More detailed summaries on these topics are provided in the following sections.

6.1 A new atmospheric correction algorithm for ETM+

The purpose of atmospheric correction is to transform the remotely sensed data obtained at the top of the atmosphere into surface reflectance, and thus improve the biophysical parameter estimation. Some conventional atmospheric correction methods are useful for homogeneous atmospheric conditions under different types of assumptions (e.g.

existence of invariant objects or dark objects). However, they cannot effectively correct heterogeneous aerosols in general atmosphere and surface conditions.

A new atmospheric correction algorithm was presented to retrieve surface reflectance from Landsat 7 ETM+ imagery. The basic idea was to identify surface clusters using the infrared bands (band 4, 5 and 7 for ETM+) less contaminated by aerosols. This new algorithm avoids the preconditions required by existing algorithms. The most characteristic parts of this algorithm are to account for heterogeneous aerosol scattering effects in a scene and to correct the surface adjacency effects using a simple analytical formula. Therefore, it is useful for general atmospheric and surface conditions.

Validation with simultaneous surface measurements indicated that this new algorithm produced very accurate results with relative differences less than 10%. This algorithm was extended to correct AVIRIS, MODIS and SeaWiFS imagery, all having different spectral and spatial characteristics from ETM+ imagery. For other sensors with hyperspectral and multi-angular viewing capabilities, investigations are needed to test the validity of the algorithm. Future study will focus on correcting multitemporal images.

6.2 Application of genetic algorithm in the optimization of RT model inversion

LAI estimation through the inversion of a radiative transfer model is a common practice in remote sensing application. The objective here was to minimize the merit function.

Currently, there are several methods (such as the downhill simplex method and the conjugate direction method) used in the minimization process. However, these methods are very complicated for parameter inversion. Some models may have multiple solutions and some cost functions may not converge. A new optimization approach—genetic algorithm (GA)—was proposed in this dissertation to optimize the merit function in the RT inversion process. With the GA optimization method, it only needs to run the forward RT simulation process. In addition, the genetic algorithm will automatically scan all ranges of the initial variables.

Different from current RT inversion algorithms, GA optimization was performed with randomly generated values for land surface parameters. A goodness-of-fit was calculated and was used to make adjustments in RT model parameters to find the best sets of parameters. In this study, six free parameters (LAI, Markov parameter, Chlorophyll A&B concentration, leaf structure parameter, and two soil parameters) were considered in the initial retrieval. Reducing the number of genes could improve the inversion's accuracy. The combination of both red and near-IR bands produced results as good as when using six ETM+ bands, while significantly reducing the computation. The best results were obtained with three genes (LAI, and two soil parameters) from ETM+ red and NIR bands (R^2=0.776, RMSE=1.064). The NIR band alone can be used to get a reasonablly good LAI estimation, but the red band cannot be used individually. The GA results were compared with the Powell minimization algorithm. The difference between these two algorithms was very small for lower LAI (<3), and increased when LAI>3.

In this study, the GA optimization model and RT model were integrated through an exchange of both input and output data files between the two models. The GA optimization process was still computationally intensive although reducing the number of free parameters helped. To solve this problem, more efficient GA optimization algorithms and GA-RT coupling methods are necessary. The computation time must be radically reduced before this method can be extended for regional LAI mapping.

6.3 LAI retrieval with a hybrid method from ETM+

Both statistical methods and physically based RT methods have been used for LAI inversion. Statistically methods are mainly based on vegetation indices. They are simple to use, but there is no universal formula for different vegetation types and thus it is difficult for large-scale application. Although physically based and more accurate, the RT methods are very complicated for parameter retrieval. Non-parametric statistically methods, mainly the neural network and projection pursuit regression algorithms, have provided an efficient tool to relate the biophysical variables of interest to the simulated reflectances.

I have proposed a new hybrid method to combine the advantages of both RT simulation and non-parametric retrieval methods and to estimate LAI from multispectral remote sensing data. The NN algorithms were integrated with RT and were used to retrieve LAI from both ETM+ surface reflectance (database 1) and TOA radiance data (database 2). Database 1 was constructed with a canopy RT model and database 2 with the combined

atmospheric and canopy RT models. A soil reflectance index, derived from the soil line, was proposed to account for the soil background reflectance.

LAI was successfully estimated with the new hybrid approach from both surface reflectance and TOA radiance. The outputs were compared with field-measured LAI datasets from four different dates. The best results were found with the combination of red and NIR bands of the surface reflectances (R^2=0.801 and RMSE=0.811). If the TOA radiances were used, the results were not so good (R^2=0.74, RMSE=1.17). In general, red and NIR bands are recommended for estimating LAI from ETM+ surface reflectances, while NIR and NDVI are recommended if TOA radiances are used. The sensitivity test showed that this approach was very robust, especially when surface reflectance was used. With this method, LAI derived from the high-resolution ETM+ image could be used to validate LAI products from some low-resolution sensors (e.g. MODIS, MISR and POLDER).

6.4 LAI retrieval from MODIS data with a hybrid approach

Presently, the MODIS team estimates LAI with the look-up table (LUT) method. The LUT method speeds the inversion process significantly, but its accuracy still depends on the input variables and RT models. The new hybrid approach developed for ETM+ was thus extended to estimate LAI from MODIS data. Besides NN, another non-parametric method, the projection pursuit regression (PPR) method, was also integrated with the RT

method. To simplify the RT simulation process, a soil reflectance index calculated from the coherent ETM+ image was used to calculate the MODIS soil reflectance.

For comparison with MODIS standard LAI products, the ETM+ reflectance was aggregated to 510m resolution and registered with the MODIS imagery. In the first step, the simulated canopy reflectance and the biophysical parameters trained the NN and PPR. Applying the trained results to MODIS reflectance data, LAI was derived and validated with results from the aggregated ETM+ reflectance data.

The MODIS aggregated data (MODAGG) were used to produce LAI with the hybrid approach (both NN and PPR). LAI maps generated from the MODAGG data were similar to those from the aggregated ETM+ data. Seasonal dynamics of LAI were clearly illustrated in the two tested dates. In the MODIS land products, the LAI ranged between 0.2~6.9, which matches the ground LAI ranges. However, the MODIS LAI mean values (around 6) were larger than results from both ETM+ and MODAGG. The final conclusion will be made after more work is done.

The NN and PPR had nearly identical results. Because the simulated databases have already taken into account various canopy/leaf and environment parameters, the non-parametric multiple regression has the advantage to abridge the number of input variables needed in the MODIS LAI algorithms.

Table 6.1 Comparison of the GA optimization methods, the hybrid approach the MODIS LAI algorithm.

	GA method	Hybrid approach	MODIS LAI algorithm
A priori information requirement	Low	Medium	Medium
Computational demands	High	Low	Medium
Accuracy over the study area	Medium	High	Low

6.5 Algorithm comparison

Table 6.1 compares the input information requirement, computational demands and accuracy of the GA method, the hybrid approach and the MODIS LAI algorithms.
As to the input information requirement, the genetic optimization algorithm needs a few input data. During the optimization process, the GA will determine the optimal value for each free parameter. The hybrid approach needs to fix some variables in the simulation process, because uncertainties will be caused by too many free variables. The MODIS LAI algorithm also needs some a priori information such as the biome type and the soil background information.

The computational demands for both the hybrid approach and the MODIS LAI algorithm lie in the RT simulation process. Once the databases are ready, the prediction process is straightforward. The GA does not need any complicated RT simulation, but the current optimization strategy is computer intensive. This also limits its practical application.

In the study area, the highest accuracy is obtained with the hybrid LAI estimation approach (R^2=0.801 and RMSE=0.811 for ETM+). The GA also works very well (R^2=0.776, RMSE=1.064 for ETM+). From the results in this chapter, it is obvious that the MODIS LAI product overestimated the LAI in the study area.

6.6 Issues for further research

In the hybrid LAI estimation approach, the soil line was determined from the whole image, but it should be instructive to look into different soil lines at different parts of the image when landscapes are very heterogeneous. Further, I have mostly considered nadir-view images in this study. In multiple viewing angles (MVA) simulations, the soil reflectance is very crucial, and the significance of the *SRI* needs further evaluation. However, MVA provide the capability of viewing the same ground are from different directions and may improve the retrieval accuracy of land surface parameters. Therefore, it is worthwhile to extend the hybrid approach to MVA observations.

One issue of relating remote sensing reflectance to LAI is the saturation problem, or, in other words, the canopy reflectance will not change with increasing LAI. The MODIS LAI algorithms quantify these situations by introducing a solution distribution function for the saturation domain. This approach can also be used in minimizing the saturation effect when this algorithm is extended to other sites.

This study area in this dissertation is a middle-latitude temperate agricultural site. For general application, it is necessary to test the hybrid approach for other vegetation types. Currently, the new method is tested for boreal forests in Canada and semi-arid rangeland in Arizona. My preliminary results show that the hybrid approach works reasonably well over these areas.

The LAI product will ultimately be used for different ecological and other land surface process models. One attractive application field is with the crop growth models for crop yield estimation. LAI and other biophysical parameters derived from remotely sensed data can meet the needs of crop models for crop monitoring and prediction. Crop models simulate LAI for a whole growing season, while the remotely sensed LAI product are just snapshots. LAI estimated from remote sensing observations can be used to tune the environmental parameters used in the crop model and thus improve the crop yield estimation. Assimilation of LAI to crop models is currently underway.

REFERENCES

Abuelgasim, A. A., S. Gopal and A. H. Strahler, 1998. Forward and inverse modelling of canopy directional reflectance using a neural network. *International Journal of Remote Sensing*, **19**(3): 453-471.

Ahlrichs, J. S. and M. E. Bauer, 1983. Relation of agronomic and multispectral reflectance characteristics of spring wheat canopies. *Agronomy Journal*, **75**: 987-993.

Analytical Spectral Devices (ASD), I., 2000. *FieldSpec Pro User's Guide*. Boulder, Colorado. pp. 85

Antyufeev, V. S. and A. L. Marshak, 1990. Inversion of Monte Carlo model for estimating vegetation canopy parameters. *Remote Sensing of Environment*, **33**(3): 201-209.

Asrar, G., M. Fuchs, E. Kanemasu and J. Hatfield, 1984. Estimating absorbed photosyntheic radiation and leaf area index from spectral reflectance in wheat. *Agronomy Journal*, **76**: 300-306.

Asrar, G., E. T. Kanemasu, R. D. Jackson and P. J. J. Pinter, 1985a. Estimation of total above-ground phytomass production using remotely sensed data. *Remote Sensing of Environment*, **17**: 211-220.

Asrar, G., E. T. Kanemasu and M. Yoshida, 1985b. Estimates of leaf area index from spectral reflectance of wheat under different cultural practices and solar angle. *Remote Sensing of Environment*, **17**: 1-11.

Asrar, G., B. J. Myneni and B. J. Choudhury, 1992. Spatial heterogeneity in vegetation canopies and remote sensing of absorbed photosyntheticaly active radiation: A modeling study. *Remote Sensing of Environment*, **41**: 85-103.

Baret, F., 1995. *Use of spectral reflectance variation to retrieve canopy biophysical characteristics*. In M. Darson and S. Plummer (Eds.), Advances in Environmental Remote Sensing (pp. 33-51). John Wiley and Sons, Inc.

Baret, F., J. Clevers and M. Steven, 1995. The robustness of canopy gap fraction estimates from red and near-infrared reflectances: a comparison of approaches. *Remote Sensing of Environment*, **54**: 141-151.

Baret, F. and T. Fourty, 1997. Estimation of leaf water content and specific leaf weight from reflectance and transmittance measurements. *Agronomie*, **17**: 455-464.

Baret, F. and G. Guyot, 1991. Potential and limits of vegetation indices for LAI and APAR assessment. *Remote Sensing of Environment*, **35**: 161-173.

Baret, F., G. Guyot and D. Major, 1989. TSAVI: a vegetation index which minimizes soil brightness effects on LAI and APAR estimation. *12th Canadian Symp. on Remote Sensing and IGRASS'90.*, Vancouver, Canada.

Baret, F., S. Jacquemoud and J. F. Hanocq, 1993. The Soil Line Concept in Remote Sensing. *Remote Sensing Reviews*, **7**: 65-82.

Barker, J. L., B. L. Markham and J. Burelbach, 1992. *MODIS image simulation from Landsat TM imagery*. In ASPRS/ACSM/RT 92 technical paper, 1 (pp. 156–165).

Berk, A., G. P. Anderson, P. K. Acharya, J. H. Chetwynd, L. S. Bernstein, E. P. Shettle, M. W. Matthew and S. M. Adler-Golden, 1999. *MODTRAN4 users manual*, Hanscom AFB, MA, Air Force Research Laboratory.

Best, R. G. and J. C. Harlan, 1985. Spectral estimation of green leaf area index of oats. *Remote Sensing of Environment*, **17**: 27-36.

Bicheron, P. and M. Leroy, 1999. A method of biophysical parameter retrieval at global scale by inversion of a vegetation reflectance model. *Remote Sensing of Environment*, **67**: 251-266.

Bonan, G. B., 1993. Importance of leaf area index and forest type when estimating photosynthesis in boreal forests. *Remote Sensing of Environment*, **43**: 303-314.

Boreal, C. C., S. A. W. Gerstl and B. J. Powers, 1991. The radiosity method in optical remote sensing of structured 3-D surfaces. *Remote Sensing of Environment*, **36**: 13-44.

Borel, C. C. and S. A. W. Gerstl, 1992. Adjacency-blurring-effect of scenes modeled by the radiosity method. *Proceedings of the SPIE*, **1688**: 620-624.

Botkin, D. B., 1986. *Remote Sensing of the Bioshpere.*, Washington, D.C., USA, National Academy of Sciences, Report of the Committee on Planetary Biology.

Broge, N. H. and E. Leblanc, 2001. Comparing prediction power and stability of broadband and hyperspectral vegetation indices for estimation of green leaf area index and canopy chlorophyll density. *Remote Sensing of Environment*, **76**(2): 156-172.

Burgess, D. W. and D. Pairman, 1997. Bidirectional reflectance effects in NOAA AVHRR data. *International Journal of Remote Sensing*, **18**: 2815-2825.

Cahalan, R. F., L. Oreopoulos, G. We, A.Marshak, S. C. Tsay and T. DeFelice, 2001. Cloud characterization and clear-sky correction from Landsat-7. *Remote Sensing of Environment*, **78**(1-2): 83-98.

CEOS/WMO, Dec, 2001. *Satellite systems and requirements (The official CEOS/WMO online database)*.

Chance, J. E., 1981. Crop identification and leaf area index calculation with Landsat multispectral data. *International Journal of Remote Sensing*, **2**: 1-14.

Chavez, J. P. S., 1988. An improved dark-object subtraction technique for atmospheric scattering correction of multispectral data. *Remote Sensing of Environment*, **24**: 459-479.

Chavez, J. P. S., 1996. Image-based atmospheric corrections - revisited and improved. *Photogrammetric Engineering and Remote Sensing*, **62**(9): 1025-1036.

Chen, J., X. Li, T. Nilson and A. Strahler, 2000. Recent advances in geometrical optical modelling and its applications. *Remote Sensing Reviews*, **18**: 227-262.

Chen, J. M., 1996a. Evaluation of vegetation indices and a modified simple ratio for boreal applications. *Canadian Journal of Remote Sensing*, **22**: 229-242.

Chen, J. M., 1996b. Optically-based methods for measuring seasonal variation of leaf area index in boreal conifer stands. *Agricultural and Forest Meteorology*, **80**: 135-163.

Chen, J. M. and T. A. Balck, 1991. Measuring leaf area index of plant canopies with branch architecture. *Agricultural and Forest Meteorology*, **57**: 1-12.

Chen, J. M. and J. Cihlar, 1995. Plant canopy gap-size analysis theory for improving optical measurements of leaf-area index. *Applied Optics*, **34**: 6211-6222.

Cihlar, J., A. S. Denning and J. Gosz, 2000. *Global terrestrial carbon observation: requirements, present status, and next steps*. Report of a Synthesis Workshop, Ottawa, Canada.

Clark, C. and A. Cañas, 1995. Spectral identification by artifical neural network and genetic algorithm. *International Journal of Remote Sensing*, **16**(12): 2255-2275.

Clevers, J., 1989. The application of a weighted infra-read vegtation index for estimating leaf area index by correcting for soil moisture. *Remote Sensing of Environment*, **29**: 25-37.

Cohen, W. B. and C. O. Justice, 1999. Validation MODIS terrestrial ecology products: linking *in situ* and satellite measurements. *Remote Sensing of Environment*, **70**: 1-3.

Coulson, K. L., E. L. Gray and G. M. B. Bouricius, 1966. Effect of surface reflection on planetary albedo. *Icarus*, **5**: 139-148.

Curran, P. J., 1983. Multispectral remote sensing for the estimation of green leaf area index. *Philosophical Transactions of Royal Society, London, Series A*, **309**: 257-270.

Daughtry, C. S., 2001. Discriminating crop residues from soil by shortware infrared reflectance. *Agronomy Journal*, **93**(1): 125-131.

Daughtry, C. S. T., M. E. Bauer, D. W. Crecellius and M. M. Hixson, 1980. Effects of management practices on reflectance of spring wheat canopies. *Agronomy Journal*, **72**: 1055-1060.

Davis, L., 1991. *Handbook of Genetic Algorithms*. New York, Van Nostrand Reinhold. pp.

de Wit, A. J. W., 1999. *The Application of a Genetic Algorithm for Crop Model Steering using NOAA-AVHRR Data*. Feb 01, 2001. **1999**.

Deblonde, G., M. Penner and A. Royer, 1994. Measuring leaf area index with the LI-COR LAI-2000 in pine stands. *Ecology*, **75**: 1507-1511.

Deering, D. W., 1989. *Field measurements of bidirectional reflectance*. In G. Asrar (Ed.) Theory and Applications of Optical Remote Sensing (pp. 14-65). New York, John Wiley and Sons, Inc.

Denison, R. F. and R. Russotti, 1997. Field estimates of green leaf area index using laser-induced chlorophyll fluorescence. *Field Crops Research*, **52**(1-2): 143-149.

Diner, D. J., J. V. Martonchik, C. Borel, S. A. W. Gerstl, H. R. Gordon, Y. Knyazikhin, R. Myneni, B. Pinty and M. M. Verstraete, 1999. *Multi-angle Imaging Spectro-Radiometer (MISR) Level 2 Surface Retrieval (MISR-10) Algorithm Theoretical Basis Document*, Jet Propulsion Laboratory, California Institute of Technology.

Dozier, J. and J. Frew, 1981. Atmospheric corrections to satellite radiometric data over rugged terrain. *Remote Sensing of Environment*, **11**: 191-205.

Elvidge, C. D. and R. J. P. Lyon, 1985. Influence of rock-soil spectral variation on assessment of green biomass. *Remote Sensing of Environment*, **17**: 265-279.

Fassnacht, K. S., E. V. Nordheim, T. M. Liliesand, S. T. Gower and M. D. MacKenzie, 1997. Estimating the leaf area index of North Central Wisconsin forests using the landsat thematic mapper. *Remote Sensing of Environment*, **61**(2): 229-245.

Fraser, R. S. and Y. J. Kaufman, 1985. The Relative Importance of Scattering and Absorption in Remote Sensing. *IEEE Transaction of Geoscience and Remote Sensing*, **23**: 699-708.

Friedman, J. and W. Stuetzle, 1981. Projection-pursuit regression. *Journal of the American Statistical Association*, **76**: 183-192.

Gao, W. and B. M. Lesht, 1997. Model inversion of satellite-measured reflectance for obtaining surface biophysical and bidirectional reflectance characteristics of grassland. *Remote Sensing of Environment*, **59**: 461-471.

Gholz, H. L., 1982. Environmental limits on aboveground net primary production, leaf area, and biomass in vegetation zones of the Pacific Northwest. *Ecology*, **63**: 469-481.

Goel, N. S., 1988. Models of Vegetation Canopy Reflectance and Their Use in Estimation of Biophysical Parameters from Reflectance Data. *Remote Sensing Review*, **4**: 1-222.

Goel, N. S. and A. Kuusk, 1992. Evaluation of one-dimensional analytical model for vegetation canopies. *12th International Geoscience and Remote Sensing Symposium*, Houston.

Goel, N. S., I. Rozehnal and R. I. Thompson, 1991. A computer graphics based model for scattering from objects of arbitrary shapes in the optical region. *Remote Sensing of Environment*, **36**: 73-104.

Goel, N. S. and R. L. Thompson, 2000. A snapshot of canopy reflectance models and a universal model for the radiation regime. *Remote Sensing Reviews*, **18**: 197-225.

Goldberg, D. E., 1989. *Genetic algorithms in search, optimization and machine learning.* Reading, MA, Addison-Wesley. pp.

Gong, P., S. X. Wang and S. Liang, 1999. Inverting a canopy reflectance model using a neural network. *International Journal of Remote Sensing*, **20**(1): 111-122.

Govaerts, Y. M. and M. M. Verstraete, 1998. Raytran: A Monte Carlo ray tracing model to compute light scattering in three-dimensional heterogeneous media. *IEEE Transactions on Geoscience and Remote Sensing*, **36**: 493-505.

Gower, S. T., K. A. Vogt and C. C. Grier, 1992. Carbon dynamics of Rocky Mountain Douglas-fir: influence of water and nutrient availability. *Ecological Monographs*, **62**: 43-65.

Green, R. O., M. L. Eastwood, C. M. Sarture, T. G. Chrien, M. Aronsson, B. J. Chippendale, J. A. Faust, B. E. Pavri, C. J. Chovit, M. Solis, M. R. Olah and O. Williams, 1998. Imaging spectroscopy and the Airborne Visible/Infrared Imaging Spectrometer (AVIRIS). *Remote Sensing of Environment*, **65**: 227-248.

Grefenstette, J., 1990. *A User's Guide to GENESIS*.

Grier, C. C. and S. W. Running, 1977. Leaf area of mature Northwestern coniferous forests: relation to site water balance. *Ecology*, **58**: 893-899.

Hansen, M., R. DeFries, J. R. G. Townshend and R. Sohlberg, 2000. Global land cover classification at 1km resolutioin using a decision tree classifier. *International Journal of Remote Sensing*, **21**: 1331-1365.

Holben, B. N., 1986. Characteristics of maximum-value composite images for temporal AVHRR data. *International Journal of Remote Sensing*, **7**: 1435-1445.

Holben, B. N. and C. O. Justice, 1980. The topographic effect on spectral response from nadir-pointing sensors. *Photogrammetric Engineering and Remote Sensing*, **46**: 1191.

Holm, R. G., M. S. Moran, R. D. Jackson, P. N. Slater, B. Yuan and S. F. Biggar, 1989. Surface reflectance factor retrieval from Thematic Mapper data. *Remote Sensing of Environment*, **27**: 47-57.

Huete, A. R., 1988. A soil-adjusted vegetation index (SAVI). *Remote Sensing of Environment*, **25**: 295-309.

Huete, A. R., 1989. *Soil influences in remotely sensed vegetation-canopy spectra.* In G. Asrar (Ed.) Theory and Applications of Optical Remote Sensing (pp. 107-141). John Wiley and Sons, Inc.

Huete, A. R., R. D. Jackson and D. F. Post, 1985. Spectral response of a plant canopy with different soil backgrounds. *Remote Sensing of Environment*, **17**: 37-53.

Huete, A. R., D. F. Post and R. D. Jackson, 1984. Soil spectral effects on 4-space vegetation discrimination. *Remote Sensing of Environment*, **15**: 155-165.

Jacquemoud, S., 1993. Inversion of the PROSPECT+SAIL canopy reflectance models from AVIRIS equivalent spectra: theoretical study. *Remote Sensing of Environment*, **44**: 281-292.

Jacquemoud, S., F. Baret and J. F. Hanocq, 1992. Modeling spectral and bidirectional soil reflectance. *Remote Sensing of Environment*, **41**(2-3): 123-132.

Jacquemoud, S., S. L. Ustin, J. Verdebout, G. Schmuck, G. Andreoli and B. Hosgood, 1996. Estimating leaf biochemistry using the PROSPECT leaf optical properties model. *Remote Sensing of Environment*, **56**: 194-202.

Jarvis, P. G. and J. W. Leverenz, 1983. *Productivity of temperate, deciduous and evergreen forests*. In O. L. Lange, P. S. Nobel, C. B. Osmond and H. Ziegler (Eds.), Physiological Plant Ecology IV. (Encyclopedia of Plant Physiology, NS, vol 12D) (pp. 233-280). Berlin Heidelberg, Springer.

Jasinski, M. F., 1990. Sensitivity of the normalized difference vegetation index to subpixel canopy cover, soil albedo, and pixel scale. *Remote Sensing of Environment*, **32**(3-3): 169-187.

Jin, Y. and C. Liu, 1997. Biomass retrieval from high dimensional active/passive remote data by using artificial neural networks. *International Journal of Remote Sensing*, **18**: 971-979.

Jin, Y. and Y. Wang, 2001. A genetic alogorithm to simulateously retrieve land surface roughness and soil wetness. *International Journal of Remote Sensing*, **22**(16): 3093-3099.

Jordan, C. F., 1969. Deviation of leaf-area index from quality of light on the forest floor. *Ecology*, **50**: 663-666.

Jupp, D. L. B., J. Walker and L. K. Penridge, 1986. Interpretation of vegetation structure in Landsat MSS Imagery: a case study in distributed semi-arid Eucalypt Woodland. Part 2. Model based analysis. *Journal of Environmental Management*, **23**: 35-57.

Justice, C., D. Starr, D. Wickland, J. Privette and T. Suttles, 1998a. EOS land validation coordination: An update. *Earth Observer*, **10**(3): 55-60.

Justice, C. O., J. R. G. Townshend, E. F. Vermote, E. Masuoka, R. E. Wolfe, N. Saleous, D. P. Roy and J. T. Morisette, 2002. An overview of MODIS Land data processing and product status. *Remote Sensing of Environment*, **83**(1-2): 3-15.

Justice, C. O., E. Vermote, J. R. G. Townshend, R. Defries, D. P. Roy, D. K. Hall, V. V. Salomonson, J. L. Privette, G. Riggs, A. Strahler, W. Lucht, R. B. Myneni, Y. Knyazikhin, S. W. Running, R. R. Nemani, Z. Wan, A. R. Huete and W. van Leeuwen, 1998b. The Moderate Resolution Imaging Spectroradiometer (MODIS): land remote sensing for global change research. *IEEE Transactions on Geoscience and Remote Sensing*, **36**: 1228 -1249.

Justice, C. O., S. W. Wharton and B. N. Holben, 1981. Application of digital terrain data to quantify and reduce the topographic effect on Landsat data. *International Journal of Remote Sensing*, **2**: 213-230.

Kaufman, Y. J., 1987. The effect of subpixel clouds on remote sensing. *International Journal of Remote Sensing*, **8**: 839-857.

Kaufman, Y. J., 1989. *The atmospheric effect on remote sensing and its correction*. In G. Asrar (Ed.) Theory and Applications of Optical Remote Sensing (pp. 336-428). New York, John Wiley & Sons.

Kaufman, Y. J. and C. Sendra, 1988. Automatic atmospheric correction. *International Journal of Remote Sensing*, **9**: 1357-1381.

Kaufman, Y. J. and D. Tanré, 1992. Atmospherically Resistant Vegetation Index (ARVI) for EOS-MODIS. *IEEE Transaction of Geoscience and Remote Sensing*, **30**: 261-270.

Kaufman, Y. J. and D. Tanré, 1996. Strategy for direct and indirect methods for correcting the aerosol effect on remote sensing: from AVHRR to EOS-MODIS. *Remote Sensing of Environment*, **55**: 65-79.

Kimes, D., J. Gastellu-Etchegorry and P. Estève, 2002. Recovery of forest canopy characteristics through inversion of a complex 3D model. *Remote Sensing of Environment*, **79**: 320-328.

Kimes, D. S., Y. Knyazikhin, J. L. Privette, A. A. Abuelgasim and F. Gao, 2000. Inversion methods for physically-based models. *Remote Sensing Review*, **18**: 381-440.

King, M. D., Ed. 1999. *EOS Science Plan, The State of Science in the EOS Program*. National Aeronautics and Space Administration. pp.

Knyazikhin, Y., J. Glassy, J. L. Privette, Y. Tian, A. Lotsch, Y. Zhang, Y. Wang, J. T. Morisette, P. Votava, R. B. Myneni, R. R. Nemani and S. W. Running, 1999. *MODIS Leaf Area Index (LAI) and Fraction of Photosynthetically Active Radiation Asborved by Vegetation (FPAR) Product (MOD15) Algorithm Theoretical Basis Document*.

Knyazikhin, Y., J. V. Martonchik, D. J. Diner, R. B. Myneni, M. Verstraete, B. Pinty and N. Gobron, 1998a. Estimation of vegetation canopy leaf area index and fraction of absorbed photosynthetically active radiation from MISR data. *Journal of Geophysical Research*, **103**: 32,239-32,256.

Knyazikhin, Y., J. V. Martonchik, R. B. Myneni, D. J. Dine and S. W. Running, 1998b. Synergistic algorithm for estimating vegetation canopy leaf area index and fraction of absorbed photosynthetically active radiation from MODIS and MISR data. *Journal of Geophysical Research*, **103**: 32,257-32,276.

Koepke, P. and K. T. Kriebel, 1978. Influence of measured reflection properties of vegetated surfaces on atmospheric radiance and its polarization. *Applied Optics*, **17**: 260-264.

Kucharik, C. J., J. M. Norman and S. T. Gower, 1998. Measurements of branch area and adjusting leaf area index indirect measurements. *Agricultural and Forest Meteorology*, **91**: 69-88.

Kuusk, A., 1991. The determination of vegetation canopy parameters from optical measurements. *Remote Sensing of Environment*, **37**: 207-218.

Kuusk, A., 1994. A multispectral canopy reflectance model. *Remote Sensing of Environment*, **50**(2): 75-82.

Kuusk, A., 1995a. A fast invertible canopy reflectance model. *Remote Sensing of Environment*, **51**: 342-350.

Kuusk, A., 1995b. A Markov chain model of canopy reflectance. *Agricultural and Forest Meteorology*, **76**: 221-236.

Kuusk, A., 1998. Monitoring of vegetation parameters on large areas by the inversion of a canopy reflectance model. *International Journal of Remote Sensing*, **19**(15): 2893-2905.

Kuusk, A., 2001. A two-layer canopy, reflectance model. *Journal of Quantitative Spectroscopy and Radiative Transfer*, **71**(1): 1-9.

LAI-COR, I., 1991. LAI-2000 Plant Canopy Analyzer: Operating Manual. 4-14.

Lang, A. R. G., 1987. Simplified estimate of leaf area index from transmittance of the sun's beam. *Agricultural and Forest Meteorology*, **41**: 179-186.

Lee, T. and Y. J. Kaufman, 1986. The effect of surface non-Lambertianity on remote sensing of ground reflectance and vegetation index. *IEEE Transaction of Geoscience and Remote Sensing*, **24**: 699-708.

Li, X., J. Cihlar, X. Zheng, L. Moreau and H. Ly, 1996. The bidirectional effects of AVHRR measurements over boreal regions. *IEEE Transactions on Geoscience and Remote Sensing*, **34**: 1308-1322.

Li, X. and A. Strahler, 1985. Geometric-optical modeling of a coniferous forest canopy. *IEEE Transactions on Geoscience and Remote Sensing*, **23**: 705-721.

Li, X. and A. Strahler, 1986. Geometric-optical bi-directional reflectance modeling of a coniferous forest canopy. *IEEE Transactions on Geoscience and Remote Sensing*, **24**: 906-919.

Li, X. and A. H. Strahler, 1992. Geometric-optical bidirectional reflectance modeling of the discrete crown vegetation canopy: effect of crown shape and multual shadowing. *IEEE Transaction of Geoscience and Remote Sensing*, **30**: 276-292.

Li, X., C. Woodcock and R. Davis, 1995. A hybrid geometric optical-radiative transfer approach for modeling albedo and directional reflectance of discontinuous canopies. *IEEE Transactions on Geosciece and Remote Sensing*, **33**(2): 466-480.

Liang, S., 2000. Numerical experiments on spatial scaling of land surface albedo and leaf area index. *Remote Sensing Reviews*, **19**: 225-242.

Liang, S., 2001. Narrowband to broadband conversions of land surface albedo: I. Formulae. *Remote Sensing of Environment*, **76**: 213-238.

Liang, S., 2003a. A direct algorithm for estimating land surface broadband albedos from MODIS Imagery. *IEEE Transactions on Geoscience and Remote Sensing*, **41**(1): 136-145.

Liang, S., 2003b. *Quantitative Remote Sensing of Land Surfaces*. New York, John Wiley and Sons, Inc. pp.

Liang, S., H. Fallah-Adl, S. Kalluri, J. JaJa, Y. J. Kaufman and J. R. G. Townshend, 1997. An operational atmospheric correction algorithm for Landsat Thematic Mapper imagery over the land. *Journal of Geophysical Research (Atmospheres)*, **102**: 17173-17186.

Liang, S., H. Fang and M. Chen, 2001. Atmospheric correction of landsat ETM+ land surface imagery: I. Methods. *IEEE Transactions on Geosciences and Remote Sensing*, **39**(11): 2490-2498.

Liang, S., H. Fang, M. Chen, C. Walthall, C. Daughtry, J. Morisette, C. Schaff and A. Strahler, 2002a. MODIS land surface reflectance and albedo products: Methods and preliminary results. *Remote Sensing of Environment*, **83**: 149-162.

Liang, S., H. Fang, L. Thorp, M. Kaul, T. G. V. Niel, T. R. McVicar, J. Pearlman, C. Walthall, C. Daughtry, F. Huemmrich and D. L. B. Jupp, 2002b. Estimation of land surface broadband albedos and leaf area index from EO-1 ALI data and validation. *IEEE Transactions on Geosciences and Remote Sensing*, **in press**.

Liang, S. and A. H. Strahler, 1993a. An analytic BRDF model of canopy radiative transfer and its inversion. *IEEE Transaction on Geoscience and Remote Sensing*, **31**(5): 1081-1092.

Liang, S. and A. H. Strahler, 1993b. The calculation of the radiance distribution of the coupled atmosphere-canopy. *IEEE Transactions on Geoscience and Remote Sensing*, **31**(2): 491-502.

Liang, S. and A. H. Strahler, 1994a. A four-stream solution for atmospheric radiative transfer over an non-Lambertian surface. *Applied Optics*, **33**: 5745-5753.

Liang, S. and A. H. Strahler, 1994b. Retrieval of surface BRDF from multiangle remotely sensed data. *Remote Sensing of Environment*, **50**: 18-30.

Lin, Y. and K. Sarabandi, 1999. Retrieval of forest parameters using a fractal-based coherent scattering model and a genetic algorithm. *IEEE Transactions on Geoscience and Remote Sensing*, **37**(3): 1415-1424.

Liu, H. Q. and A. R. Huete, 1995. A feedback based modification of the NDVI to minimize soil and atmospheric noise. *IEEE Transaction of Geoscience and Remote Sensing*, **33**: 457-465.

McLeod, S. D. and S. W. Running, 1988. Comparing site quality indices and productivity in Ponderosa pine stands of western Montana. *Canadian Journal of Forest Research*, **18**: 346-352.

McNaughton, K. G. and P. G. Jarvis, 1983. *Predicting effects of vegetation changes on transpiration and evaporation*. In T. T. Kozlowski (Ed.) Water Deficits and Plant Growth (pp. 1-47). London, England., Academic Press.

Miesch, C., X. Briottet, Y. H. Kerr and F. Cabot, 1999. Monte Carlo approach for solving the radiative transfer equation over mountainous and heterogeneous areas. *Applied Optics*, **38**: 7419-7430.

Moran, M. S., R. D. Jackson, G. F. Hart, P. N. Slater, R. J. Bartell, S. F. Biggar, D. I. Gellman and R. P. Santer, 1990. Obtaining surface reflectance factors from atmospheric and view angle corrected SPOT-1 HRV data. *Remote Sensing of Environment*, **32**: 203-214.

Moran, M. S., R. D. Jackson, P. N. Slater and P. M. Teillet, 1992. Evaluation of simplified procedures for retrieval of land surface reflectance factors from satellite sensor output. *Remote Sensing of Environment*, **41**: 169-184.

Morisette, J. T., J. L. Privette and C. O. Justice, 2002. A framework for the validation of MODIS Land products. *Remote Sensing of Environment*, **83**(1-2): 77-96.

Muller, E. and H. Décamps, 2001. Modeling soil moisture-reflectance. *Remote Sensing of the Environment*, **76**(2): 173-180.

Myneni, R. B. and B. D. Ganapol, 1991. A simplified formulation of photon transport in leaf canopies with finite dimensional scatterers. *Journal of Quantitative Spectroscopy and Radiative Transfer*, **46**: 135-140.

Myneni, R. B., S. Maggion, J. Iaquinta, J. L. Privette, N. Gobron, B. Pinty, D. S. Kimes, M. M. Verstraete and D. L. Williams, 1995. Optical remote sensing of vegetation: Modeling, caveats, and algorithms. *Remote Sensing of Environment*, **51**: 169-188.

Myneni, R. B., R. Ramakrishna, R. Nemani and S. W. Running, 1997. Estimation of global leaf area index and absorbed par using radiative transfer models. *IEEE Transactions on Geosciences and Remote Sensing*, **35**(6): 1380 -1393.

Myneni, R. B., J. Ross and G. Asrar, 1989. A review on the theory of photon transport in leaf canopies. *Agricultural and Forest Meteorology*, **45**(1-2): 1-153.

Nilson, T. and A. Kuusk, 1989. A reflectance model for the homogeneous plant canopy and its inversion. *Remote Sensing of Environment*, **27**(2): 157-167.

Norman, J. M. and J. M. Welles, 1983. Radiative transfer in an array of canopies. *Agronomy Journal*, **75**: 81-488.

Otterman, J., 1984. Albedo of a forest modeled as a plane with dense protrusions. *Journal of Climate and Appllied Meteorology*, **22**: 297-307.

Otterman, J. and R. S. Fraser, 1976. Earth-atmosphere system and surface reflectivities in arid regions from Landsat (MSS data). *Remote Sensing Environ*, **5**: 247-266.

Otterman, J., D. E. Strebel and K. J. Ranson, 1987. Inferring spectral reflectances of plant elements by simple inversion of bidirectional reflectance measurements. *Remote Sensing of Environment*, **21**(2): 215-228.

Ouaidrari, H. and E. F. Vermote, 1999. Operational atmospheric correction of Landsat TM data. *Remote Sensing of Environment*, **70**: 4-15.

Pearson, R. L. and L. D. Miller, 1972. Remote mapping of standing crop biomass for estimation of the productivity of the short-grass Prairie, Pawnee National Grasslands, Colorado. *8th Int. Symp. on Remote Sensing of Environment*, ERIM, Ann Arbor, MI.

Peterson, D. L., M. A. Spanner, S. W. Running and K. B. Teuber, 1987. Relationship of thematic mapper simulator data to leaf area index of temperate coniferous forest. *Remote Sensing of Environment*, **22**: 323-341.

Pinilla Ruiz, C. and F. J. Ariza López, 2002. Restoring SPOT images using PSF-derived deconvolution filters. *International Journal of Remote Sensing*, **23**(12): 2379-2391.

Pinty, B., M. M. Verstraete and R. E. Dickinson, 1990. A physical model for the bidirectional reflectance of vegetation canopies - Part 2: Inversion and validation. *J. Geophysical Research*, **95**: 11767-11775.

Plummer, S. E., 2000. Perspectives on combining ecological process models and remotely sensed data. *Ecological Modeling*, **129**: 169-186.

Popp, T., 1995. Correcting atmospheric masking to retrieve the spectral albedo of land surfaces from satellite measurements. *International Journal of Remote Sensing*, **16**(18): 3483-3508.

Press, W. H., S. A. Teukolsky, W. T. Vetterling and B. P. Plannery, 1992. *Numerical Recipes in C: The Art of Scientific Computing*. New York, Cambridge University Press. pp.

Price, J. C., 1990. On the information content of soil reflectance spectra. *Remote Sensing of Environment*, **33**: 113-121.

Price, J. C. and J. C. Bausch, 1995. Leaf area index estimation from visible and near-infrared reflectance data. *Remote Sensing of Environment*, **52**: 55-65.

Prince, S. D., 1999. *What practical information about land-surface function can be determined by remote sensing? Where do we stand?* In J. D. Tenhunen and P. Kabat (Eds.), Integrating Hydrology, Ecosystem Dynamics, and Biogeochemistry in Complex Landscapes (pp. 39-60). New York, John Wiley & Sons Ltd.

Prince, S. D. and S. N. Goward, 1995. Global primary production: a remote sensing approach. *Journal of Biogeography*, **22**(4-5): 815-835.

Privette, J., R. Myneni, J. Morisette and C. Justice, 1998. Global validation of EOS LAI and FPAR products. *Earth Observer*, **10**(6): 39-42.

Privette, J. L., W. J. Emery and D. S. Schimel, 1996. Inversion of a vegetation reflectance model with NOAA AVHRR data. *Remote Sensing of Environment*, **58**(2): 187-200.

Privette, J. L., R. B. Myneni, C. J. Tucker and W. J. Emery, 1994. Invertibility of a 1-D Discrete Ordinates cCanopy Reflectance Model. *Remote Sensing of Environment*, **48**: 89-105.

Qi, J., A. Chehbouni, A. R. Huete, Y. Kerr and S. Sorooshian, 1994. A modified soil adjusted vegetation index (MSAVI). *Remote Sensing of Environment*, **48**: 119-126.

Qi, J., Y. H. Kerr, M. S. Moran, M. Weltz, A. R. Huete, S. Sorooshian and R. Bryant, 2000. Leaf area index estimates using remotely sensed data and BRDF models in a semiarid region. *Remote Sensing of Environment*, **73**: 18-30.

Qin, W. and S. Liang, 2000. Plane-parallel canopy radiation transfer modeling: recent advances and future directions. *Remote Sensing Reviews*, **18**: 281-306.

Qiu, J., 2001. An improved model of surface BRDF-atmospheric coupled radiation. *IEEE Transactions on Geoscience and Remote Sensing*, **39**(1): 181-187.

Qiu, W., J. R. Herman and Z. Ahmad, 2001. A fast, accurate algorithm to account for non-Lambertian surface effects on TOA radiance. *Journal of Geophysical Research*, **106**(D19): 22671-22684.

Rahman, H., 2001. Influence of atmospheric correction on the estimation of biophysical parameters of crop canopy using satellite remote sensing. *International Journal of Remote Sensing*, **22**(7): 1245-1268.

Rahman, H., B. Pinty and M. M. Verstraete, 1993. Coupled surface-atmosphere reflectance (CSAR) mdel, 2, Semiempirical surface model usable with NOAA advanced very high resolution radiometer data. *Journal of Geophysical Research*, **98**: 20791-20801.

Reinersman, P. N. and K. L. Carder, 1995. Monte Carlo simulatioin of the atmospheric point-spread function with an application to correction for the adjacency effect. *Applied Optics*, **34**: 4453-4471.

Renders, J.-M. and S. P. Flasse, 1996. Hybrid methods using genetic algorithms for global optimization. *IEEE Transactions on Systems, Man, and Cybernetics-Part B: Cybernetics*, **26**(2): 243-258.

Richardson, A. J. and C. L. Wiegand, 1977. Distinguishing vegetation from soil background information. *Photogrammetric Engineering and Remote Sensing*, **43**: 1541-1552.

Richter, R., 1996a. Atmospheric correction of satellite data with haze removal including a haze/clear transition region. *Computers and Geosciences*, **22**: 675-681.

Richter, R., 1996b. A spatially adaptive fast atmospheric correction algorithm. *International Journal of Remote Sensing*, **17**: 1201-1214.

Richter, R., 1997. Correction of atmospheric and topographic effects for high spatial resolution satellite imagery. *International Journal of Remote Sensing*, **18**: 1099-1111.

Rosema, A., W. Verhoef, H. Noorbergen and J. J. Borgesius, 1992. A new forest light interaction model in support of forest monitoring. *Remote Sensing of Environment*, **51**: 375-384.

Ross, J. and A. Marshak, 1989. The influence of leaf orientation and the specular component of leaf reflectance on the canopy bidirectional reflectance. *Remote Sensing of Environment*, **27**(3): 251-260.

Ross, J. K. and A. L. Marshak, 1988. Calculation of canopy bidirectional reflectance using the Monte Carlo method. *Remote Sensing of Environment*, **24**(2): 213-225.

Roujean, J. L. and F. M. Bréon, 1995. Estimating PAR Absorbed by Vegetation from Bidirectional Reflectance Measurements. *Remote Sensing of Environment*, **51**: 375-384.

Roujean, J. L., M. Leory, A. Podaire and P. Y. Deschamps, 1992. Evidence of surface reflectance bidirectional effects from a NOAA/AVHRR multi-temporal data set. *International Journal of Remote Sensing*, **13**: 685-698.

Roujean, J. L., D. Tanré, F. M. Bréon and J. L. Deuzé, 1997. Retrieval of land surface parameters from airborne POLDER bidirectional reflectance distribution function during HAPEX-Sahel. *Journal of Geophyscial Research*, **101**(D10): 11201-11218.

Rouse, J. W., R. H. Haas, J. A. Schell, D. W. Deering and J. C. Harlan, 1974. *Monitoring the vernal advancement of retrogradation of natural vegetation.*, Greenbelt, MD, NASA/GSFC**:** 371.III.

Running, S. W. and J. C. Coughlan, 1988. A general model of forest ecosytem processes for regional applications. I. Hydrologic balance, canopy gas exchange and primary production processes. *Ecological Modelling*, **42**: 125-154.

Schroeder, P. E., B.McCandish, R.H.Waring and D.A.Perry, 1982. The relationship of maximum canopy leaf area to forest growth in eastern Washington. *Northwest Science*, **56**: 455-457.

Sellers, P., 1985. Canopy reflectance, photosynthesis and transpiration. *International Journal of Remote Sensing*, **6**: 1335-1372.

Sellers, P. J., Y. Mintz, Y. C. Sud and A. Dalcher, 1986. A simple biosphere model (SiB) for use within general circulation models. *Journal of the Atmopsheric Science*, **43**: 505-531.

Singh, S. M., 1988. Simulation of solar zenith angle effect on global vegetationindex (GVI) data. *International Journal of Remote Sensing*, **9**: 237-248.

Singh, S. M. and A. P. Cracknell, 1986. The estimate of atmospheric effects for SPOT using AVHRR channel-1 data. *International Journal of Remote Sensing*, **7**: 361-377.

Slater, P. N., S. F. Biggar, R. G. Holm and and others, 1987. Reflectance- and radiance-based methods for the in-flight absolute calibration of multispectral sensors. *Remote Sensing of Environment*, **22**: 11-37.

Smith, J. A., 1993. LAI inversion using a backpropagation neural network trained with a multiple scattering model. *IEEE Transactions on Geoscience and Remote Sensing*, **31**: 1102-1106.

Stoner, E. R., 1979. *Physicochemical, site, and bidirectional reflectance factor characteristics of uniformly moist soils.*, W. Lafayette, IN 47907, Purdue University.Ph.D thesis.

Tanré, D., P. Y. Deschamps, P. Duhaut and M. Herman, 1987. Adjacency effect produced by the atmospheric scattering in Thematic Mapper Data. *Journal of Geophysical Research*, **92**(D10): 12000-12006.

Tanré, D., M. Herman and P. Y. Deschamps, 1983. Influence of the atmosphere on space measurements of directional properties. *Applied Optics*, **22**: 733-741.

Tanré, D., M. Herman, P. Y. Deschamps and A. De Leffe, 1979. Atmospheric modeling for space measurements of ground reflectances including bidirectional properties. *Applied Optics*, **18**(21): 3587-3594.

Tanré, D., B. N. Holben and Y. J. Kaufman, 1992. Atmospheric correction algorithm for NOAA-AVHRR products: Theory and application. *IEEE Transactions on Geoscience and Remote Sensing*, **30**: 231-248.

Tian, Y., Y. Wang, Y. Zhang, Y. Knyazikhin, J. Bogaert and R. B. Myneni, 2003. Radiative transfer based scaling of LAI retrievals from reflectance data of different resolutions. *Remote Sensing of Environment*, **84**(1): 143-159.

Tian, Y., C. E. Woodcock, Y. Wang, J. L. Privette, N. V. Shabanov, L. Zhou, Y. Zhang, W. Buermann, J. Dong, B. Veikkanen, T. Häme, K. Andersson, M. Ozdogan, Y. Knyazikhin and R. B. Myneni, 2002. Multiscale analysis and validation of the MODIS LAI product I. Uncertainty assessment. *Remote Sensing of Environment*, **83**(3): 414-430.

Tian, Y., Y. Zhang, Y. Knyazikhin, R. B. Myneni, J. M. Glassy, D. Dedieu and S. W. Running, 2000. Prototyping of MODIS LAI and FPAR algorithm with LASUR and LANDSAT data. *IEEE Transactions on Geoscience Remote Sensing*, **38**(5): 2387–2401.

Tucker, C. J., 1979. Red and photographic infrared linear combinations monitoring vegetation. *Remote Sensing of Environment*, **8**: 127-150.

Turner, D. P., W. B. Cohen, R. E. Kennedy, K. S. Fassnacht and J. M. Briggs, 1999. Relationships between Leaf Area Index and Landsat TM spectral Vegetation Indices across three Temperate Zone Sites. *Remote Sensing of Environment*, **70**: 52-68.

Venables, W. N. and B. D. Ripley, 1994. *Modern applied statistics with S-PLUS*. New York, Springer-Verlag. pp. 462

Verhoef, W., 1984. Light scattering by leaf layers with application to canopy reflectance modeling: The SAIL model. *Remote Sensing of Environment*, **16**: 125-141.

Vermote, E., D. Tanré and M. Herman, 1990. Atmospheric effects on satellite imagery: correction algorithms for ocean color or vegetation monitoring. *International Society for Photogrammetry and Remote Sensing*, **28**: 46-55.

Vermote, E. F., D. Tanre, J. L. Deuze, M. Herman and J. J. Morcrette, 1997. Second simulation of the satellite signal in the solar spectrum, 6S: An overview. *IEEE Transactions on Geoscience and Remote Sensing*, **35**(3): 675-686.

Verstaete, M. M., B. Pinty and R. E. Dickinson, 1990. A physical model of the bidirectional reflectance vegetation canopies, I Theory. *J. Geophy. Res.*, **95**(D8): 11755-11765.

Verstraete, M. M., B. Pinty and R. E. Dickinson, 1990. Bidirectional reflectance of vegetation canopies. Part I: Theory. *Journal of Geophysical Research*, **95**: 11755-11765.

Walthall, C., 1997. A study of reflectance anisotropy and canopy structure using a simple empirical model. *Remote Sensing of Environment*, **61**: 118-128.

Walthall, C., J. L. Roujean and J. Morisette, 2000. Field and landscape BRDF optical wavelength measurements: experience, techniques and the future. *Remote Sensing Reviews*, **18**: 503-531.

Walthall, C. L., J. M. Norman, J. M. Welles, G. Campbell and B. L. Blad, 1985. Simple equation to approximate the bi-directional reflectance from vegetation canopies and bare soil surfaces. *Applied Optics*, **24**: 383-387.

Wang, Y., Y. Tian, Y. Zhang, N. El-Saleous, Y. Knyazikhin, E. Vermote and R. B. Myneni, 2001. Investigation of product accuracy as a function of input and model uncertainties: case study with SeaWiFS and MODIS LAI/FPAR algorithm. *Remote Sensing of Environment*, **78**: 296-311.

Weiss, M. and F. Baret, 1999. Evaluation of canopy biophysical variable retrieval performances from the accumulation of large swath satellite data. *Remote Sensing of Environment*, **70**: 293-306.

Weiss, M., F. Baret, R. B. Myneni, A. Pragnere and Y. Knyazikhin, 2000. Investigation of a model inversion technique to estimate canopy biophysical variables from spectral and directional reflectance data. *Agronomie*, **20**(1): 3-22.

White, J. D., K. C. Ryan, S. W. Running, R. Nemani and R. E. Keane, 1997. Measurement and remote sensing of LAI in rocky mountain montane ecosystems. *Canadian Journal of Forest Research*, **27**(11): 1714-1727.

Wittwer, S., 1983. *Land related global habitability science issues*, Washington, D.C., National Aeronautics and Space Administration.

Woodcock, C. E., J. Collins, V. D. Jakabhazy, X. Li, S. A. Macomber and Y. Wu, 1997. Inversion of the Li-Strahler canopy reflectance model for mapping forest structure. *IEEE Transactions on Geoscience and Remote Sensing*, **35**(2): 405-414.

Yin, Z. and T. H. L. Williams, 1997. Obtaining spatial and temporal vegetation data from Landsat MSS and AVHRR/NOAA satellite images for a hydrologic model. *Photogrammetric Engineering and Remote Sensing*, **63**(1): 69-77.

Zhang, Y., B. Guindon and J. Cihlar, 2002. An image transform to characterize and compensate for spatial variations in thin cloud contamination of Landsat images. *Remote Sensing of Environment*, **87**(2-3): 173-187.

Zhang, Y., Y. Tian, Y. Knyazikhin, J. V. Martonchik, D. J. Diner, M. Leroy and R. B. Myneni, 2000. Prototyping of MISR LAI and FPAR algorithm with POLDER data over Africa. *IEEE Transactions on Geoscience Remote Sensing*, **38**(5): 2402-2418.

Zhuang, J. and X. Xu, 2000. Genetic algorithms and its application to the retrieval of component temperature. *Remote Sensing for Land and Resources (Chinese)*(1): 28-33.